Master Thesis

Motional Quantum States of Cesium Atoms Trapped Around a Nanofiber

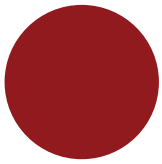

University of Copenhagen

Jacob Thornfeldt Hansen

There is nothing like looking,
if you want to find something…
You certainly usually find something,
if you look, but it is not always quite
the something you were after.

-J.R.R. TOLKIEN, THE HOBBIT

Motional Quantum States of Cesium Atoms Trapped Around a Nanofiber

Author Jacob Thornfeldt Hansen

Supervisor Assoc. Prof. Jörg Helge Müller

Supervisor Prof. Eugene Simon Polzik

Student ID: kjf816

QUANTOP

The Niels Bohr Institute

Submitted to the University of Copenhagen
August 5th, 2020

Abstract

The interaction of mesoscopic atomic ensembles with a single optical mode in the strong coupling regime can be realized using optical nanofibers. The evanescent field of light, guided by an optical fiber of sub-wavelength diameter, allows for strong confinement of neutral atoms by utilizing dipole forces.

The same strong confinement allows for the resolution of motional sidebands, which reveal information about the motional state of the atomic ensemble.

In this thesis, the fabrication, characterization and installation of a new nanofiber is presented. The analysis of sideband resolved Raman spectra gives us an insight into the temperature of trapped Cesium atoms. Different methods of accounting for systematic errors are presented and critically evaluated. The motional states of the trap potential are studied numerically and comparisons with the experimental temperature estimation method show good agreement with the numerical results.

Sammenfatning

Interaktionen mellem mesoskopiske atomare ensembler med en enkelt optisk mode i det stærke koblingsregime, kan realiseres ved brug optiske nanofibre. Det hurtigt aftagende lysfelt, ledet af en optisk fiber med sub-bølgelængde diameter, muliggør stærk indskrænkelse af neutrale atomer ved at udnytte dipolkræfter.

Den selvsamme stærke indskrænkelse tillader os at opløse bevægelsessidebånd, som afslører information om bevægelsestilstanden for det atomare ensemble.

I denne afhandling vil fabrikationen, karakteriseringen og installationen af en ny nanofiber blive præsenteret. Analysen af sidebåndsopløste Raman spektre giver os en indsigt i temperaturen af de fangede Cæsium atomer. Forskellige måder at tage højde for systematiske fejl præsenteres og evalueres kritisk. Bevægelsestilstandene i fældepotentialet bliver studeret numerisk og sammenligninger med den eksperimentelle temperaturestimeringsmetode viser god overensstemmelse med de numeriske resultater.

ACKNOWLEDGMENTS

This thesis is the conclusion of the past year and a half, working on the nanofiber experiment in the Quantop research group. While there were many stressful and trying times, the experience has been extremely enriching and i think it has made me a much better scientist. This work could not have been done without the help and support of the people around me.

First i would like to thank my two supervisors, Jörg Helge Müller and Eugene Simon Polzik. To Jörg; thank you for your guidance, both experimental and theoretical. It really is a privilege to have as devoted a supervisor as you. You are truly a fount of knowledge. To Eugene; thank you for allowing me to be a part of your group and for being a great source of inspiration throughout the process.

Thank you to Jürgen Appel for your technical guidance and for taking time out to help us, when our nanofiber broke.

I would like to express my sincerest appreciation to Signe Brynold Markussen, with whom i got to share all of the trials and tribulations, and of course, successes in the lab. I am truly grateful to have had you as a lab partner. Also thank you to Estrid Naver and Zixuan Song for your contributions to the experiment and for your great company.

The work in this thesis could not have been done if not for Christoffer Østfeldt and Freja T. Pedersen. Your past work on the nanofiber experiment has been instrumental and an invaluable source of information.

Thank you to all the wonderful people at Quantop. It is a lot of fun to work with people who are as passionate, ambitious, and welcoming as you are.

Finally, I wish to thank my family and friends for their support and encouragement throughout my study and for keeping my spirits up when things did not go as planned.

Contents

List of Figures

INTRODUCTION

Since the first measurements of quantum systems, exploration into the fundamental physical properties has allowed for observations of phenomena which radically changed our perception of the physical world. Recent years have seen the emergence of quantum technologies, harnessing the exotic features of quantum systems. The prospect of quantum computing reaching commercial availability has attracted many interested eyes and has roused the public interest.

One of the next frontiers in quantum computing is distributing quantum states using a "Quantum Internet", proposed by Kimble [2008]. For such a system to work, one needs to be able to exchange quantum information between nodes of the network. The widespread use of optical fibers in current information technology lays a strong foundation for light based exchange of quantum information.

For quantum computation, one needs a two-level system, a Qubit, which can be efficiently manipulated and which has coherence times longer than the duration of the quantum computation. Atoms are a promising candidate, given the long coherence times, by virtue of their weak coupling to their environment, Preskill [1998].

The use of atoms as Qubits necessitates the trapping and cooling of atomic motion. Many types of atomic traps exist, however, they mostly fall into two regimes: single atoms and macroscopic ensembles of $\sim 10^6$–10^9 atoms. Free space dipole traps of single atoms allow for strong interaction but suffer from poor scalability, whereas achieving consistent interaction across the entire ensemble is challenging for traps

of macroscopic ensembles.

Optical nanofibers offer a way of interacting with quantum systems of ~ 1000 atoms on a single pass, bridging the gap between the two previously mentioned regimes.

Optical nanofibers are realized as adiabatically tapered single mode optical fibers, first proposed by Tong et al. [2004]. The fast decay of the evanescent field around a sub-wavelength diameter nanofiber provides the steep intensity gradients needed for tight confinement using dipole forces, Kien et al. [2004]; Vetsch et al. [2010]. The diffraction-free propagation of the evanescent field allows for steep intensity gradients across the entire length of the nanofiber. The steep intensity gradients also allow for operation in the strong coupling regime, with single atom ODs of $\sim 2.4\,\%$ Béguin [2015].

However, the same steep intensity gradients, coupled with the anharmonicity of the trap potential, lead to motional state dependent interactions. Several experiments on the manipulation of atoms trapped around a nanofiber have found the finite temperature of the atomic ensemble to be a limiting factor, making cooling of the trapped atoms an important task to improving the performance of nanofiber traps.

On the other hand, the same motional state dependent interaction can be utilized to manipulate the state of the atomic ensemble to realize non-classical motional states, leading to entanglement between the internal and external degrees of freedom of the atoms.

Goal of this thesis

The goal of this thesis is to measure the motional transitions of nanofiber trapped atoms. Using the asymmetric coupling of the motional sidebands one may measure the temperature of the atomic ensemble using stimulated Raman transitions. To study the behavior of trapped atoms in the nanofiber potential, numerical simulations will be employed to grant a deeper insight into the motional spectra.

The nanofiber breaks

On May 5th, 2019, we were struck by tragedy as the nanofiber in our setup broke. This meant that we had to fabricate, characterize and install a new nanofiber into the existing setup. The fiber pulling setup, which had last been used in the summer of 2017, needed to be rebooted.

With the help of Jürgen Appel, we were able to get the setup working, however, we would not have a new nanofiber installed in the setup until November of 2019. This process was immensely educational and allowed us to learn the art of handling optical fibers and how to handle ultra high vacuum components. However, it also meant that progress on the nanofiber experiment was halted for seven months. Our first atomic signal on the new fiber was acquired on the 30th of January, 2020, about nine months after the rupture of the old fiber. Roughly a month and a half later, on the 11th of March, 2020, the novel corona virus, COVID-19, forced the Danish population into quarantine.

These events have had a dramatic effect on my time in the lab. This means that we did not have time to tie up every loose end and explore quite as many different avenues as we would have liked. I urge the reader to keep this in mind while reading this thesis.

Structure of the thesis

This thesis is divided into three main parts. The first part lays the theoretical foundations for understanding the experiment. We first treat atoms and their interaction with light, we will then see how light propagates through sub wavelength diameter optical fibers and finally how these properties can be combined to form a nanofiber atom trap.

The second part concerns the experimental work carried out during the project. The first chapter involves the fabrication, characterization and installation of a new nanofiber. In the second chapter the experimental setup and procedures are presented. The next two chapters involve the calibration of the setup, including the optimization of the trapping parameters and the cancellation of differential Stark shifts due to the Raman laser. The final chapter of the second part presents the work on resolved Raman spectroscopy with a focus on temperature estimation.

In the third part we treat the trapping potential numerically. We first establish the necessary theoretical foundations for simulating a two-level atom with motional states. We then move on to finding the wavefunctions of the one dimensional radial trap potential and subsequently simulating Raman spectra, comparing the results to the experimental methods. We then extend our treatment to the two dimensional potential, finding the wavefunctions and studying the non-separability of the potential. We finally highlight some of the possible improvements and future paths for the simulations.

Part I

Foundations

CHAPTER

1 ATOMIC PHYSICS

One of the early ground-breaking results in quantum mechanics was solving the energy structure of hydrogen. Hydrogen, being the simplest atom in the periodic table of elements, has a single electron orbiting the nucleus. The use of hydrogen-like atoms is prevalent in atomic physics; using hydrogen-like atoms, also known as alkali metals, allows us to draw from the results obtained in the treatment of the hydrogen atom to understand larger, more complicated atoms.

In this chapter the structure of Cesium will be presented, following the treatment given in [Foot, 2005] and [Steck, 2007].

1.1 The Cesium atom

The atom of choice for this work is Cesium. Cesium, being the second heaviest of the alkali metals (no. 55 in the periodic table), is well suited for low temperature experiments. Cesium has a single stable isotope, ^{133}Cs, which is by far the most naturally abundant isotope.

Cesium has a single electron in its outermost orbital, with the remaining orbitals fully occupied. This allows us to treat Cesium as having a single electron orbiting a modified central potential. We can therefore use the results for the hydrogen atom to gain some insight into the nature of Cesium.

Given the rotational symmetry of the Hydrogen atom, the solutions can be separated into radial and angular wave functions, $R_{n,l}$ and $Y_{l,m}$,

were n, l, m are quantum numbers describing the orbitals. In Hydrogen, the energy structure only depends on the principal quantum number n. For each n there are $n-1$ degenerate states with angular momentum l and $2l+1$ magnetic quantum numbers, determining the projection of l on to the z-axis.

Due to the modified central potential of Cesium, the l degeneracy is lifted. In this work we shall focus on the D-line; the transition between $|N=6, L=0, m\rangle$ and $|N'=6, L'=1, m'\rangle$, where we have written n, l in capital letters to differentiate from the hydrogen wavefunction. Additionally we denote excited states with a prime, e.g L', throughout this thesis. The quantum numbers N and L describe the gross electronic energy structure of the atom, i.e. the largest energy scale for the atoms.

We will now delve into the smaller energy scales, which are relevant in this work.

1.1.1 Fine structure

The fine structure concerns the interaction of an electrons spin with its own angular momentum. From the perspective of the orbiting electron, the charge of the nucleus produces a magnetic field. This magnetic field interacts with the magnetic dipole moment of the electron leading to energy splitting dependent on the orientation of the electron spin with respect to the magnetic field.

From the orbital angular momentum $\mathbf{L}$ and spin $\mathbf{S}$, we can find the total angular momentum

$$\mathbf{J} = \mathbf{L} + \mathbf{S}, \tag{1.1}$$

which can take on values, in increments of 1, of

$$|L - S| \leq J \leq L + S. \tag{1.2}$$

This coupling leads to the splitting of the excited state $|N'=6, L'=1\rangle$ into $|N'=6, L'=1, J'=1/2\rangle$ and $|N=6, L'=1, J'=3/2\rangle$. The ground state has $L=0$ and therefore there is only one level, $|N=6, L=0, J=1/2\rangle$. In the absence of strong magnetic fields these states all have $2J+1$ degenerate magnetic levels, denoted m_J. In our experiment we are only concerned with the transition between $L=0, J=1/2$ and $L'=1, J'=3/2$, known as the D2-line. These states are also referred to as $6^2S_{1/2}$ and $6^2P_{3/2}$.

To transition between the states of the fine structure, certain rules have to be obeyed. For electric dipole transitions the change in total angular momentum J must obey

$$\begin{aligned} \Delta J &= 0, \pm 1 \\ \Delta m_J &= 0, \pm 1 \\ J = 0 &\nleftrightarrow 0 \end{aligned} \tag{1.3}$$

Transitions which preserve m_J are called π-transitions and are driven by linearly polarized light, whereas transitions which change m_J by ± 1 are called $\sigma^{\pm}$-transitions, driven by circularly polarized light.

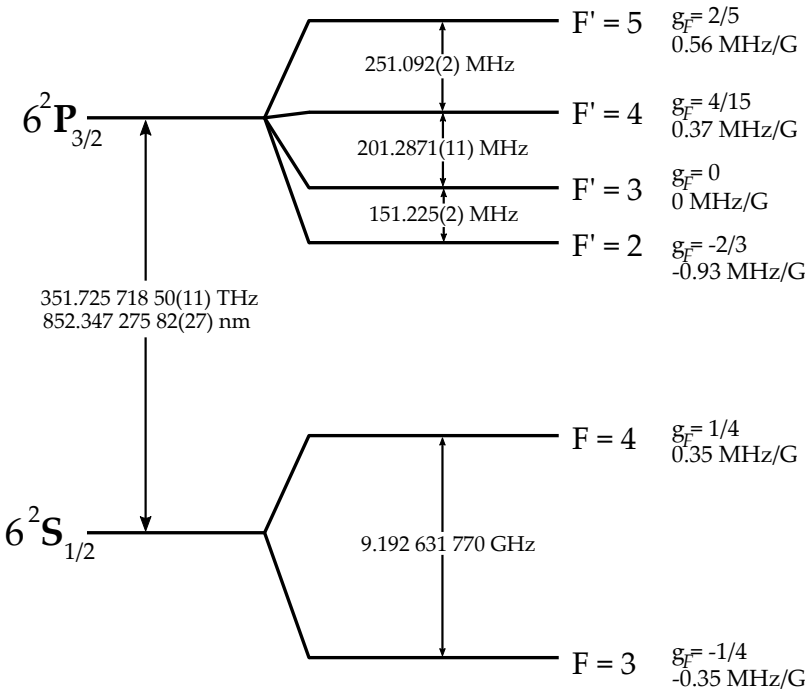

Figure 1.1 — Energy levels of the D2 line of Cesium. The ground state splitting has no uncertainty since it is defined as this exact value. The Landé g-factors are shown along with the Zeeman splitting per Gauss. This figure is heavily inspired by a similar figure from [Steck, 2007]

1.1.2 Hyperfine structure

Another splitting occurs due to the fact that the nucleus of the atom has a spin with a corresponding magnetic moment. This magnetic moment

interacts with the angular momentum of the electron. This splitting is known as the hyperfine splitting. Analogously to the fine structure we can define a total angular momentum, now including the nuclear spin

$$\mathbf{F} = \mathbf{J} + \mathbf{I}, \tag{1.4}$$

which takes on values in increments of 1 of

$$|J - I| \leq F \leq J + I \tag{1.5}$$

equivalently to the fine structure this leads to splitting of the fine structure levels. For Cesium the nuclear spin is $7/2$ leading to values of $F = 3, 4$ for the ground state and $2, 3, 4, 5$ for the excited state $6^2P_{3/2}$. Each hyperfine level has $2F + 1$ magnetic sublevels.

Due to the fact that the nuclear magnetic dipole moment is significantly smaller than that of the electron, the effect of this interaction is much smaller than the fine structure. The fine structure splitting of the $N = 6, L = 1$ level is $\sim 16\,\text{THz}$, while the hyperfine splitting is only $\sim 9\,\text{GHz}$ for the ground state.

The selection rules governing electric dipole transitions in the hyperfine structure are completely equivalent to those of the fine structure.

$$\begin{aligned} \Delta F &= 0, \pm 1 \\ F = 0 &\nleftrightarrow 0 \\ \Delta m_F &= 0, \pm 1 \end{aligned} \tag{1.6}$$

The rules in eq. 1.6 are of course on top of the fine structure selection rules. Due to parity, transitions between the two ground state hyperfine levels are electric dipole forbidden and thus cannot be directly accessed this way. One can, however, drive these transitions with magnetic dipole transitions, although these are significantly weaker than their electric counterparts.

1.1.3 Zeeman effect

If an applied magnetic field is weak compared to the hyperfine splitting we can look at this as a perturbation to the hyperfine structure. The Zeeman effect leads to a shift of the magnetic sublevels of the hyperfine structure, which is linear in m_F. The shift is given by

$$E = g_F \mu_B m_F B, \tag{1.7}$$

where μ_B is the Bohr magneton, B is the applied magnetic field and m_F is the projection of F onto the magnetic field direction. The factor g_F is the Landé g-factor and is given by

$$g_F = \frac{F(F+1) + J(J+1) - I(I+1)}{2F(F+1)} g_J, \tag{1.8}$$

where g_J is the g-factor for the electron angular momentum.

If we plug in values for the ground state hyperfine levels, 3 and 4, we find that the factors g_F will be equal in magnitude, but with opposite sign. This is shown in figure 1.1. Throughout this work we will pri-

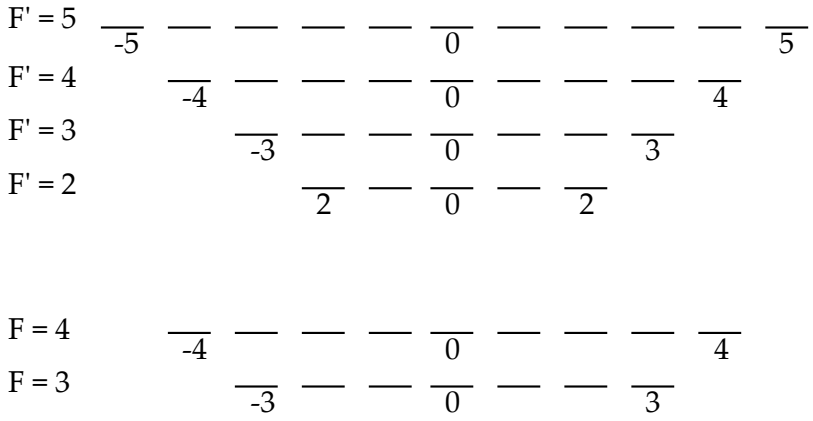

Figure 1.2 — Plot of the D2 line with magnetic sublevels. Numbers under lines refer to the m_F quantum number of the state.

marily focus on the $m_F = 0$ levels of the ground state and the stretched levels, i.e. $|F = 3, m_F = -3\rangle$ and $|F = 4, m_F = -4\rangle$, shown in figure 1.2.

CHAPTER

2 LIGHT-ATOM INTERACTIONS

In this chapter we will study the interaction between light and atoms. We will first derive the two-level Hamiltonian and study its consequences. Then, using the concepts from the two level case, we will expand into multi-level systems and use this to understand some of the manipulations of atoms made possible using electromagnetic radiation. This chapter largely follows the treatment found in [Steck, 2007].

2.1 The two-level atom

Let us consider a two level system interacting with a classical light field. We will denote the two levels as $|g\rangle$ for the ground state and $|e\rangle$ for the excited state. The system is driven by a classical field $\mathbf{E}(t) = \hat{\epsilon} E_0 \cos(\omega t)$, where $\hat{\epsilon}$ is the field polarization, ω is the angular frequency of the field, where we have neglected any spatial contribution to the phase of the electric field over the characteristic size of the electron cloud[1]. Choosing the ground state energy to be zero we can write the atomic Hamiltonian as

$$H_{\mathrm{A}} = \hbar\omega_0 \, |e\rangle\langle e| \tag{2.1}$$

and the atom-field Hamiltonian as

$$H_{\mathrm{AF}} = -\mathbf{d} \cdot \mathbf{E}, \tag{2.2}$$

[1] The dipole approximation

where $\mathbf{d}$ is the atomic dipole operator, $d = -e\mathbf{r}_e$. Here e is the electron charge and $\mathbf{r}_e$ is the position of the electron w.r.t. the nucleus. The full Hamiltonian is then the sum of the two terms,

$$H = H_{\mathrm{A}} + H_{\mathrm{AF}}. \tag{2.3}$$

Writing the electric field in terms of complex exponentials and introducing the atomic lowering operator

$$\sigma = |g\rangle\langle e| \tag{2.4}$$

with the Hermitian conjugate of this being the raising operator, we can write the atom-field part of the Hamiltonian as

$$H_{\mathrm{AF}} = \frac{\hbar\Omega}{2}\left(\sigma e^{i\omega t} + \sigma^\dagger e^{-i\omega t}\right) \tag{2.5}$$

where we have introduced the Rabi frequency, $\Omega = -\frac{\langle g|\hat{\epsilon}\cdot\mathbf{d}|e\rangle E_0}{\hbar}$.

Moving into a rotating frame, rotating at angular frequency ω, we can write the full Hamiltonian without explicit time dependence as,

$$H = -\hbar\Delta\,|e\rangle\langle e| + \frac{\hbar\Omega}{2}\left(\sigma + \sigma^\dagger\right), \tag{2.6}$$

where $\Delta = \omega - \omega_0$.

2.1.1 Rabi flopping

Solving the Schrödinger equation with the Hamiltonian , eq. 2.6, gives us the time evolution of a two-level atom interacting with light. For an initially unexcited atom, i.e. $P_e(0) = 0$, we get

$$P_e(t) = \frac{\Omega^2}{\tilde{\Omega}^2}\sin^2\left(\frac{\tilde{\Omega}t}{2}\right) \tag{2.7}$$

where P_e is the probability of the atom being in the excited state and where $\tilde{\Omega} = \sqrt{\Omega^2 + \Delta^2}$ is the generalized Rabi frequency, [Steck, 2008].

Rabi oscillations at different detunings are plotted in figure 2.1. We see that for a resonant driving field, i.e. $\Delta = 0$, we can transfer the atom into the excited state by applying a pulse with pulse-angle $\Omega t = \pi$, these are fittingly called π-pulses and are an integral part of the experimental toolbox. We can similarly do a resonant pulse with pulse-angle $\Omega t = \pi/2$; this will bring the atom into an equal superposition of $|g\rangle$ and $|e\rangle$.

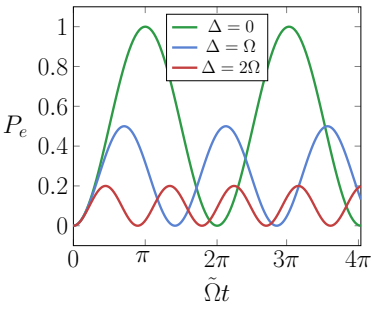

Figure 2.1 — Rabi flopping for different detunings.

2.1.1.1 The Bloch sphere

A useful tool for visualizing the Rabi pulses is the Bloch sphere, [Milonni and Eberly, 2010] and [Foot, 2005]. We can represent a pure state of a two-level system as a unit vector on the surface of a sphere. We begin by introducing the density matrix of a state $|\psi\rangle$,

$$\boldsymbol{\rho} = |\psi\rangle\langle\psi| = \begin{pmatrix} \rho_{11} & \rho_{12} \\ \rho_{21} & \rho_{22} \end{pmatrix} \tag{2.8}$$

where $\rho_{ij} = c_i c_j *$, with $c_{i,j}$ being the coefficients of the state, and where the matrix is Hermitian. We can define the Bloch vector $\mathbf{R} = u\hat{i}+v\hat{j}+w\hat{k}$, where

$$\begin{aligned} u &= \rho_{12} + \rho_{21} \\ v &= -i(\rho_{12} - \rho_{21}) \\ w &= \rho_{11} - \rho_{22}. \end{aligned} \tag{2.9}$$

The Bloch vector contains all of the information about the atomic state. The time evolution of the Bloch vector is governed by,

$$\frac{d\mathbf{R}}{dt} = \boldsymbol{\tau} \times \mathbf{R} \tag{2.10}$$

where $\boldsymbol{\tau}$ is defined as

$$\boldsymbol{\tau} = \mathrm{Re}(\Omega)\hat{i} + \mathrm{Im}(\Omega)\hat{j} + \Delta\hat{k}. \tag{2.11}$$

For a pure state the length of the Bloch vector is constant. Therefore the state can be described by only two numbers, allowing us to write the state as

$$|\psi\rangle = \cos\left(\frac{\theta}{2}\right)|0\rangle + \sin\left(\frac{\theta}{2}\right)e^{i\phi}|1\rangle \tag{2.12}$$

where we have named the two states of the two level system $|1\rangle$ and $|2\rangle$. Applying a resonant pulse, $\Delta = 0$, amounts to placing a torque vector in the equatorial plane of the Bloch sphere. A resonant π-pulse takes the state vector to the antipode. By changing the phase of the Rabi frequency the torque vector can be moved in the equatorial plane. A graphical representation of the Bloch sphere is shown in figure 2.2.

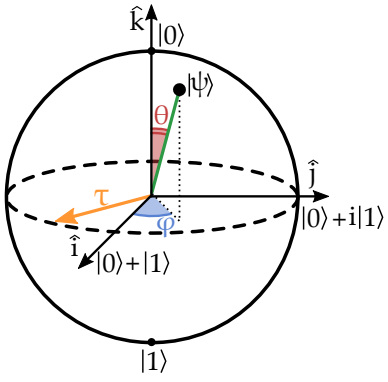

Figure 2.2 — The Bloch sphere. A state ψ is represented as a point on a unit sphere. The state can be uniquely defined by the angles θ and ϕ. A torque vector describes the effect of light interacting with a two level system.

The Ramsey sequence

We see that applying a $\pi/2$-pulse puts the state into the equatorial plane. If the pulse is detuned, the state will continue to precess around the $\hat{z}$-axis with angular velocity Δ. This precession is the basis for Ramsey

spectroscopy; applying an initial $\pi/2$-pulse and allowing the state to evolve for a dark time τ, then applying a second $\pi/2$-pulse to complete the transfer. If the initial pulse is detuned the state will precess in the equatorial plane and the subsequent pulse is no longer perpendicular to the state vector, thus not completing the transfer. By scanning the phase of the second transfer pulse one can map out a fringe which allows for extremely precise measurement of the detuning.

2.1.2 The AC Stark shift

The mixing of levels seen in the previous sections means that the original atomic states are no longer the eigenstates of the coupled system, [Dalibard and Cohen-Tannoudji, 1985]. We therefore need to diagonalize the Hamiltonian, eq. 2.6 to find the new eigenstates and energies. Writing the Hamiltonian as a matrix we get

$$H = \hbar \begin{pmatrix} -\Delta & \frac{\Omega}{2} \\ \frac{\Omega}{2} & 0 \end{pmatrix} \tag{2.13}$$

We can now find the eigenvalues of the Hamiltonian

$$E_{+,-} = -\frac{\hbar\Delta}{2} \pm \frac{\hbar\sqrt{\Delta^2 + \Omega^2}}{2} \tag{2.14}$$

with the two eigenstates $|+\rangle$ and $|-\rangle$ defined by

$$\begin{aligned} |+\rangle &= \sin(\theta)\,|g\rangle + \cos(\theta)\,|e\rangle \\ |-\rangle &= \cos(\theta)\,|g\rangle - \sin(\theta)\,|e\rangle \end{aligned} \tag{2.15}$$

where $\tan(2\theta) = -\frac{\Omega}{\Delta}$. This shift of the energy levels is known as the AC Stark shift. In the limit of $|\Delta| \gg \Omega$, the eigenenergies become

$$E_{\pm} \approx \frac{\hbar}{2}\left(-\Delta \pm \left(\Delta + \frac{\Omega^2}{2\Delta}\right)\right) \tag{2.16}$$

and the states become

$$\begin{aligned} |+\rangle &\approx |e\rangle \\ |-\rangle &\approx |g\rangle \end{aligned} \tag{2.17}$$

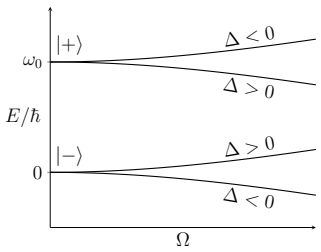

Figure 2.3 — The shift of energy levels due to the presence of detuned light.

This means that for a fixed detuning $|\Delta| \gg \Omega$ and a spatially dependent Rabi frequency the Stark shift leads to a potential,

$$U_{\text{dip}}(r) = \frac{\hbar\Omega(r)^2}{4\Delta} \tag{2.18}$$

of the ground state of the atom. Equation 2.16 is plotted as a function of Rabi frequency in figure 2.3. The shift of the ground state energy is dependent on the square of the Rabi frequency and thus is linear in intensity. Therefore, strong intensity gradients lead to strong dipole forces, a phenomenon which will be exploited to form the nanofiber trap.

2.2 Multi-level atoms

2.2.1 Scalar, vector and tensor light shifts

In the treatment of the Stark shift we only considered a two level atom. In reality atoms have an infinite number of bound states which should, in principle, be taken into account. The derivation of the effects of the full level structure is very lengthy and will therefore not be presented. The light shifts can be written in terms of scalar, vector and tensor polarizabilities as

$$\begin{aligned}\Delta E(F, m_{\mathrm{F}}, \omega) = &- \alpha^{(0)}(F,\omega)|E_0^{(+)}|^2 \\ &- \alpha^{(1)}(F,\omega)(iE_0^{(-)} \times E_0^{(+)})_z \frac{m_{\mathrm{F}}}{F} \\ &- \alpha^{(2)}(F,\omega)\frac{\left(3|E_{0z}^{(+)}|^2 - |E_0^{(+)}|^2\right)}{2}\left(\frac{3m_{\mathrm{F}}^2 - F(F+1)}{F(2F-1)}\right)\end{aligned} \tag{2.19}$$

where $\alpha^{(1,2,3)}(F,\omega)$ are the scalar, vector and tensor polarizabilities, respectively and where $E^{(\pm)}$ are the positive(negative) frequency parts of the electric field, [Steck, 2008].

The first term of equation 2.19 is the scalar term, which is essentially what we derived in the previous section. The second term is the vector shift. This is also known as a fictitious magnetic field because it interacts with the magnetic sublevels in a fashion very reminiscent of a magnetic field. This fictitious magnetic field arises from circularly polarized light; the term $(E_0^{(-)} \times E_0^{(+)}) = 0$ for linearly polarized light. The fictitious magnetic fields may be vector-added to real magnetic fields, [Le Kien et al., 2013].

The final term is the tensor shift. This induces shifts on the levels m_F proportional to m_F^2 as opposed to the linear shift due to the vector shift. The tensor shift is, unlike the vector shift, maximal when the driving light is polarized along the quantization axis. The tensor shift of the ground state of Cesium vanishes for detunings large compared to the hyperfine splitting, [Lacrôute et al., 2012].

2.2.2 Raman transitions

A useful tool for driving transitions between states of the ground level manifold are stimulated Raman transitions. Stimulated Raman transitions are two-photon transitions in a three-level system. We would like to drive transitions between two levels, $|g_1\rangle$ and $|g_2\rangle$, that are closely spaced, via a virtual level, shown in figure 2.4. We set the excited state energy to zero and thus the two ground states will have energy $-\hbar\omega_{1,2}$. The system is driven with light at frequencies $\omega_{1,2}^L$

$$\begin{aligned} H_A &= -\hbar\omega_1 |g_1\rangle\langle g_1| - \hbar\omega_2 |g_2\rangle\langle g_2| \\ H_{AF} &= \frac{\hbar\Omega_1}{2}\left(e^{i\omega_1^L}\sigma_1 + e^{-i\omega_1^L}\sigma_1^\dagger\right) \\ &\quad + \frac{\hbar\Omega_2}{2}\left(e^{-i\omega_2^L}\sigma_2 + e^{-i\omega_2^L}\sigma_2^\dagger\right) \end{aligned} \tag{2.20}$$

where $\sigma_\alpha = |g_\alpha\rangle\langle e|$ and where Ω_α is the Rabi frequency between the ground states and the excited state. We can remove the explicit time dependence by moving to a rotating frame, where state $|g_\alpha\rangle$ rotates at ω_α^L.

$$\begin{aligned} H_A &= \hbar\Delta_1 |g_1\rangle\langle g_1| + \hbar\Delta_2 |g_2\rangle\langle g_2| \\ H_{AF} &= \frac{\hbar\Omega_1}{2}\left(\sigma_1 + \sigma_1^\dagger\right) + \frac{\hbar\Omega_2}{2}\left(\sigma_2 + \sigma_2^\dagger\right) \end{aligned} \tag{2.21}$$

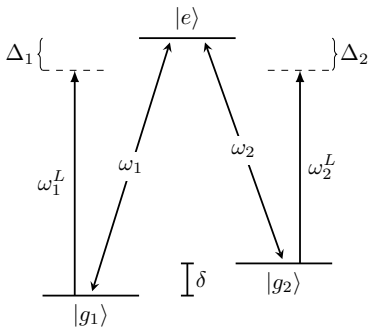

Figure 2.4 — A three-level system with two driving fields at frequency ω_α^L.

where $\Delta_\alpha = \omega_\alpha^L - \omega_\alpha$. Boosting the energies by $-\hbar\Delta$, where $\Delta = \frac{\Delta_1+\Delta_2}{2}$ and defining the two photon detuning $\delta = \Delta_1 - \Delta_2$ we can write the Hamiltonian as

$$H = \hbar\begin{pmatrix} \frac{\delta}{2} & 0 & \frac{\Omega_1}{2} \\ 0 & -\frac{\delta}{2} & \frac{\Omega_2}{2} \\ \frac{\Omega_1}{2} & \frac{\Omega_2}{2} & -\Delta \end{pmatrix}. \tag{2.22}$$

Assuming that $\Delta \gg \delta, |\Omega_{1,2}|$ we can assume the excited state to remain unpopulated and thus we can adiabatically eliminate the excited state, [Brion et al., 2007]. This allows us to rewrite the Hamiltonian into an effective two-level Hamiltonian,

$$H_{\text{eff}} = \hbar\begin{pmatrix} \frac{\delta}{2} + \frac{\Omega_1^2}{4\Delta} & \frac{\Omega_{RR}}{2} \\ \frac{\Omega_{RR}}{2} & -\frac{\delta}{2} + \frac{\Omega_2^2}{4\Delta} \end{pmatrix} \tag{2.23}$$

This Hamiltonian has the same form as for the two level atoms, eq. 2.13, but now with the Rabi frequency replaced by a Raman-Rabi frequency $\Omega_{RR} = \frac{\Omega_1\Omega_2}{2\Delta}$ and with an additional Stark shift of the atomic

levels $\frac{\Omega_\alpha}{4\Delta}$. This Stark shift can be eliminated using a multi-frequency drive described in chapters 6 and 8.

2.3 Laser cooling

In order to observe the effects described in the previous sections we have to cool down the atomic motion. Atoms at room temperature move at high speeds in random directions leading to inhomogeneous Doppler broadening of atomic transitions. Furthermore, the study of atoms trapped in potential wells of limited depth, requires the atoms to be sufficiently cold before loading.

In this work, the focus is on trapping atoms using the dipole force arising from the steep gradients of the evanescent field propagating along the outside of an optical nanofiber. In order to load atoms into such a trap we first have to cool the atomic motion.

2.3.1 Optical molasses

Since photons carry momentum, the absorption of a photon by an atom leads to a change in the momentum of the atom.

Atoms at room temperature have large momenta compared to photons and thus need to absorb many to slow down the motion. In order for resonant laser cooling to occur a closed optical loop is necessary. In Cesium, the transition between $|F = 4\rangle$ and $|F' = 5\rangle$ forms such a closed optical loop due to selection rules, see figure 2.5. This allows the atoms to continue to interact with the light, gradually slowing down the motion. The possibility of off-resonant excitations can lead to atoms leaving the optical loop and therefore a repumper is needed. The repumper acts on the $|F = 3\rangle$ to $|F' = 4\rangle$ transition to keep atoms out of $|F = 3\rangle$.

The motion of the atoms affects the interaction with the light due to Doppler shifts; atoms moving towards the beam will see blue shifted light whereas atoms moving away from the beam will see red shifted light. By tuning the lasers red of the transition, atoms moving towards the laser beam will interact more strongly with the light, see figure 2.6. For a two-level atom the fundamental cooling limit is the Doppler temperature,

$$k_B T_D = \frac{\hbar\Gamma}{2} \tag{2.24}$$

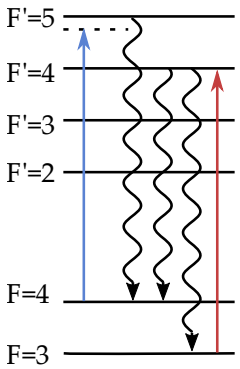

Figure 2.5 — Atomic transitions used for optical molasses cooling of Cesium atoms.

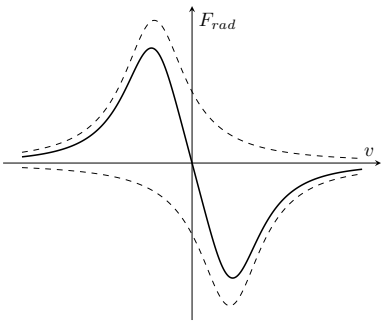

Figure 2.6 — The radiative force exerted by red detuned light as a function of the atomic velocity. Dashed lines are the force of each separate laser.

where Γ is the natural linewidth of the transition. For Cesium on the D2 line, the Doppler temperature is $T_D = 125\,\mu$K. It turns out, however, that multilevel atoms can be cooled down well below the Doppler temperature, due to effects of polarization gradient cooling, [Chu, 1992; Cohen-Tannoudji and Phillips, 1990].

The optical molasses technique allows for cooling of the atomic motion, but it does not offer trapping, as atoms at sufficiently low temperatures will be allowed to disperse out of the laser beams.

2.3.2 Magneto-optical trap

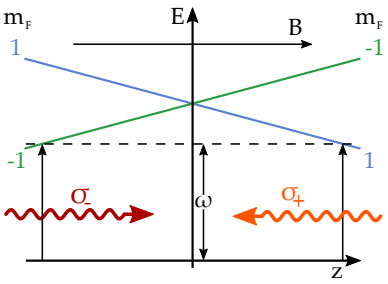

Figure 2.7 — A position dependent magnetic field tunes the atomic levels into resonance with the MOT beams.

The magneto-optical trap (MOT) is one of the most important developments in atomic physics and can be found in almost any AMO[2] lab. The MOT builds upon the optical molasses technique, but introduces a quadrupole magnetic field. The magnetic field strength is position dependent and allows for confinement of the atoms. The principle for a MOT is shown in figure 2.7, [Foot, 2005].

Counter propagating light with right- and left-hand circular polarization is detuned red w.r.t the cooling transition. The position dependent magnetic field brings the atoms into resonance with the molasses beams. This allows for both cooling and confinement of the atoms.

In figure 2.8 the setup for a MOT is pictured. Two coils are placed in Helmholtz configuration, with current flowing in opposite directions to generate a quadrupole field. Circularly polarized beams propagate from each of the cardinal directions. A cloud of atoms forms at the zero of the magnetic field.

[2] Atomic, molecular and optical physics

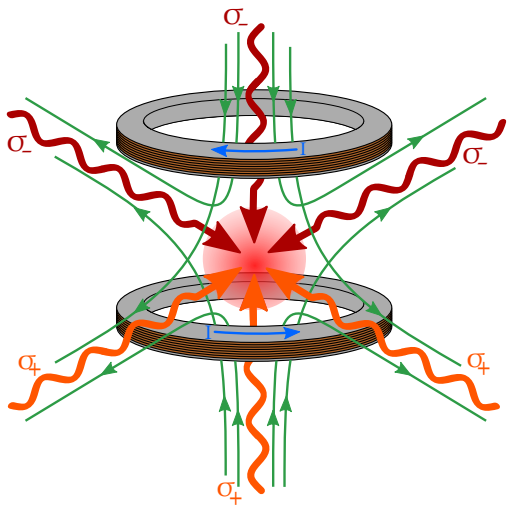

Figure 2.8 — A magneto-optical trap. A cloud of atoms is gathered using three pairs of counter-propagating beams with orthogonal circular polarization. The confinement of the trap is achieved using a pair of Helmholtz coils with the current running in opposite directions, forming a quadrupole magnetic field.

2.3.3 Sub-doppler cooling

It was observed that the cooling provided by the MOT alone was not enough to allow for efficient loading of the nanofiber dipole trap. For this reason a sub-doppler cooling procedure was implemented. Sub-Doppler cooling makes use of the polarization gradients formed by the counter-propagating MOT beams to establish a Zeeman state dependent Stark shift potential. The atomic motion on the scale of the optical wavelength allows for kinetic energy to be extracted via optical pumping into local dark states. This process allows for cooling significantly below the Doppler limit.

The cooling scheme used in this work is known as gray molasses or blue Sisyphus cooling (BSC), [Béguin, 2015; Boiron et al., 1996]. During BSC the cooler and repump beams are ramped down in frequency, while the power of the repump along with the magnetic field strength are ramped down. In the process of BSC the MOT cloud is compressed and the atoms will be left in the $F = 3$ manifold. The theoretical minimum temperature for this type of cooling is on the order of tens of the recoil temperature,

$$T_{rec} = \frac{\hbar^2 k^2}{2mk_B}, \tag{2.25}$$

which for the D2 line is 100 nK. Since we are ultimately interested in optimizing the loading of the dipole trap, the actual temperature reached during the sub-doppler stage is of secondary importance.

2.3.4 Resolved sideband cooling

In the regime where the confinement of atoms is sufficiently strong, the trap frequency becomes large enough that motional sidebands become resolved, [Wineland et al., 1998]. This allows for direct manipulation of the motional state of the atoms. To access these transitions in practice one needs a mechanism for coupling the motional states. In typical Raman spectroscopy this is done by counter propagating two beams. However, coupling can also be achieved by having a sufficiently steep spatial gradient of a single coupling beam. A steep gradient of the in-

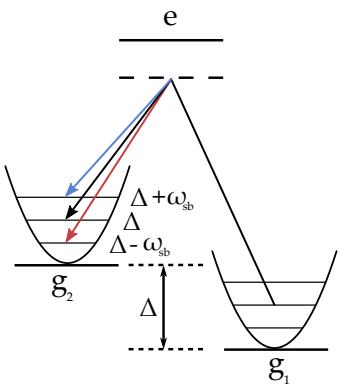

Figure 2.9 — The transfer of atoms between motional levels, through a virtual level. By matching the two photon detuning to the trap frequency atoms can be transferred to higher or lower motional states.

tensity can be written as the imaginary part of the k-vector of the Raman light. The electric field is thus,

$$\mathbf{E} = \mathbf{E}_0 e^{i(\beta z - \omega t)} e^{-\tilde{k} r}$$

where β is the normal propagation constant and where $\tilde{k}$ is the decay of the electric field in the r direction. The interaction of an atom in a motional state n will then be

$$\langle g, n | \, \mathbf{d} \cdot \mathbf{E} \, | e, n' \rangle = \langle g | \, \mathbf{d} \cdot \mathbf{E}_0 e^{i(\beta z - \omega t)} \, | e \rangle \, \langle n | \, e^{-\tilde{k} r} \, | n' \rangle$$

In the case of Raman transitions this interaction will be described by the product of electric fields, and thus the decay of the intensity, k, is

the relevant quantity. We can write the coordinate r as the position operator and quantize the motion. Assuming a harmonic potential the motional transitions can be written as

$$\langle n|\, e^{-k\hat{r}}\, |n'\rangle = \langle n|\, e^{-\eta(a+a^\dagger)}\, |n'\rangle \tag{2.26}$$

where we have introduced the creation and annihilation operators $a^{(\dagger)}$ and the Lamb-Dicke parameter, $\eta = k\sqrt{\frac{\hbar}{2m\nu}}$, where m is the mass of the atom and ν is the trap frequency. We can Taylor expand the exponential to find,

$$\langle n|\, e^{-\eta(a+a^\dagger)}\, |n'\rangle = \delta_{n,n'} + \eta\left(\sqrt{n}\delta_{n,n'-1} + \sqrt{n+1}\delta_{n,n'+1}\right) \tag{2.27}$$

$$+ \mathcal{O}(\eta^2) \tag{2.28}$$

where $\delta_{n,n'}$ is the Kronecker delta. From this we see that transitions, which increase the motional quantum number n, occur with a larger Rabi frequency than transitions which reduce the motional quantum number.

This coupling between motional states is what allows for cooling to occur. It is, however, important that the Lamb-Dicke parameter, η, is small in order to reduce the effects of recoil changing the motional state of the atom, [Wineland et al., 1998].

By measuring the interaction of the atoms with light we can also infer information about the motional state of the atoms. The atoms will be resonant with light, at two-photon detunings $\Delta = \pm 2\pi \times \nu$, where ν is the trap frequency. The motional energy of the atom will be increased at a detuning equal to $+2\pi\nu$, whereas the energy will be reduced for $\Delta = -2\pi\nu$, see figure 2.9. The steep intensity gradient of the Raman light is, in our experiment, achieved using the evanescent field of nanofiber guided light, described in chapter 3.

Many different resolved sideband cooling schemes exist, such as [Østfeldt, 2017] and [Albrecht et al., 2016], but the discussion in this work will be limited to the cooling scheme carried out in the Raman sideband spectroscopy experiments. This cooling scheme is known as degenerate Raman cooling.

2.3.4.1 Degenerate Raman cooling

Strong gradients of magnetic fields can lead to coupling between adjacent degenerate Zeeman levels of the atom, figure 2.10. The adjacent Zeeman levels can be tuned into degeneracy with the motional levels,

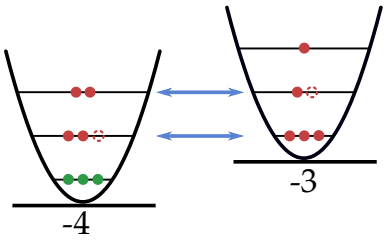

Figure 2.10 — The coupling between degenerate motional states allows for transfer of atoms. The motional ground state of $|m_F = -4\rangle$ is decoupled.

i.e. making $|m_F, n\rangle$ degenerate with $|m_F + 1, n - 1\rangle$, by proper choice of the bias magnetic field, [Meng et al., 2018].

By pumping atoms with σ^- polarized light the atoms will gradually lose motional quanta. The lowest motional state of $|F = 4, m_F = -4\rangle$ does not couple to adjacent states through the fictitious magnetic field. In this process atoms accumulate in the motional ground state of $|F = 4, m_F = -4\rangle$.

In practice we generate these strong magnetic field gradients using the fictitious magnetic field of the nanofiber trap lasers. An in-depth treatment of the cooling scheme along with the experimental implementation can be found in [Markussen, 2020].

2.4 Optical pumping

An important tool in atomic physics is the ability to prepare atoms in well-defined states. This ensures that the interaction is the same for the entire ensemble and increases the number of accessible atoms. By proper choice of frequency and polarization, atoms can be pumped into states which are decoupled from the light, also known as dark states. One way of preparing the atoms is by making use of a linearly polarized pump on the $|F = 4\rangle \rightarrow |F' = 4\rangle$ transition. The transition between $|F = 4, m_\mathrm{F} = 0\rangle \rightarrow |F' = 4, m'_\mathrm{F} = 0\rangle$ is dipole forbidden and can therefore not be driven by the linearly polarized pumping light. Due to the possibility of spontaneous decay from $|F' = 4\rangle$ into the $|F = 3\rangle$ manifold a repumper is required. The repumper drives atoms out of the $|F = 3\rangle$ manifold and allows them to spontaneously decay into $|F = 4\rangle$. This means that the atoms will gather in the dark state $|F = 4, m_F = 0\rangle$ over time, the optical pumping scheme is shown in figure 2.11. The atoms in $|F = 4, m_F = 0\rangle$ can then be transferred to $|F = 3, m_F = 0\rangle$ using a resonant microwave π-pulse and any remaining atoms in the $|F = 4\rangle$ manifold are blown away using a pulse from the MOT cooler.

An analogous procedure can be carried out to prepare atoms in the stretched levels. A σ-polarized optical pumping beam brings the atoms into the extreme m_F levels. A subsequent σ-polarized microwave π-pulse then brings the atoms into $|F = 3, m_F = \pm 3\rangle$.

In the practical implementation of this scheme, for atoms trapped around an optical nanofiber, the optical pumping beam is modulated at 20 MHz resulting in two frequency components at ± 20 MHz w.r.t the $|F = 4\rangle \rightarrow |F' = 4\rangle$ transition. This ensures that the light is not absorbed

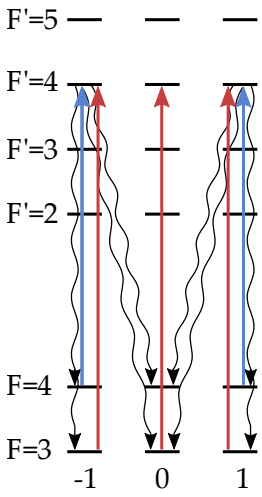

Figure 2.11 — Scheme for preparing atoms in the $|F = 3, m_F = 0\rangle$ state. The cooler drives atoms from $F = 4$ to $F' = 4$, however the transition between $|F = 4, m_F = 0\rangle$ and $|F' = 4, m_F = 0\rangle$ is dipole forbidden, leading to the accumulation of atoms in $|F = 4, m_F = 0\rangle$. A repumper ensures that atoms in the $F = 3$ manifold are brought back into $F = 4$.

and can propagate through the entire atomic ensemble without exerting a dipole force on the atoms, [Østfeldt, 2017].

A typical optical pumping signal is shown in figure 2.12. We see that after turning on the repumper we get an additional amount of signal due to the atoms residing in other levels than $|F = 3, m_F = 0\rangle$. The repumped signal serves as a useful reference to the total number of trapped atoms and will be used extensively to compare different measurement with varying signal levels.

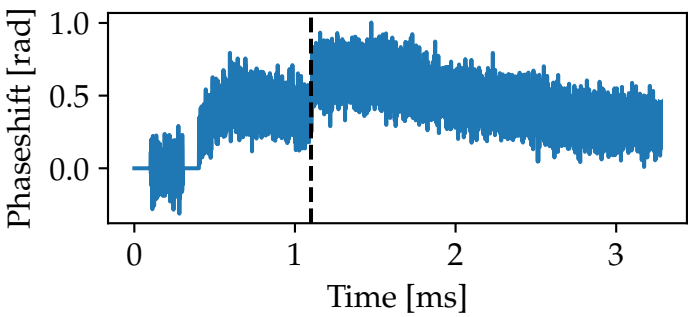

Figure 2.12 — Signal showing optical pumping. The vertical dashed line indicates the repumper being turned on.

CHAPTER

3 LIGHT PROPAGATION IN NANOFIBERS

In this chapter the propagation of light in sub-wavelength optical fibers will be presented. The derivation of the equations presented in this chapter is somewhat involved and will not be covered - the focus will be on exploring the consequences of the solutions. Detailed derivations can be found in sources such as [Béguin, 2015] and [Vetsch, 2010].

3.1 Modes of Propagation

A typical optical fiber consists of a silica core, surrounded by a silica cladding, shown in figure 3.1. Impurities are added to the core to slightly increase the refractive index.

Light propagating in a medium with higher refractive index than the surroundings can totally internally reflect, given the angle of incidence is larger than the so called critical angle. In the geometrical optics picture this can be seen as the limiting angle of the acceptance cone of the waveguide. In the limit of small waveguides ($a \approx \lambda$) the geometrical picture is no longer valid and the full Maxwell's equations have to be employed,

$$\begin{aligned} \vec{\nabla} \times \vec{H} &= \epsilon(r)\frac{\partial \vec{E}}{\partial t}, & \vec{\nabla} \cdot H &= 0 \\ \vec{\nabla} \times \vec{E} &= -\mu_0 \frac{\partial \vec{H}}{\partial t}, & \vec{\nabla} \cdot (\epsilon(r)\vec{E}) &= 0 \end{aligned} \tag{3.1}$$

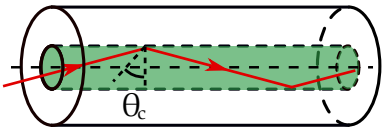

Light can be guided when the angle of reflection is larger than the critical angle

$$\theta > \sin^{-1}\left(\frac{n_2}{n_1}\right) = \theta_c$$

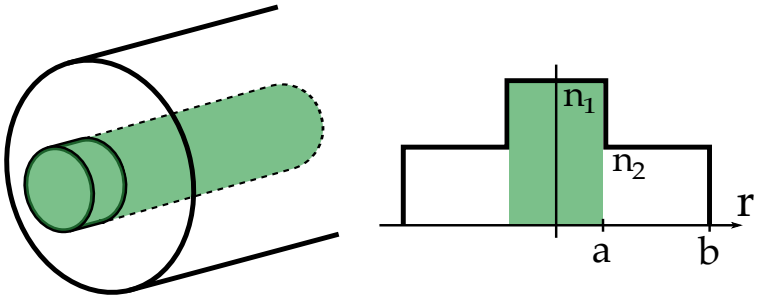

Figure 3.1 — Illustration of a step-index optical fiber. The core of the fiber has a refractive index of n_1 and is surrounded by a cladding with refractive index n_2

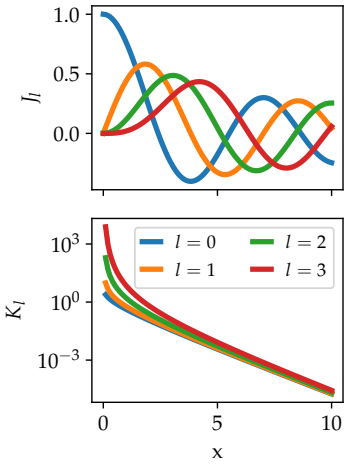

Figure 3.2 — Plot of the unmodified(top) and modified(bottom) Bessel functions. Note the log scale of the bottom panel.

where $\vec{E}$ is the electric field, $\vec{H}$ is the magnetic field, μ_0 is the vacuum permeability and $\epsilon(r)$ the permittivity of the medium, here a function of the radial coordinate r. The wave equation can readily be derived from Maxwell's equations,

$$\vec{\nabla}^2\vec{E} - \mu_0\epsilon(r)\frac{\partial^2\vec{E}}{\partial t^2} = -\vec{\nabla}\left[\frac{\vec{E}\cdot\vec{\nabla}\epsilon(r)}{\epsilon(r)}\right], \tag{3.2}$$

with an equivalent differential equation for the magnetic field. For the geometry of a fiber optic waveguide the problem decomposes into two regions; inside the core ($r < a$) and inside the cladding ($r > a$). Inside the core of the fiber, the solutions to equation 3.2 are described in terms of Bessel functions of the first kind J_l, where l is the order of the Bessel function. In the cladding of the fiber, the solutions are described in terms of modified Bessel functions of the second kind K_l, see figure 3.2. The propagation modes in a waveguide are described by effective propagation constants, β. Finding the allowed values of β amounts to solving a transcendental equation,

$$\begin{aligned}\frac{J_l'(ha)}{haJ_l(ha)} = &-\frac{K_l'(qa)}{qaK_l(qa)}\left(\frac{n_1^2+n_2^2}{2n_1^2}\right) \\ &\pm\sqrt{\left(\frac{n_1^2-n_2^2}{2n_1^2}\right)^2\left[\left(\frac{K_l'(ha)}{qaK_l(qa)}\right)^2+\left(\frac{2l\beta k_0 n_1^2}{h^2q^2a^2}\right)\right]},\end{aligned} \tag{3.3}$$

where a is the core radius, n_1 and n_2 the refractive index of the core and cladding, respectively, J_l and K_l the unmodified and modified Bessel

functions, respectively and where h and q are given by,

$$h = \sqrt{k_0^2 n_1^2 - \beta^2} \tag{3.4}$$
$$q = \sqrt{\beta^2 - k_0^2 n_2^2}. \tag{3.5}$$

Here $k_0 = \frac{2\pi}{\lambda}$ is the vacuum propagation constant and $1/h, 1/q$ are the decay lengths of the modes inside and outside of the core, respectively. The different solutions describe different modes of propagation. We are interested in finding the situation where only one mode is guided by the fiber. From the solutions, a cut-off mode parameter can be found,

$$V \equiv \frac{2\pi a}{\lambda}\sqrt{n_1^2 - n_2^2} < 2.405, \tag{3.6}$$

where V is the mode parameter, λ the wavelength and where the cutoff is $V_C = 2.405$. Obeying this inequality ensures that only one mode is guided by the fiber. This fundamental mode is also known as HE_{11}, shorthand for hybrid electric - hybrid referring to the fact that there is a non-vanishing longitudinal component of the field.
The HE_{11} mode has two polarizations, with the electric field outside the core($r > a$) given by,

$$\mathcal{E}_z^{\pm}(r,\phi) = CK_1(qr)\text{exp}[\pm i\phi] \tag{3.7}$$
$$\mathcal{E}_r^{\pm}(r,\phi) = -C\frac{i\beta}{2q}[K_2(qr)(1+s) + K_0(qr)(1-s)]\text{exp}[\pm i\phi] \tag{3.8}$$
$$\mathcal{E}_\phi^{\pm}(r,\phi) = \pm C\frac{\beta}{2q}[K_0(qr)(1-s) - K_2(qr)(1+s)]\text{exp}[\pm i\phi], \tag{3.9}$$

where $\mathcal{E}^{+(-)}$ refers to the right-hand (left-hand) quasi-circular polarization, C is a constant proportional to the power and where

$$s = \left[\frac{1}{(ha)^2} + \frac{1}{(qa)^2}\right]\left[\frac{J_1'}{haJ_1(ha)} + \frac{K_1'}{qaK_1(qa)}\right]. \tag{3.10}$$

From the two quasi-circular polarization modes, a quasi-linear polarized mode can be constructed,

$$\mathcal{E}^{\uparrow}(r,\phi) = \frac{\mathcal{E}^{+}(r,\phi) + \mathcal{E}^{-}(r,\phi)}{\sqrt{2}} \tag{3.11}$$
$$\mathcal{E}^{\rightarrow}(r,\phi) = \frac{\mathcal{E}^{+}(r,\phi) - \mathcal{E}^{-}(r,\phi)}{\sqrt{2}}. \tag{3.12}$$

The transverse components of the quasi-linear polarization are in phase and behave like a linearly polarized mode. The longitudinal component, $\mathcal{E}_z$, is $90°$ out of phase with the transverse components leading to an elliptical polarization parallel to the fiber axis. The longitudinal component depends on the radial as well as azimuthal coordinate and thus the ellipticity and helicity of the elliptical polarization varies around the fiber. The magnitude of the longitudinal component is maximal in the plane of the polarization and zero in the plane perpendicular to the polarization direction.

The electric field outside the core for the fundamental mode propagates as an evanescent wave. Due to it being fiber guided there is no diffraction of the evanescent field. The fast decay in addition to the diffraction-less propagation are very desirable features for atomic physics. In a standard optical fiber the evanescent field is fully contained within the cladding. Therefore, to access this evanescent field we, effectively, need to replace the cladding with free space. For a core-air guided mode the numerical aperture will be close to one, $NA = \sqrt{n_1^2 - n_2^2} \approx 1$, where $n_1 \approx 1.5$ and $n_2 = 1$. Using equation 3.6 we see, that the single mode condition can be fulfilled, at the appropriate wavelengths ($780,\ 852,\ 1060$ nm) for a core-air interface if the radius of the core is < 300nm.

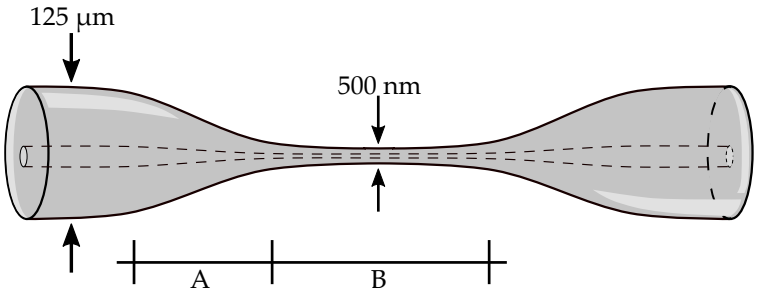

Figure 3.3 — Illustration of an optical nanofiber. An optical fiber with a diameter of $125\,\mu m$ is gradually tapered (Region A) down to a diameter of $500\,nm$.

Figure 3.3 depicts an illustration of an optical nanofiber. The standard $125\,\mu$m single-mode fiber is tapered down to a waist section of only 500 nm. At the waist the core becomes so thin that it can no longer effectively guide the light and the light becomes cladding guided, with the cladding now acting as the core and with free space acting as the cladding. The fiber guided mode is allowed to be guided through the

tapered region provided the taper angle is smaller than a certain threshold, this is discussed in finer detail in chapter 5.
As the diameter of the fiber decreases the power of the evanescent field increases.

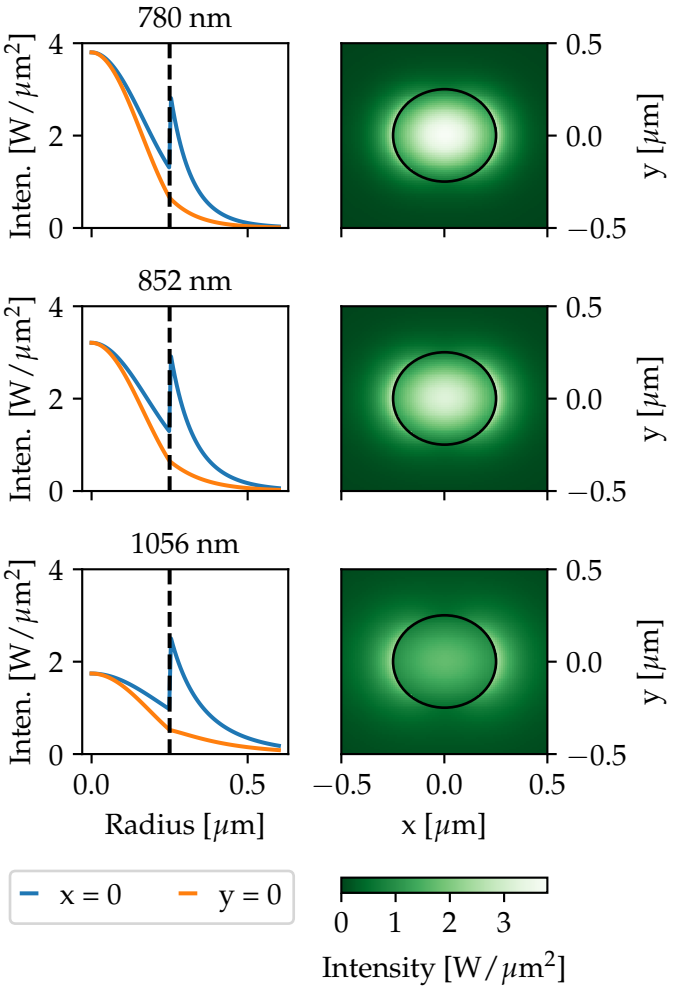

Figure 3.4 — Intensity distributions for different wavelengths. Left column shows radial intensity distribution for $x = 0$ and $y = 0$. Right column shows the transverse intensity distributions black circles indicate the fiber periphery.

3.2 Evanescent Field

For fiber diameters smaller than the wavelength of the guided light a large proportion of the guided light propagates as an evanescent field.

The intensity distribution is dependent on the direction of polarization, leading to an azimuthally dependent intensity. Plotted in figure 3.4 are the transverse intensities for three relevant wavelengths in our experiment. The left column shows the radial decay of the field.

The decay length of the evanescent field depends on the wavelength of the light - larger wavelengths have longer decay lengths. It is also apparent that the intensity of the evanescent field is larger along the axis of polarization. For a propagation mode as complicated as this, the polarization pattern becomes highly non-trivial.

3.2.1 Polarization

The polarization pattern of the fundamental mode of a nanofiber is somewhat complicated. The polarization pattern of the quasi-linear polarization are plotted in figure 3.5. The transverse components are nicely in phase and behave like a linear polarization. In figure 3.5 the colormap refers to the ratio of the imaginary part of the longitudinal field to the horizontal component. This gives us an indication of the ellipticity of the field. The ellipticity changes sign on the two sides of the fiber and is maximal along the quasi-linear polarization direction. Comparing the polarization pattern to the intensities in figure 3.4 we see that the region of highest intensity is also the region of maximum ellipticity. As shown in chapter 2.2.1 the presence of circular polarizations give rise to vector light shifts. These fictitious magnetic fields can be a significant nuisance in the experiment due to the steep radial gradients of the evanescent fields. The quasi-linearly polarized electric field is plotted in figure 3.6 for different points in time. The longitudinal elliptical polarization can be cancelled by counter-propagating light, polarized in the same direction. The resulting polarization pattern is locally linear at every point but with the polarization direction rotating along the axis of the fiber see appendix A.

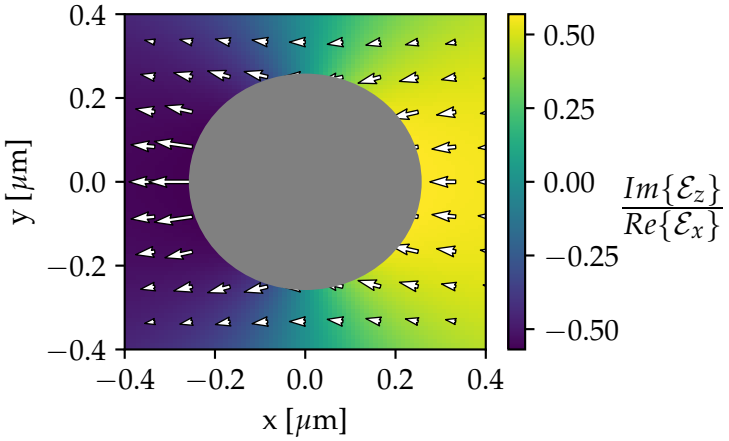

Figure 3.5 — Plot of the polarization pattern of the evanescent field of a 500 nm fiber. Arrows indicate the transverse polarization direction, here horizontal. The fiber cross-section is indicated by the grey circle. Colormap indicates the ratio of $\frac{Im\{\mathcal{E}_z\}}{Re\{\mathcal{E}_x\}}$ showing the distribution of elliptically polarized light. The ellipticity goes to zero along $x = 0$ and is maximum and changes sign along $y = 0$

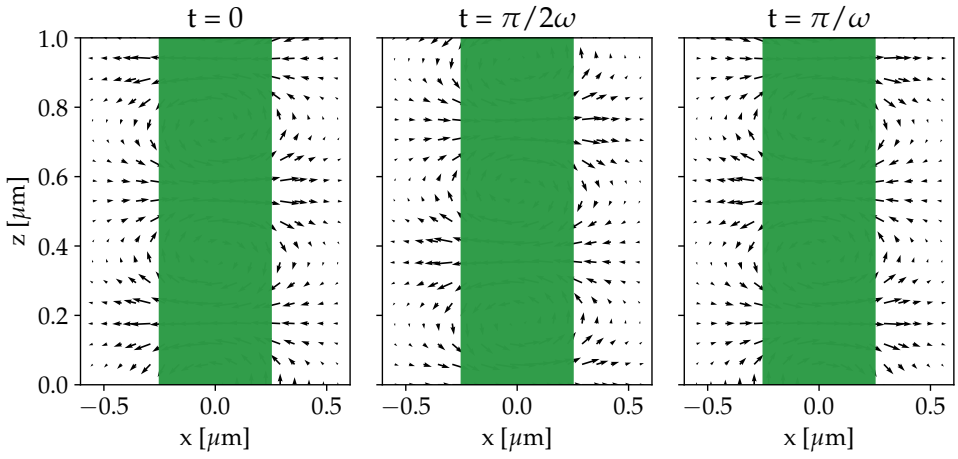

Figure 3.6 — Longitudinal plot of quasi-linearly polarized electric field at different points in time.

CHAPTER

4 NANOFIBER ATOM TRAP

In chapter 2 we saw how an intensity gradient of far off-resonant light leads to a dipole force, the strength of which depends on how steep the gradient of the intensity is. In chapter 3 we found that the evanescent field around an optical nanofiber has near exponential decay along with diffraction-free propagation; suitable properties for generating strong dipole forces.

In this chapter some of the considerations for building a nanofiber trap are presented.

4.1 Trap Potential

Shown in chapter 2, the presence of a red detuned light field induces a dipole force, pulling the atom towards the high intensity region. The surface of the fiber also induces a short range Van der Waals force which attracts atoms towards the surface of the fiber [Boustimi et al., 2002]. We want to keep the atoms from reaching the surface of the fiber since this will lead to the atoms being ejected from the trap. We can create a barrier towards the surface of the fiber by utilizing a blue detuned trap field. The wavelengths chosen for the nanofiber trap are far detuned from the D2 line, allowing us to disregard the hyperfine splitting of the excited state manifold. Since the detuning is still at the same magnitude as the fine structure splitting, the tensor shift will be determined by the J quantum number. For the ground state of Cesium this is equal to

$1/2$, cancelling the tensor shift of the ground state manifold. The vector light shift can be cancelled by making sure that the local polarization is linear. This is important as it ensures that the atoms feel the same dipole force regardless of which ground state hyperfine level they are in.

Different trap schemes, using so called "magic" wavelengths, allow for simultaneous cancellation of differential Stark shifts on both the ground and excited state manifolds, [Lacrôute et al., 2012].

In chapter 3 we saw how the evanescent field around a nanofiber has a near exponential decay and that this decay length depends on the wavelength of the light. This property turns out to be critical for establishing a dipole trap around a nanofiber.
As seen in equation 2.18, a far detuned field induces a dipole potential

$$U_{\text{dip}}(r) = \frac{\hbar\Omega^2(r)}{4\Delta}, \tag{4.1}$$

where $\Omega(r) = \frac{\langle e|\mu|g\rangle E(r)}{\hbar}$ is the Rabi frequency and Δ is the detuning of the field. This potential depends on the square of the Rabi frequency and thus is linear in intensity. Modelling the evanescent field around the nanofiber as a decaying exponential function we can write the potential due to red- and blue detuned light as

$$U(x) = B\mathrm{e}^{-x\kappa_b} - R\mathrm{e}^{-x\kappa_r}, \tag{4.2}$$

where B, R are the Stark shifts due to the blue- and red detuned fields, respectively, and κ_b, κ_r the decay constant of the blue- and red detuned fields, respectively. The existence of a local trap minimum is guaranteed if $B > R$ and $\kappa_b > \kappa_r$. Since we are free to choose the power of the trap fields the first condition is easily met. We know that larger wavelengths have longer decay lengths, therefore the second requirement is also met.
The rotational asymmetry shown in figure 3.4 allows for azimuthal confinement of the atoms; by making the blue trap orthogonally polarized w.r.t. the red trap we limit the azimuthal extent of the potential. Additionally two counter-propagating red beams are used, forming a standing wave. The standing wave modulates the potential along the axis of the fiber, leading to trap-sites every half wavelength.

The trap potential is shown in figure 4.1 for a red detuned field at $1056\,\text{nm}$ and a blue detuned at $783\,\text{nm}$. In the left panel we see the azimuthal confinement, made possible by the orthogonally polarized

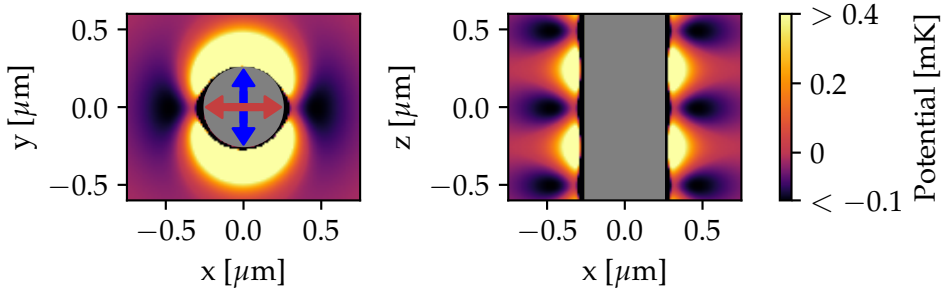

Figure 4.1 — Plot of the trap potential around a 500 nm fiber. The potential is formed using an attractive field at 1056 nm(red arrow, left panel) and a repulsive at 783 nm(blue arrow, left panel). The powers used are $P_{\text{red}} = 2 \times 0.7\,\text{mW}$ and $P_{\text{blue}} = 2 \times 4\,\text{mW}$. Left panel shows the periodic nature of the standing wave trap.

beams. The standing wave formed by the two red detuned beams results in a periodic potential in the axial direction, shown in the right panel.

In the experimental implementation of the nanofiber trap we use two counter propagating blue beams, detuned from each other by $\sim 0.5\,\text{nm}$. Since this frequency difference is several orders of magnitude higher than the trap dynamics the modulation of the trap will be averaged out. This allows us to cancel the longitudinal circular polarization of the evanescent field, eliminating vector light shifts from the blue trap laser.

Figure 4.2 depicts the radial potential, along the polarization of the red detuned trap field. Close to the fiber surface the Van der Waals force dominates. The significant anharmonicity of the potential is an important feature of the nanofiber trap and will be studied in more detail in chapters 11 and 12.

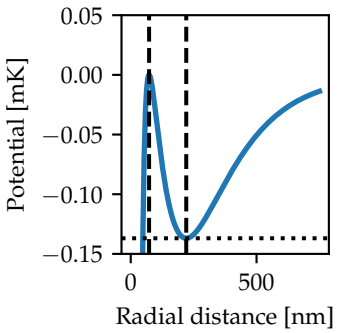

Figure 4.2 — Potential along the red trap polarization direction. Powers are $P_{\text{blue}} = 2 \times 4\,\text{mW}$ and $P_{\text{red}} = 2 \times 0.7\,\text{mW}$. Note the anharmonicity of the potential. Dashed lines indicate location of potential minimum and maximum, the horizontal dotted line indicates the potential minimum.

4.1.1 Collisional Blockade Regime

The strong confinement of the atoms trapped around the nanofiber allows us to operate in the collisional blockade regime, [Schlosser et al., 2002]. In this regime no more than one atom may occupy each trap site, due to atom-to-atom collisions becoming the dominant loss mechanism. The verification that we in practice operate in the collisional blockade regime is challenging, but it is generally assumed that nanofiber traps

do operate in the collisional blockade regime, [Vetsch, 2010; Béguin, 2015].

4.1.2 The Lamb-Dicke regime

A major point of interest in the study of dipole traps is the manipulation of the motional states. In chapter 2.3.4 the Lamb-Dicke parameter, η, was introduced in the context of motional transitions. We found, that the Lamb-Dicke parameter has to be sufficiently small for the resolution of motional transitions, [Wineland et al., 1998]. We find that the Lamb-Dicke parameter can be related to the recoil frequency of the trapped atom

$$\frac{\omega_r}{\omega_{\text{trap}}} = \eta^2.$$

This tells us that we need to have a trap frequency which is significantly larger than the recoil frequency to minimize the likelihood of motional state changing spontaneous scattering events. In chapter 7 and 9 we will see that the trap frequency of a potential like the ones in figures 4.1 and 4.2 are $\sim 90\,\text{kHz}$, whereas the recoil frequency of the D2-line is $2\,\text{kHz}$.

Part II

Experimental Work

CHAPTER

5 NANOFIBER FABRICATION, CHARACTERIZATION, AND INSTALLATION

On the 5th of may 2019 our nanofiber Bertha was hit by a rogue piece of dust. This meant that we had to take the fiber out and replace it with a new nanofiber.

The work of pulling a new fiber took place within a preexisting pulling setup, which had been sitting unused since 2017. Because of this we had to reestablish the setup and learn the procedures. This was made possible, in part, due to the help of Jürgen Appel who graciously took out time to help us get to know the setup early in the process.

The process of pulling, characterizing and installing our new nanofiber, named Didrik, in our setup will be presented in this chapter.

5.1 Overview of fiber pulling setup

In this section a brief overview of the main components of the fiber pulling rig will be given.
The fiber pulling takes place inside a flow box [1] to reduce the amount of dust in the air. A simplified diagram of the pulling setup is pictured in figure 5.1.

The setup consists of the linear stages, (1), which are used to clamp and pull the fiber. To make the fiber malleable a hydrogen-oxygen flame is produced by a nozzle (2), supplied by high-pressure flasks of hydrogen and oxygen (3). The flow of hydrogen and oxygen is regulated

[1] Shilling engineering: CleanProCel

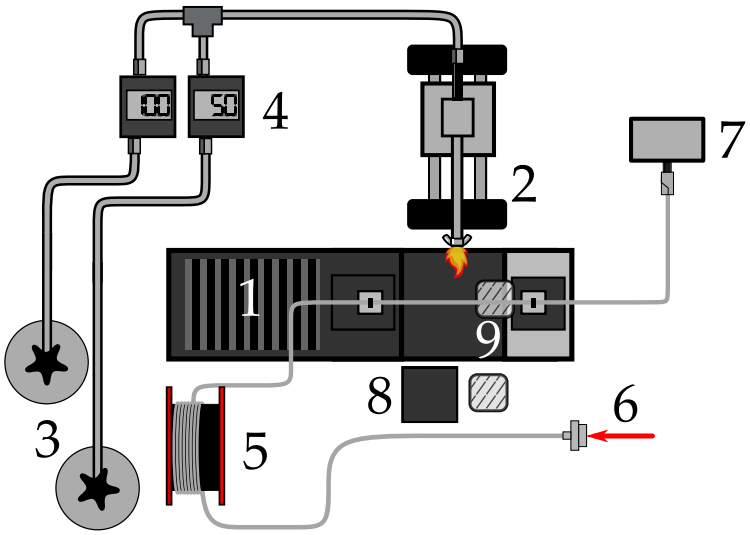

Figure 5.1 — Simplified diagram of the pulling setup. The different numbered sections are described in the text. Figure heavily inspired by [Pedersen, 2017].

using a set of gas flow regulators, (4). The fiber is derived from a spool of Thorlabs 780HP single-mode fiber (5). Light at relevant wavelengths (780, 852, 1056 nm) is coupled into the fiber (6) and monitored during the pulling sequence using a homebuilt photodetector (7). A magnetic base (8) allows for easy installation and removal of the fiber camera, probe fiber and nanofiber tuning-fork holder. Laser pointers are positioned from the side and from the top of the stages, (9), to allow for alignment of the stages.

5.1.1 Fiber cleaning and inspection

The unjacketed Thorlabs 780HP fiber comes equipped with a protective layer of acrylate. This coating needs to be removed prior to pulling as any remnant will produce soot on the surface of the fiber during burning. The coating is stripped off using an oven stripper, which heats up the coating allowing it to subsequently be scraped off using a pair of blades. The fiber is finally wiped off with acetone or ethanol to remove any remnants of the coating.

The fiber is imaged with a camera after stripping to ensure that the coating has been fully removed. The camera is mounted on a magnetic plate (8) and the fiber is moved, using the stages, very slowly(~ 0.5 mm/s) underneath the camera. If any dirt is present the fiber is

wiped off once again. It typically requires a handful of attempts before the fiber is sufficiently clean to proceed with the pulling process.

Fibers meant to go into vacuum are typically discarded after two or three unsuccessful cleanings as the wiping might introduce micro-fractures in the fiber, which can reduce the survivability.

5.1.2 Stage alignment

To avoid asymmetry of the nanofiber we need to ensure that the pulling stages are properly aligned. Misalignment of the stages can lead to unpredictable nanofiber widths and can lead to the fiber breaking during the pulling procedure.

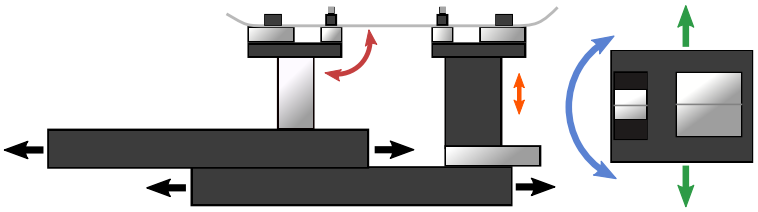

Figure 5.2 — Illustration of the pulling stages. Left panel shows the stages in profile. Right panel shows a top-down view of the fiber slots. the upper stage can move independently of the lower stage. The pitch and yaw can be adjusted for both stages. The right stage allows for both vertical and horizontal adjustment.

The pulling stages are pictured in figure 5.2. The pulling stages, made by Steinmeyer[2], are two separate linear stages, stacked on top of one-another. The top stage can move independently of the bottom stage. Moving the bottom stage allows for translation of the entire pulling setup. This is useful as it allows for linear movement of the fiber which is important for inspection purposes as well as characterization. The stages are driven by servo motors with PID control for the position and velocity[3].

The right panel of figure 5.2 shows a top down view of the stages. Both the top and bottom stage have yaw and pitch degrees of freedom. The bottom stage additionally allows for XYZ-translation. The stages have V-grooves for seating a stripped fiber. The fiber is then held in place using a clamp and a rubberized magnet.

[2]PMT-160-150-DC05-R and PMT-160-050-DC38-R
[3]Galil DMC-2143

The alignment of the stages can be carried out in two different ways. The first is using the diffraction pattern of a green laser pointer. At the two points (9) in figure 5.1, laser modules can be installed. The one from above allows us to align the yaw of the stages, while the one from the side allows for pitch alignment. The alignment is carried out by putting a stripped fiber end into the fiber clamps. The fiber is then periodically moved backwards and forwards. If the diffraction pattern created by the fiber changes, the alignment can be adjusted to compensate. We use a fiber end since using a full piece of fiber, bridging the gap between the two stages, would result in the fiber being tensioned, which would be released as the fiber elongates during pulling. To make the XYZ-alignment we first place a stripped fiber across the two stages. We then take a picture of the fiber at the top stage and move the bottom stage. If the image at the bottom stage is shifted laterally or out of focus we adjust this with the bottom stage. This is the method reported to be the most effective in past incarnations[Pedersen, 2017]. However we found that this method was not always reliable.

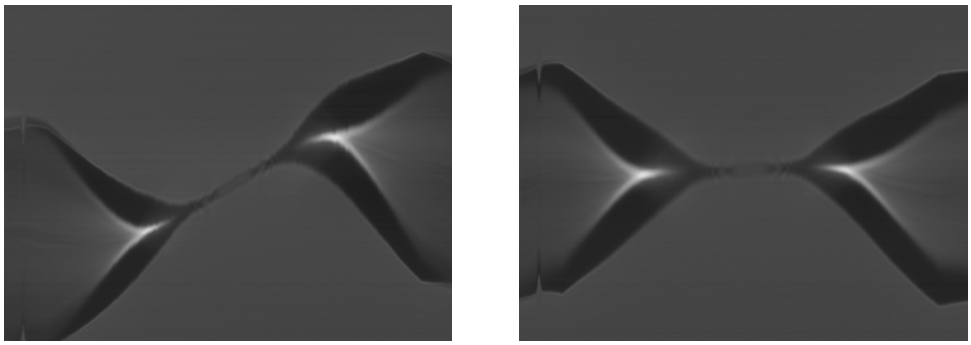

Figure 5.3 — Images of pulled fibers. Left panel shows badly aligned yaw of the stages. The right panel shows good alignment of the stages. Note that these images are not to scale with the horizontal direction compressed by a factor of 40.

The second method for aligning fibers involves pulling a piece of fiber, taking an image of the fiber, like the ones seen in figure 5.3, and seeing if there is any misalignment. By adjusting the alignment, pulling a fiber and then imaging we can gradually improve the alignment. While this method is slow and cumbersome it is at times the best way to reliably achieve proper alignment of the stages.

5.1.3 The Flame

Fiber pulling relies on creating a small hot zone where the fused silica of the fiber transitions and becomes fluid. The temperature at which this occurs is above $1500°$ K. In order to produce such a flame we use a $2:1$ hydrogen-oxygen mixture, controlled by gas flow regulators[4], (4). The flame is sufficiently hot and its only biproduct is water, which evaporates off of the fiber. A nozzle (2), custom made by the NBI mechanical workshop, is used to produce the flame. The nozzle is mounted on rails that allow it to be moved away from and towards the fiber. The flame is ignited using the spark from a normal gas lighter.

In the past the nozzle performed inconsistently, with flashbacks into the nozzle, leading to the extinction of the flame, or the flame simply not being hot enough. This was typically accompanied by a high-pitched tone emitted by the nozzle and a red glow of the tip of the nozzle.

We found that the inconsistencies of the nozzle could be ameliorated by introducing a heatsink. A wingnut was cut and pressure fit over the tip of the nozzle. This greatly improved the stability and after this modification there were seldom any issues with the performance of the flame.

5.1.4 Pulling procedure

The fibers used for pulling are single mode at wavelengths of $780\,\text{nm}$ and above. To ensure that no higher order modes are excited as the fiber is tapered down to the desired radius of $\sim 250\,\text{nm}$ we need to make sure that the tapering is adiabatic. This can be achieved if the taper angle is much smaller than the limiting angle[Love et al., 1991],

$$\Omega(z) = a\frac{\beta_{01} - \beta_{02}}{2\pi}, \tag{5.1}$$

where a is the fiber radius, β_{01} and β_{02} are the propagation constants for the fundamental and first excited mode. The limiting angle for relevant wavelengths is plotted in figure 5.4. The simplest way to ensure that one stays below this limiting angle is by using a linear taper. We use a linear taper with a taper angle of $2\,\text{mrad}$.

The pulling algorithm makes use of small consecutive asymmetric pulls, gradually building the linear taper. The pulling trajectory is preprogrammed and was optimized by Freja T. Pedersen, [Pedersen, 2017]. During the pulling procedure the transmission is monitored using light

[4]Omega: FMA 5510-ST

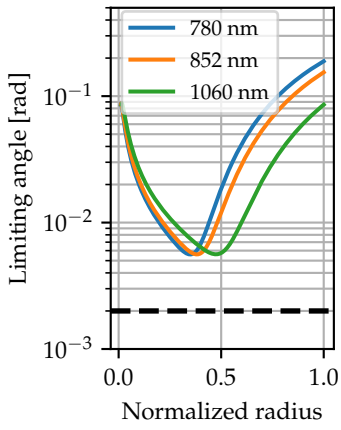

Figure 5.4 — Limiting angle for 780 nm, 852 nm and 1060 nm. Dashed line marks the 2 mrad taper angle chosen for fiber pulling.

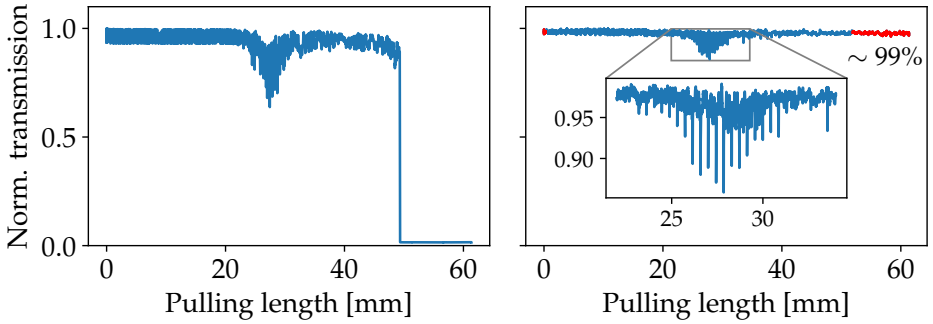

Figure 5.5 — Plot of nanofiber transmission during pulling. Left panel shows a bad pull, where the fiber broke. Right panel shows a good pull with transmission of $\sim 99\,\%$. Inset shows the periodic dips in signal halfway through the pull.

at $852\,\text{nm}$. Figure 5.5 shows transmission data for two fiber pulls; one where the fiber broke and one where it survived.

The periodic dips in signal between $25\,\text{mm}$ and $30\,\text{mm}$ pulling length appear when the fiber diameter approaches the point where the limiting angle is minimal. The dips occur synchronized with the turning points of the pulling sequence which speaks for it being related to intermediate large taper angles while the linear taper is being built. These lead to the excitation of higher order modes which cause interference. These dips subside however and transmissions of $> 99\,\%$ are routinely achieved.

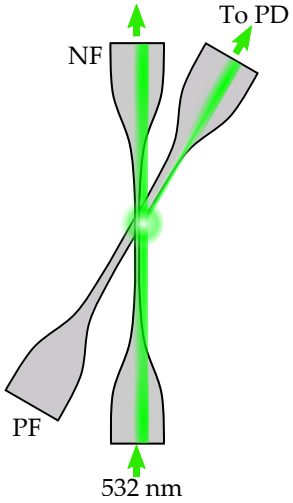

Figure 5.6 — Probe fiber setup. A $\sim 1\,\mu$m thick probe fiber(PF) is pushed against the nanofiber(NF), allowing for evanescent coupling of higher order modes.

5.1.5 Waist Measurement

The waist characterization is done using the method of higher order mode beats, [Fatemi et al., 2017]. The guided modes of a fiber are governed by their respective propagation constants β. By sending light at $523\,\text{nm}$, which is below the single mode cutoff, through the nanofiber we get excitation of higher order modes. The evanescent field can then be picked up by a probe fiber with a diameter of a few μms by making the two touch, figure 5.6. The probe signal is shown in figure 5.7.

The difference in propagation constant for different modes gives rise to interference as the nanofiber is moved across the probe fiber. The beat frequencies can be found using a Fourier transform, however in order to preserve spatial information, i.e. position along the nanofiber, we use

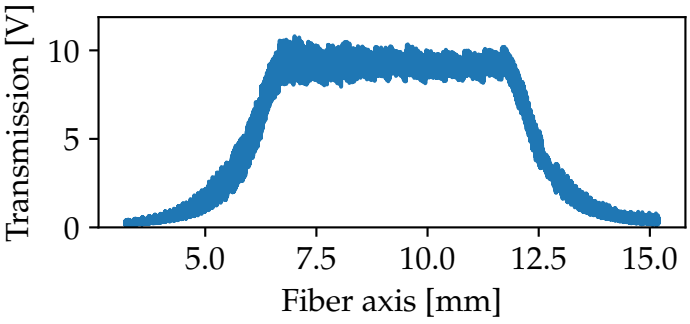

Figure 5.7 — Signal from probe fiber taken with a scanning speed of $0.1\,\mathrm{mm/s}$. The signal oscillations are used to determine the beat frequencies of the higher order modes. As we scan along the axis of the fiber, the signal increases as more light propagates as an evanescent field.

a technique known as the Gabor transform[Gabor, 1947], defined as

$$G(x) = \int_{-\infty}^{\infty} T(x')e^{-\pi(x'-x)^2/\zeta^2}e^{-i\beta x'}dx', \tag{5.2}$$

where $T(x')$ is the transmission signal, x and ζ are the position and width of the window and β is the spatial beat frequency. The Gabor transform of the probe signal is plotted in figure 5.8. We see distinct modes, which increase in beat frequency as the fiber diameter shrinks.

The fiber diameter is then determined by estimating the point where the spatial beat frequencies intersect the theoretical.

While this method is "non-destructive" it does, however, risk transferring dust to the surface of the nanofiber. We can therefore not make a waist measurement of the final fiber since this must be completely dust-free. Over the course of several months we measured the waist of pulled fibers and found that we could consistently get fibers with diameters of $\sim 490\,\mathrm{nm}$.

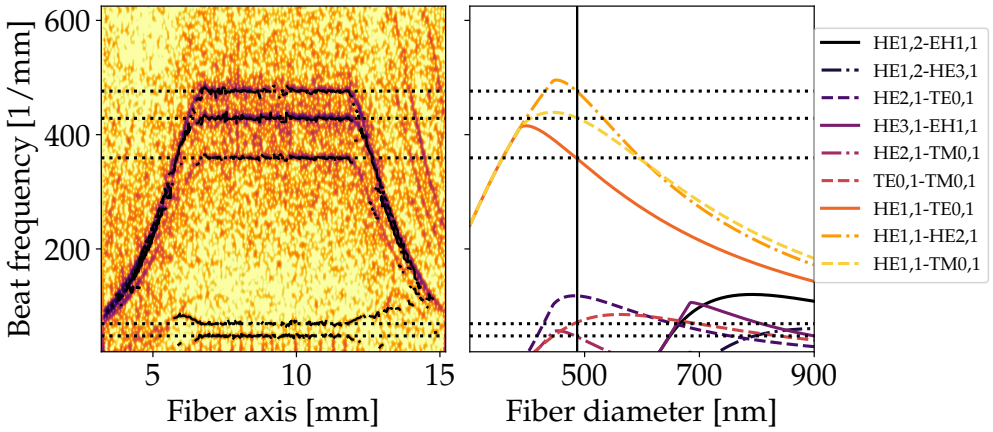

Figure 5.8 — Gabor transform of the probe fiber signal. Left panel shows the Gabor plot dashed lines represent the spatial beat frequencies of the nano section. Right panel shows beat frequencies between different guided modes for different fiber diameters. Vertical line shows the estimated diameter of the nanofiber, ~ 490 nm.

5.2 Fiber installation

The process of installing the nanofiber involves mounting the nanofiber to a holder for the vacuum, pumping and baking the vacuum chamber and splicing connectorized fiber ends to the nanofiber.

Due to slight differences in the mounting of the fiber, the alignment of the nanofiber with respect to the center of the MOT ended up being slightly off. Therefore realignment of the MOT was necessary. This will also be covered briefly.

5.2.1 Fiber gluing

The nanofiber is glued onto a glass holder using UV glue, glue points shown in figure 5.9. The glass holder is pressure fit onto a steel rod which is attached to a CF-flange[5] for the vacuum chamber. The CF-flange has threaded feedthrough holes which allows for a fiber to be coupled into the vacuum can. The fiber ends are passed through a Teflon ferrule which is compressed by a Swagelok nut,[Abraham and Cornell, 1998]. To avoid twisting the fiber ends a washer is placed in between the ferrule and the Swagelok, figure 5.10.

[5]ConFlat

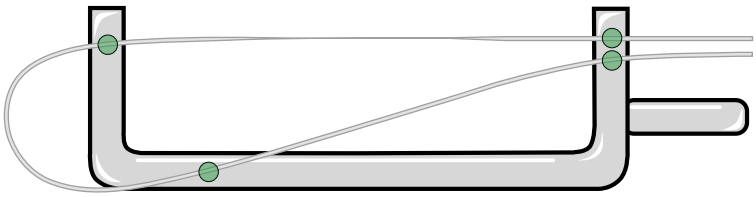

Figure 5.9 — The glue points on the nanofiber holder. The green spots indicate the glue points used to attach the nanofiber to the holder.

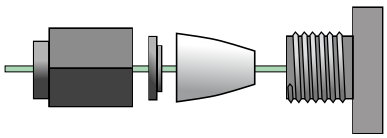

Figure 5.10 — Fiber feedthrough using a Teflon ferrule and Swagelok nut.

5.2.2 Pumping and baking

In order to efficiently trap atoms we require an ultra high vacuum, roughly 10^{-9} mbar. The vacuum is established in three steps while being monitored using an ion vacuum gauge[6], plotted in figure 5.11. The first step is using a turbo pump to bring the pressure down to $\sim 7 \times 10^{-8}$ mbar. During this initial pump down we send high powers of light(>20 mW) through the fiber, to make sure that it can withstand a reasonable amount of power. While pumping down we monitor potential leaks. One of the main sources of leaks is the fiber feedthrough. The Swagelok nut is gradually tightened to reduce leaks. It is, however, important to take care not to overtighten the Swagelok as this may affect the fiber shape and transmission and can in the extreme case damage the fiber. The vacuum chamber is then wrapped in heater wire, which allows us to gradually increase the temperature of the vacuum chamber. Since the chamber has been exposed to air, the inner surfaces will have accumulated water vapor, which we can evaporate off. We heat the vacuum chamber to roughly 100° Celsius. This temperature is chosen such that we do not compromise the UV-glue used to mount the nanofiber. After baking, the pressure is close to 10^{-8} mbar. The Cesium dispensers are flashed by supplying them with roughly 4 A of current to release any water or other grime, which might have accumulated while exposed to air.

Finally our ion pump is turned on to bring the pressure down to $\sim 10^{-9}$ mbar. The nanofiber ends are then spliced onto connectorized fibers, using a fusion splicer. We get estimated splicing transmissions of $> 99\%$ and $> 95\%$ for the two fiber ends. The vacuum chamber is

[6] AML: PGC2 UHV Vacuum gauge

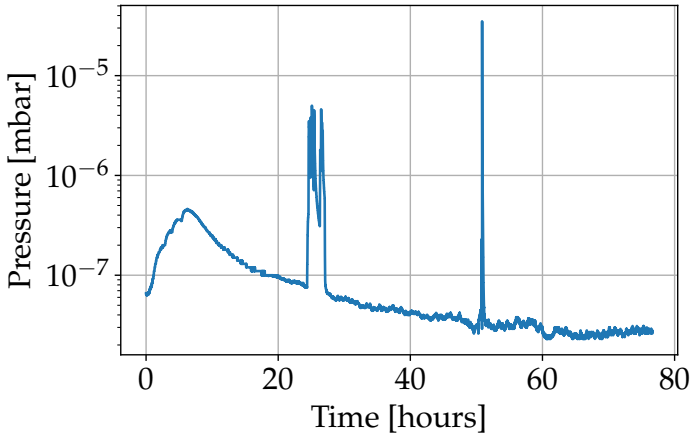

Figure 5.11 — Pressure in the vacuum chamber during baking. The initial increase in pressure is due to the increasing temperature. At roughly 25 hours the Cesium dispensers are flashed on, briefly increasing the pressure substantially. The final spike occurs when the ion pump is turned on.

then transported into the optical setup, where the ion pump continues to run.

5.2.3 MOT alignment

In order to load the nanofiber trap we first need to gather atoms. This is done using a magneto-optical trap. When installing the nanofiber into the optical setup it is necessary to ensure that the position of the nano-section of the fiber sits at the center of the MOT. The process of aligning the MOT is iterative and somewhat time consuming. Each of the six MOT beams have two angular degrees of freedom and can be translated in all direction. Three sets of compensation coils allow for cancellation of the Earths magnetic field as well as finetuning of the field zero of the MOT coils. The initial optimization of the MOT is done by looking at infrared cameras pointing at the fiber, sitting orthogonally to each other, images are shown in figure 5.12. During the loading of the nanofiber trap, the detuning of the cooler is increased and the magnetic field strength is ramped down. This means, that the equilibrium position of the MOT will be subject to change, if the MOT beams and magnetic center are not nicely aligned. We can adjust the field zero of the magnetic field by moving the MOT coils or using the compensation

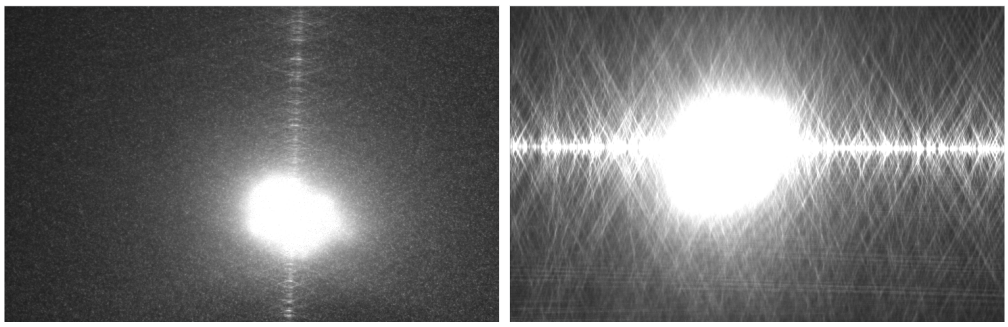

Figure 5.12 — Images of the MOT overlapped with the nanofiber.

coils to fine tune the position. The MOT is aligned, such that it remains stationary over the course of a sub-doppler cooling procedure.

Once the first atomic signal is acquired, we optimize the MOT w.r.t. the detected signal through the nanofiber.

CHAPTER

6 EXPERIMENTAL SETUP AND PROCEDURES

In this chapter a description of the experimental setup will be presented. Our dispersive probing scheme along with the practical implementation will be presented. The different methods for coherent manipulation of atomic states will also be presented with emphasis on a dipole force-free Raman scheme. Finally, a typical experimental sequence will be outlined.

6.1 Probing scheme

The small effective mode area of the evanescent field of the nanofiber guided light allows us to operate within the strong coupling regime [Balykin et al., 2004; Warken et al., 2007; Solano et al., 2017], with an optical depth (OD) of about $2.4\,\%$ per atom, [Béguin, 2015]. The strong coupling opens up the opportunity to work with a dispersive probing scheme.

The probing scheme, implemented by J.-B. Béguin, [Béguin et al., 2014], makes use of two symmetrical sidebands propagating through the atomic ensemble. The carrier is locked close to the $|F = 4\rangle \rightarrow |F' = 5\rangle$ transition, with the sidebands placed at $\pm 62.5\,\mathrm{MHz}$, corresponding to roughly 12Γ[1]. The carrier acts as a local oscillator(LO), with the two sidebands propagating through the nanofiber, interacting with the atoms. The absorption and dispersion around an atomic transition is plotted in

[1] Natural linewidths for the D2 line

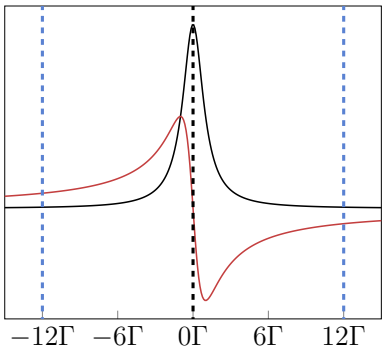

Figure 6.1 — Absorption and dispersion. Dashed lines are the lower sideband, carrier and upper sideband.

figure 6.1. We see that the sign of the refractive index changes on either side of the transition. This means that the two sidebands acquire phase shifts from the atoms of equal magnitude but opposite sign.

The sidebands are overlapped with the LO on a photodetector. The resulting beatnote can then be filtered, amplified and IQ-demodulated, yielding signals where the in-phase and quadrature components are proportional to

$$\begin{aligned} S^{\text{in}}(t) &\propto \mathcal{E}_{\text{LO}} \left\{ \bar{\mathcal{E}} \cos(\Phi_{\text{ref}}) \cos\left(\Delta\bar{\Phi}\right) + \Delta\bar{\mathcal{E}} \sin(\Phi_{\text{ref}}) \sin\left(\Delta\bar{\Phi}\right) \right\} \\ S^{\text{q}}(t) &\propto \mathcal{E}_{\text{LO}} \left\{ \bar{\mathcal{E}} \cos(\Phi_{\text{ref}}) \sin\left(\Delta\bar{\Phi}\right) - \Delta\bar{\mathcal{E}} \sin(\Phi_{\text{ref}}) \cos\left(\Delta\bar{\Phi}\right) \right\} \end{aligned} \tag{6.1}$$

$$\begin{aligned} \bar{\Phi} &= \frac{\Phi_1 + \Phi_2}{2}, \ \Delta\bar{\Phi} = \frac{\Phi_2 - \Phi_1}{2} \\ \bar{\mathcal{E}} &= \frac{\mathcal{E}_1 + \mathcal{E}_2}{2}, \ \Delta\bar{\mathcal{E}} = \frac{\mathcal{E}_2 - \mathcal{E}_1}{2} \\ \Phi_{\text{ref}} &= \Phi_{\text{LO}} - \bar{\Phi} \end{aligned} \tag{6.2}$$

where $\mathcal{E}_{1,2}$ and $\Phi_{1,2}$ are the field amplitude and phase shifts of the two sidebands. By balancing the two sidebands, i.e. minimizing $\Delta\bar{\mathcal{E}}$, we only get the second term of the two equations in 6.1. By choosing an appropriate LO phase, Φ_{LO}, we can maximize the in-phase signal in the absence of atoms. We note that for small $\Delta\bar{\Phi}$ the in-phase signal $S^{\text{in}}(t)$, is, to first order, only sensitive to changes in $\bar{\mathcal{E}}$. The other quadrature $S^{\text{q}}(t)$, on the other hand, is maximally sensitive to changes in $\Delta\bar{\Phi}$. The asymmetry of the atomic phase shift means that the differential phase, $\Delta\bar{\Phi}$, is sensitive to atomic phase shifts, while suppressing common mode phase shifts, such as elongation of the fiber. We can then extract the atomic phase shift, $\Delta\bar{\Phi}$, by the following,

$$\Delta\bar{\Phi} = \tan^{-1}\left(\frac{S^{\text{q}}(t)}{S^{\text{in}}(t)}\right). \tag{6.3}$$

The quantity $\Delta\bar{\Phi}$ is what is used to quantify the atomic population in the experiments presented.

6.1.1 Practical implementation

A schematic of the practical implementation of the two color probe is shown in figure 6.2. The probe sidebands are derived from an extended cavity diode laser(ECDL) locked close to the $|F = 4\rangle \rightarrow |F = 5'\rangle$ transition. The light is split into the LO and sidebands using a polarizing

beam splitter(PBS). The transmitted light is double-passed through an acousto-optic modulator(AOM), with a modulation frequency of 62.5 MHz. The 1st and -1st diffraction orders of the AOM are picked off and co-propagated into the nanofiber.

Figure 6.3 shows the method for generating the sidebands; the incoming light is shifted by the AOM and retro-reflected by a concave mirror, the 1st order is generated on the first pass and is unshifted beam second pass, the -1st order is obtained by taking the 0th order on the first pass and the -1st order on the second. The two co-propagating sidebands are coupled into the nanofiber.

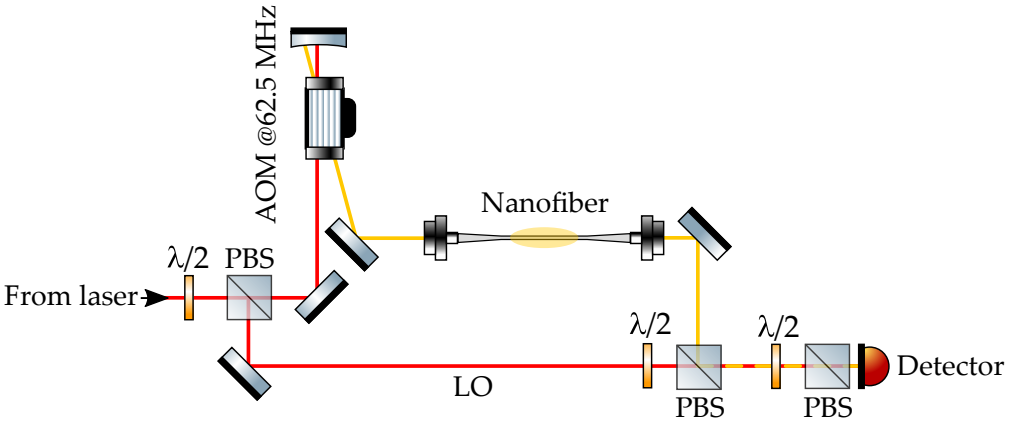

Figure 6.2 — Light derived from an ECDL is used to generate sidebands at 62.5 MHz using an AOM. The sidebands propagate through the atomic ensemble and are detected using heterodyne detection.

The unshifted light is used as a local oscillator. One mirror of the LO path has a piezoelectric crystal attached, allowing for stabilization of the interferometer arm. The LO path length is locked during MOT loading, when no atoms are present in the dipole trap, by maximizing the in-phase signal. Using a PBS and a waveplate the sidebands and LO can be overlapped and the power impinging on the detector adjusted using a second set of PBS and waveplate.

The probe polarization is parallel to the red trap laser. This means that the polarization of the probe at the trap minimum is elliptical. The probe will therefore optically pump the atoms into the outer m_F levels.

This effect is apparent in figure 6.4; the initial transient is a result of the increased interaction strength, due to larger Clebsch-Gordon coefficients, of the outermost m_F levels. The initial transient is followed by an exponential decay as a result of the heating of atoms in the trap.

Figure 6.3 — Generation of probe sidebands. The carrier light is passed through an AOM. The 1st and 0th order are retro-reflected picking up a 0 and -1 shift respectively. The (1,-1) co-propagate to the nanofiber.

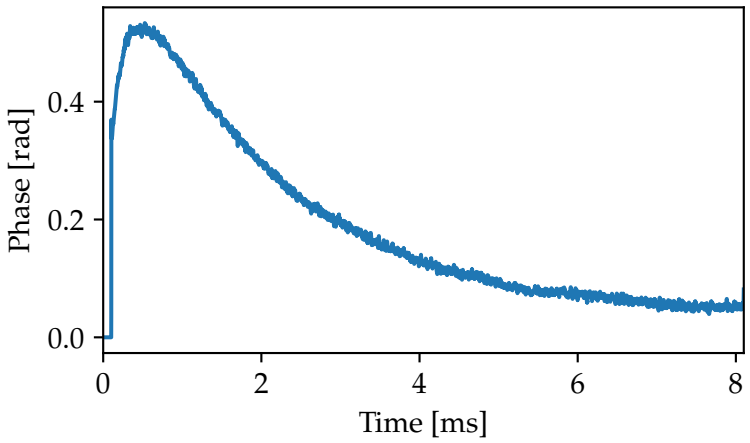

Figure 6.4 — A typical probing trace. The atoms are initially pumped into the extreme mf levels by the probe, this leads to an increase in signal due to larger Rabi frequencies. The signal subsequently decays due to heating of atoms.

6.2 Atomic transfer

Performing experiments on the trapped atoms requires coherent manipulation of the state of the atoms. We have two ways of doing coherent state transfers between the ground state hyperfine levels in our experiment; microwave pulses and stimulated Raman transitions.

6.2.1 Microwave

The microwave pulses are controlled using a DDS (Direct Digital Synthesizer) and allows for precision control of the microwave frequency. The microwave frequency is stabilized using a GPS reference to discipline a local crystal oscillator.

The microwave allows us to drive the hyperfine transitions directly, however, since these are electric dipole forbidden the transition must be driven using magnetic dipole transitions. These are inherently slower than their electric counterpart, which means that high microwave powers are necessary to achieve moderate Rabi frequencies. In our case the power of the microwave is on the order of 10 W leading to a Rabi frequency of ~ 40 kHz, shown in figure 6.5.

We have two microwave horns at our disposal in the experimental setup. One for linearly polarized pulses and one for circularly polarized

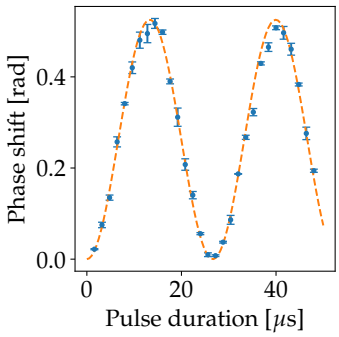

Figure 6.5 — Microwave Rabi oscillations. Rabi dashed line is a cosine fit yielding a Rabi frequency of $37.54(13)$ kHz.

pulses. Switching between the two microwave horns is cumbersome and cannot be done during experimental sequences. The addition of a relay would allow for fast switching between the two microwave horns.

The microwave wave-front is homogenous on the scale of the atoms. This makes it ideal for driving transitions on the entire atomic ensemble. The same homogeneity, however, also means that we cannot drive motional transitions in the trap.

6.2.2 Raman laser

Aside from the microwave horn we can also transfer atoms between the ground state hyperfine levels using Raman transitions. Raman transitions have the benefit of being two-step electrical dipole transitions and therefore allow for significantly larger Rabi frequencies at lower powers. Furthermore since the Raman light can be coupled through our nanofiber, the spatial inhomogeneity of the Raman light allows for coupling between motional states of the atoms, enabling the resolution of motional sidebands. However, the same spatial inhomogeneity also limits the transfer of atoms due to motional dephasing and for fast coherent transfer, more sophisticated pulsing schemes are required, [Østfeldt, 2017].

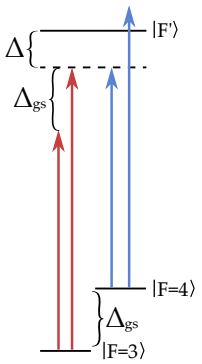

Figure 6.6 — A standard lambda system. The carrier is detuned by Δ forming a virtual level. For the lower ground state the two Raman fields are red detuned with respect to the excited level, whereas for the upper ground state the carrier is blue of the transition.

For a standard λ system, such as the one in figure 6.6, there is no way to choose the field amplitudes and/or detunings to allow for the same Stark shift of both ground state levels. The difference in Stark shift results in the level splitting changing. The Stark shift is dependent on the intensity and as such large intensity gradients will lead to inhomogeneous broadening of the transition. The nature of the nanofiber guided modes results in steep spatial intensity gradients and therefore strongly affect the atoms. Since we are ultimately interested in driving motional transitions and by that resolve the motional sidebands, we need to limit the effects of inhomogeneous broadening.

The differential Stark shift can, however, be cancelled by using a Raman scheme involving more than two fields.

6.2.2.1 Dipole force-free Raman scheme

The working principle of the dipole force-free Raman scheme is to have a carrier with two symmetrical sidebands, enabling the cancellation of differential light shifts, see figure 6.7. A detailed description of the scheme can be found in [Østfeldt et al., 2017]. The take-home points

are that such a Raman system allows for cancellation on the $|F = 0\rangle \rightarrow |F' = 0\rangle$ transition if the carrier detuning w.r.t the excited state manifold is approximately $\frac{\Delta_{\text{hf}}}{2}$, where Δ_{hf} is the hyperfine splitting of the ground state, and if the sideband to carrier power ratio is ~ 1.5. Using sepa-

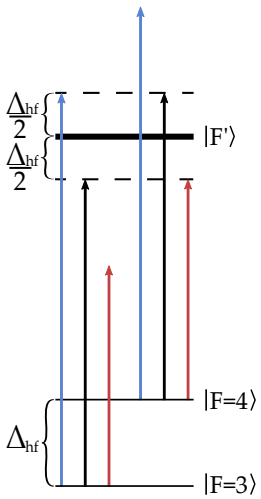

Figure 6.7 — Dipole force-free Raman scheme. Carrier, lower sideband and upper sideband separated by approximately the hyperfine splitting, Δ_{hf}. The carrier is detuned from the F' manifold by $\frac{\Delta_{\text{hf}}}{2}$.

rate lasers to implement this scheme would be cumbersome, which is why the sidebands are derived from the carrier. An Electro Optic Modulator(EOM) is used to generate the sidebands. The EOM modulates the phase of the light, generating sidebands at integer multiples of the modulation frequency, where the modulation strength determines the power in the sidebands. The practical implementation of the scheme

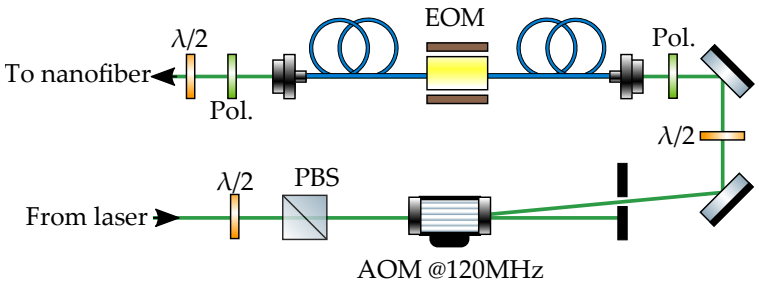

Figure 6.8 — Light derived from an ECDL is used to generate sidebands at 62.5 MHz using an AOM. The sidebands propagate through the atomic ensemble and are detected using heterodyne detection.

is depicted in figure 6.8. Light derived from an ECDL is sent through an AOM allowing for pulsing down to a $\sim 40\,\text{ns}$ timescale. The light is then propagated through a fiber-coupled EOM. The EOM is supplied with an RF pulse, where the frequency, amplitude and phase can be controlled on a 4 ns timescale using a DDS. The RF amplitude is typically measured in terms of DDS units, i.e. the units set within the computer controlled DDS board. A discussion on the practical cancellation of the differential Stark shift is presented in chapter 8.

6.3 A run of the experiment

There are several lasers involved in running the experiment; all of which are extended cavity diode lasers (ECDL). The repumper, cooler, probe, and Raman laser are locked using OPLLs[2], developed by [Appel et al., 2010]. The repumper acts as a master to which the other lasers are locked. The repumper is locked using saturated absorption spectroscopy on the transition from $F = 3$ to the 3×2 cross-over in the excited state manifold. The cooler, probe and Raman lasers are beatnote-locked to the repumper signal. We have three trap lasers, none of which are locked; one red detuned at 1064 nm and two blue detuned at 782.5 nm and 783 nm. The red trap laser is split into equal parts which are counter-propagating through the nanofiber, figure 6.9. The two blue trap lasers are propagating from either side, the counter propagation of the two slightly detuned beams cancels the local circular polarization at the trap minimum to limit the fictitious magnetic fields.

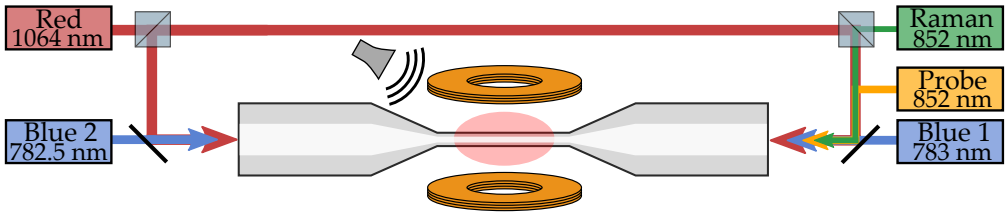

Figure 6.9 — The nanofiber trap is formed by propagating trap light through the fiber. Red trap light is counter propagated to form a standing wave. We counter propagate two blue lasers with slightly different frequencies to cancel fictitious magnetic fields.

[2]Optical phase locked loop

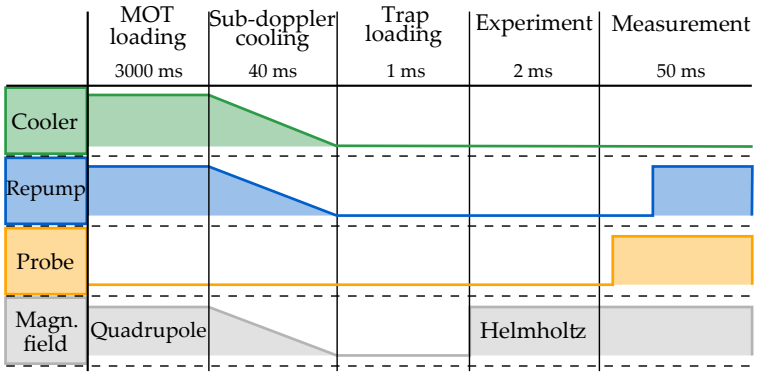

Figure 6.10 — A typical experimental sequence. The MOT is loaded and subsequently cooled using gray molasses. This is followed by loading into the nanofiber trap. The experimental sequences take place briefly before the detection in the measurement stage.

A typical experimental sequence is shown in figure 6.10. The Cesium atoms are initially loaded in a magneto-optical trap. This brings the atoms down to about the doppler temperature. This, however, is not quite cold enough to efficiently load the nanofiber trap. We use this opportunity to lock the detection interferometer, while no atoms are present in the trap. Next step is to further cool the atoms. To do this a subsequent sub-doppler cooling routine is employed. We use gray molasses, or blue Sisyphus cooling, to cool the atoms down to a theoretical temperature on the order of tens of the recoil temperature. The actual temperature reached during this sub-doppler stage is not of great importance since we mainly focus on optimizing the cooling with respect to dipole trap loading. The MOT loading takes approximately 3 seconds while the sub-doppler cooling step takes roughly 40 ms. During the sub-doppler cooling stage the quadrupole field for the MOT is gradually reduced.
The atoms are at this stage cold enough to be efficiently loaded into the nanofiber trap. After the loading we perform the desired state manipulation. The probe is turned on, typically along with the repumper to read out the atomic population after an experiment.

CHAPTER

7 NANOFIBER TRAP PARAMETERS

In this chapter, some of the characterization measurements carried out on the new fiber will be presented.

7.1 Trap heatmap

To optimize the trap we need to find the best trap power configuration. This is done by scanning the trap powers and measuring the resulting phase shift, seen in figure 7.1. We find the optimum to be roughly $4\,\mathrm{mW}$ per blue and $1\,\mathrm{mW}$ per red. The theoretical optimum configuration is $\sim 0.8\,\mathrm{mW}$ per red for a total blue power of $8\,\mathrm{mW}$. This puts us slightly above the expected amount of red trap power. This has been the case in all previous incarnations of the experiment [Béguin, 2015; Østfeldt, 2017; Hansen, 2018; Markussen, 2020]. The cause of this is not known, but might be due to bad contrast of the red standing wave - if the red trap polarizations are not nicely aligned the anti-nodes of the standing wave will be weaker. It is also possible that the blue trap polarization is not exactly orthogonal to the red trap polarization. This means that there will be more blue power at the trap sites and thus more red power is needed to balance the trap.

Increasing the overall trap power should, in principle, only lead to a deeper trap and thus more atoms, however, we find that the signal decreases when the power level crosses some threshold. We noted a significant amount of macroscopic vibration of the nanofiber when ex-

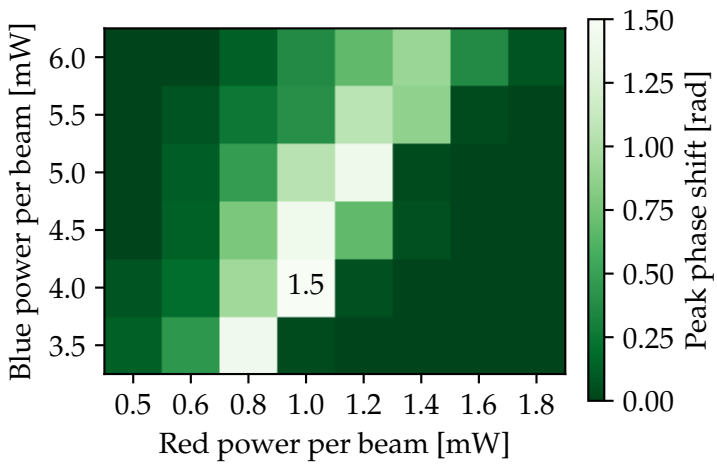

Figure 7.1 — Heatmap of maximum measured phase shift for different trap power combinations. Maximum value measured is annotated in the figure.

ceeding $\sim 5\,\mathrm{mW}$ per blue beam. This might be an explanation as to the decrease in signal.

There is a clear trend in the heatmap, leading to an optimum ratio of powers. This is expected since, if we consider the potential as described in chapter 4, we can write this as,

$$U = Be^{-x\kappa_b} - Re^{-x\kappa_r}, \tag{7.1}$$

where B is the power of the blue trap light, with decay constant κ_b, and R is the power of the red trap light, with decay constant κ_r. If we think of the optimum trap configuration we can think of the blue power as being $B = aR$, where a is a ratio. We can therefore factor out the red power,

$$U = R\left(ae^{x\kappa_b} - e^{-x\kappa_r}\right), \tag{7.2}$$

and we see that this simply scales linearly with power.

An interesting feature is the asymmetry around the maximum; an excess of red power leads to a steeper drop in signal. In this case the potential barrier towards the fiber surface is lower and thus trapped atoms are more likely to hit the fiber surface, heating them up and ejecting them from the trap. With an excess of blue trap light the potential barrier towards the fiber is taller, but the trap is also shallower.

7.2 Trap sloshing frequency

We now turn to the trap frequency. We can get an estimate of the radial trap frequency by pulsing off the red detuned trap light. This leaves the trap with only the repulsive part and thus gives the atoms a radial kick. The resulting sloshing of the center of mass of the atomic ensemble can then be measured to give an estimate of the radial trap frequency. The red trap is turned off for 100 to 600 ns. The resulting probe signal is modelled as a damped harmonic oscillation,

$$S(t) = Ae^{-t/T}\cos(2\pi ft + \phi) + k, \tag{7.3}$$

where A is the oscillation amplitude, T is the damping time, f is the trap frequency, ϕ is the phase and k is an amplitude offset. The data is fitted from $t = 200\,\mu$s, figure 7.2.

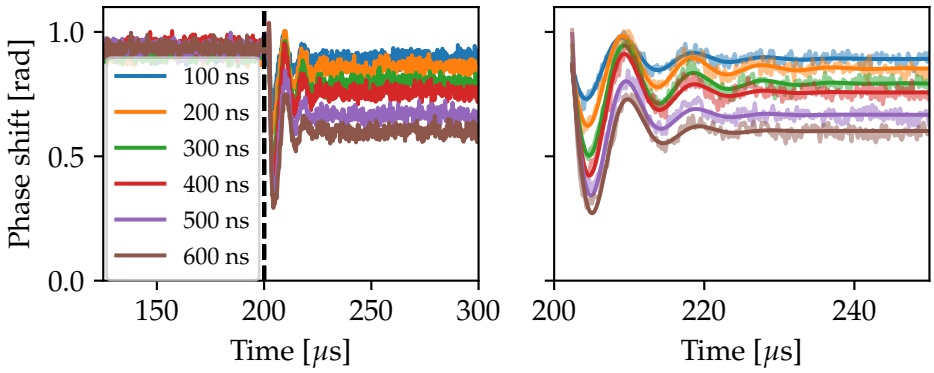

Figure 7.2 — Measurement of trap sloshing frequency. Left panel shows traces with the dashed line marking the pulse-off time at 200 μs. Data is averaged over 25 cycles. Right panel shows the fitted traces, shown with solid lines. Trap frequencies are plotted in figure 7.3

The overall dip in signal is due to loss of atoms during the pulse off, with longer pulse off times resulting in larger atom loss. We find a trap frequency of ~ 106 kHz, consistent with previous measurements [Markussen, 2017; Andersen, 2018; Hansen, 2018; Østfeldt, 2017]. The trap frequencies are plotted in figure 7.3. The trap configuration for this measurement was done with slightly more trap power than what is used in the rest of the thesis, with roughly 10 mW of total blue power and 1.25 mW per red.

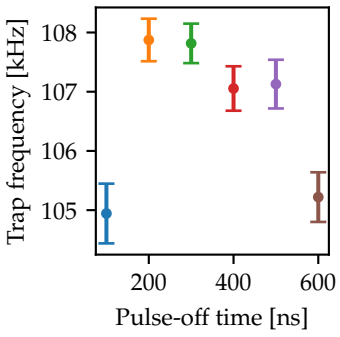

Figure 7.3 — Trap frequencies found in figure 7.2.

7.3 Trap lifetime

Finally we would like to characterize the lifetime of our trap. To do so the trap is loaded and after a variable delay the probe is turned on. The points used, are the maximum phase shift acquired during the probing intervals. The data is plotted in figure 7.4. The points are fitted with an exponential decay,

$$S(t) = Ae^{-t/T} + k, \tag{7.4}$$

where A is the initial phase shift, T is the lifetime and k is an amplitude offset.

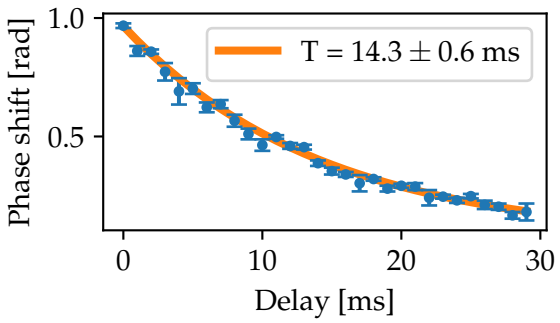

Figure 7.4 — Lifetime measurement of the trap. The probe is turned off after a variable delay after trap loading. The solid line is an exponential fit, yielding a lifetime in the trap of $T = 14.3\,\text{ms}$

The fit yields a decay time of $14.3\,\text{ms}$. This is quite a bit less than the $24.4\,\text{ms}$ observed in the our old nanofiber, [Østfeldt, 2017]. The reason for this has yet to be determined, but certain observations made in the experiment might point to an explanation. As mentioned in section 7.1 there is a significant amount of macroscopic vibration of the nanofiber, when exceeding a power level of 10mW of blue power. These vibrations might play a role, but given the fact that the vibrations are visible on the fiber cameras it seems unlikely that they are fast enough to play a role on an atomic scale.

What might also be contributing to the shorter lifetime is laser noise. We observed a significant amount of trap laser noise. This will be covered in the next section 7.4.

7.4 Noise

In the process of characterizing the nanofiber and optimizing the setup we also investigated the torsional modes of the fiber. This lead to the observation that two of the trap lasers were quite noisy. Only the measurement of the noise was carried out, but no mitigation of the noise was done.

7.4.1 Torsional modes

The vibrational modes of the fiber can have an impact on the trap lifetime, as heating of the atomic motion can lead to the expulsion of atoms from the trap, [Hümmer et al., 2019]. To measure the vibrational modes we place a polarizer at $45°$ w.r.t. the red trap polarization. The refractive index of the fiber is modulated by the vibrations and thus translate into a modulation of the polarization. This can then be measured on a photodetector. It is instructive to understand where the torsional modes of the fiber are since these vibrations may lead to heating if they are at the wrong frequency. The spectra shown in figure 7.5 exhibit a large

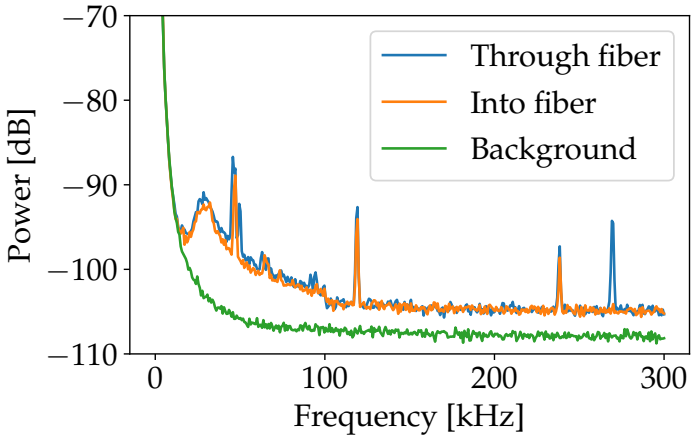

Figure 7.5 — Measurement of torsional modes of the nanofiber. The broadband noise of the laser obscures most of the torsional spectrum, with the exception of a peak at ~ 270 kHz and ~ 60 kHz.

amount of broadband noise at low frequencies. This was found to be due to amplitude noise of the red trap laser, which will be discussed in more detail in the next subsection.

We do not have a more complete spectrum of the torsional modes of the fiber, than what is shown in figure 7.5. This means that there could possibly be torsional modes at frequencies close to the trap frequency. We do however see peaks at $\sim$ 270 kHz and $\sim$ 60 kHz which coincides with the measurements taken on the old fiber, [Østfeldt, 2017]. In [Østfeldt, 2017] torsional modes were found at 66 kHz and 270 kHz, however there was no broadband laser noise as seen in figure 7.5.

7.4.2 Laser noise

We note that most of the broadband noise and peaks present in the torsional mode spectrum are in fact due to noise on the trap lasers themselves. The broadband noise in figure 7.5 was due to a poorly optimized AOM, which led to fluctuations in the coupling efficiency. We were able to reduce the amount of noise after the AOM. However, we found that there was still noise on the laser. We were able to trace down the noise to the current controller for the laser module. The amplitude noise is plotted in figure 7.6. We note that there is noise present on both the red

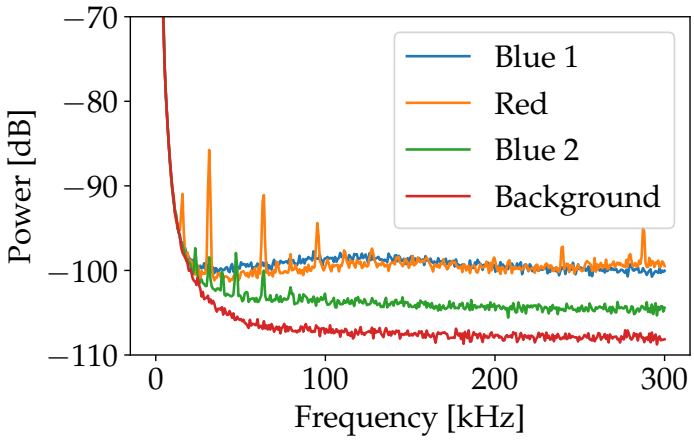

Figure 7.6 — Amplitude noise of the trap lasers.

trap laser and one of the blue trap lasers. The noise is also of a similar character. The noise shows up when the current controller modules have heated up. We concluded that the noise was simply due to degradation of the electronic components of the current controllers.

We were, however, not able to get rid of the noise on the lasers. We started investigating the noise on the lasers before we had our first

signal and were somewhat concerned that this was keeping us from trapping atoms. It turned out to not be the limiting factor and once atomic signal was acquired we abandoned the search for the source of the noise, but it remains a possible explanation for the low lifetime of the trap.

CHAPTER

8 STARK SHIFT CANCELLATION

In this chapter the efforts to balance differential Stark shifts, due to the Raman laser, will be presented. In chapter 6.2.2.1 a dipole force-free Raman scheme was presented. This scheme allows for cancellation of differential Stark shifts on the clock transition by proper choice of sideband to carrier ratio. As discussed in chapter 6.2.2.1 we can manipulate the sideband to carrier ratio using a DDS pulse, with a power given in DDS units. This is how we will refer to the modulation power throughout this discussion.

Our main tool for balancing differential Stark shifts is the Ramsey sequence, seen in figure 8.1. As shown in chapter 2, an atom in an equal superposition under the effects of a detuning, will begin to precess around the equator of the Bloch sphere. The states position on the equator affects the way the atom interacts with the light. Under the effects of a Stark shift the atom experiences a detuning from the hyperfine transition, causing the atom to precess around the equator of the Bloch sphere.

In practice this experiment is carried out by applying a resonant microwave $\pi/2$ pulse to establish an equal superposition, then, after a waiting time, applying a second $\pi/2$ pulse with variable phase to complete the transfer. During the waiting time a Raman pulse is applied. The Raman light drives the same transition as the microwave, which means that directly using the Raman light would affect the populations in the two hyperfine levels. What we would like is for the pulse to preserve the population while still affecting the level spacing. In prac-

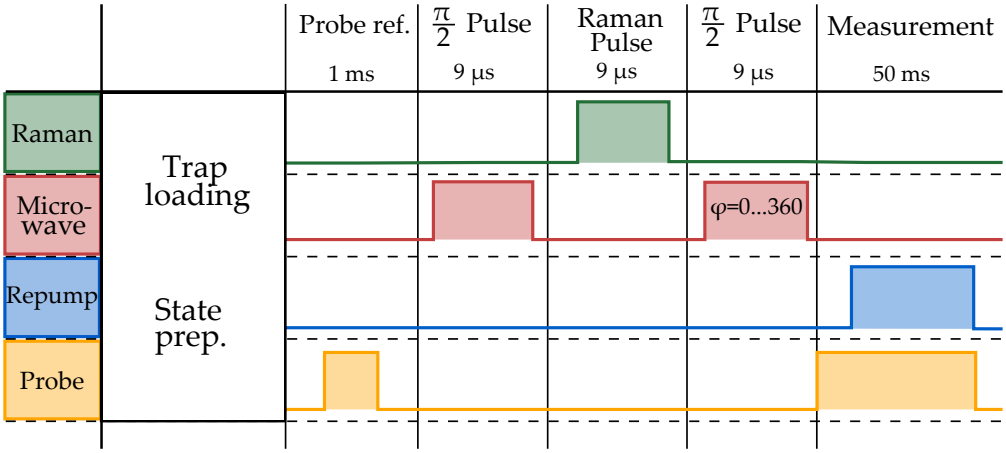

Figure 8.1 — Timeline of the Raman Ramsey sequence, employed to cancel differential Stark shifts. An initial microwave $\pi/2$ pulse is applied followed by a Raman pulse. The Raman pulse consisting of a series of 4 ns pulses with the phase flipping 180 degrees between subsequent pulses. A final $\pi/2$ pulse with variable phase is applied to finish the transfer of atoms. The population in $|F = 4\rangle$ is then read out by the probe. A repump pulse allows us to normalize the signal if necessary.

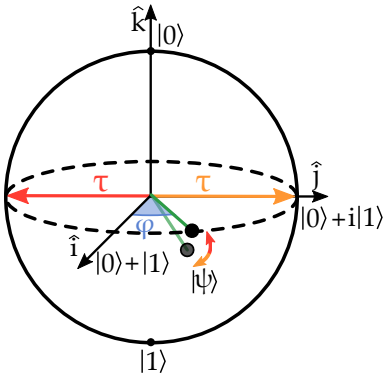

Figure 8.2 — Bloch sphere representation of the phase flip Ramsey sequence. The atoms are brought into an equal superposition using a microwave. A subsequent Raman pulse is applied, where the phase is toggled between 0° and 180°.

tice this is achieved by applying a short Raman pulse, where the phase of the pulse is modulated between 0° and 180° every 4 ns, see figure 8.2. This means that each subsequent 4 ns interval effectively undoes the work of the previous and the population in the two levels stays the same.

8.1 On the $|m_F = 0\rangle \rightarrow |m_F = 0\rangle$ transition

To cancel the differential Stark shift on the $|m_F = 0\rangle \rightarrow |m_F = 0\rangle$ transition we first have to prepare the atoms in the $|F = 3, m_f = 0\rangle$ state. This is done using the state preparation procedure presented in section 2.4. After the loading and state preparation, the atoms are put through a Ramsey sequence, as shown in figure 8.1. Since we are driving the $|m_F = 0\rangle \rightarrow |m_F = 0\rangle$ transition we use π polarized microwave pulses. The resulting fringe is then fitted to the function,

$$S(\phi) = A\cos(\phi + \phi_0) + k, \tag{8.1}$$

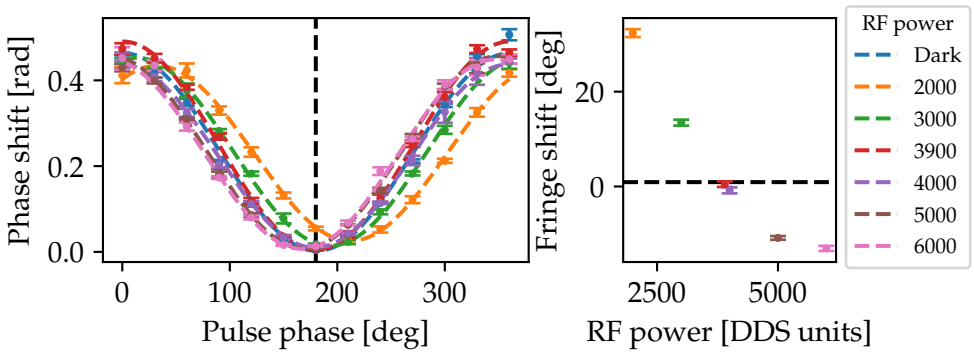

Figure 8.3 — Raman Ramsey fringe on the $|F = 0\rangle \rightarrow |F' = 0\rangle$ transition with different modulation indices. Left panel shows the phase shift, dashed line indicates $180°$. Right panel shows fringe shifts as a function of RF power, dashed line indicates dark fringe shift. Note that the fringe shift passes through zero, allowing for cancellation of differential Stark shifts.

where ϕ is the phase of the second microwave pulse, ϕ_0 is the fringe shift, A is the amplitude and k is an offset. In the case of an unbalanced Stark shift the fit will yield a non-zero ϕ_0.
Shown in figure 8.3(left) is an example of Ramsey fringes on the $|m_F = 0\rangle \rightarrow |m_F = 0\rangle$ transition. The fringes acquired in figure 8.3 are nicely resolved, with visibilities close to 1. The fringe shifts are plotted in the right panel of figure 8.3. We see that we can choose an RF power such that the differential Stark shift is cancelled.

8.2 Stretched Levels

Since we are ultimately interested in measuring Raman cooled spectra, which occur on the extreme m_F levels, we also have to make sure that the Raman scheme works on the stretched transitions. The naïve assumption that balancing the Stark shifts on the $|0\rangle \rightarrow |0\rangle$ transition would also balance them on the stretched transition is unfortunately wrong. Calculations on the differential Stark shift cancellation, with all excited states included, are shown in appendix B.1. The consequence of this is that we have to calibrate the Stark shift for each relevant transition. While doing this we discovered a possible serious systematic flaw in the phase toggling method. This means that experimentally we have to determine the appropriate RF power spectroscopically. More on this later in the section.

The initial idea was to use the same methodology as on the $|m_F = 0\rangle \rightarrow |m_F = 0\rangle$ transition, i.e. using a Ramsey sequence with a non destructive Raman pulse, but using σ polarized microwave pulses instead of π. In figure 8.4 a series of Ramsey fringes are plotted. These are nicely resolved and it would seem that with a proper choice of RF power, one could cancel the differential light shifts. In the case of figure 8.4 the choice of RF power was 4700. But as it turns out this does not work.

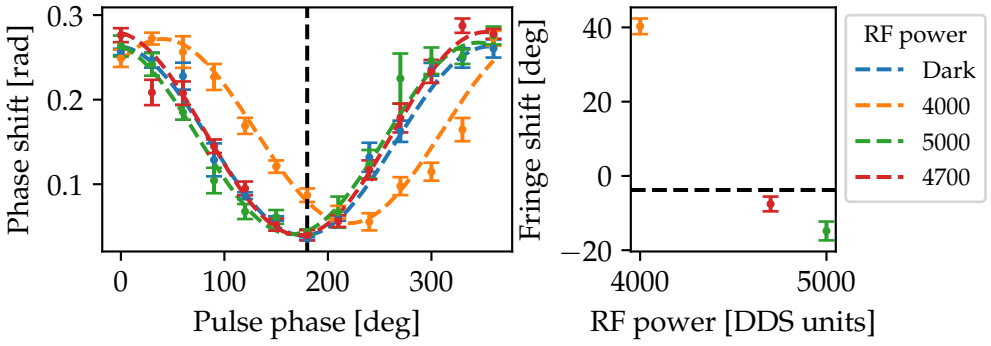

Figure 8.4 — Raman Ramsey fringe on the $|F = 3, m_F = -3\rangle \rightarrow |F' = 4, m_{F'} = -4\rangle$ transition. Good modulation RF power is 4700. Similarly to the 00 case we can choose an RF power such that the fringe shift is zero. This however turns out to not be sufficient, see figure 8.6.

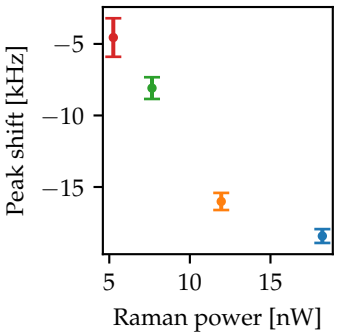

Figure 8.5 — Shifts of the Raman spectra w.r.t. the microwave spectrum for different Raman powers.

Shown in figure 8.6 are a series of Raman spectra using the "good" modulation index on the stretched transition, compared to a microwave spectrum. It is apparent that the spectra are significantly shifted from the microwave peak. Moreover the shift is dependent on the Raman power. This is highly suggestive that there is in fact an unbalanced Stark shift. Plotted in figure 8.5 are the shifts with respect to the microwave.

The Ramsey sequence using the phase-toggled Raman pulse does not work as expected on the stretched transition. Upon further inspection it is a stroke of luck that the method even works on the $|0\rangle \rightarrow |0\rangle$ transition. If we think of the phase flips, occurring every 4 ns, this really amounts to flipping the phase of the modulation tone sent to the EOM, generating the Raman sidebands. We can write the complex electric field as

$$E = E_0 \exp\left[i\left(\omega_{\text{opt}} t + z \sin\left(\Delta t + \Phi\left(\frac{t}{T_{\text{flip}}}\right)\right)\right)\right], \tag{8.2}$$

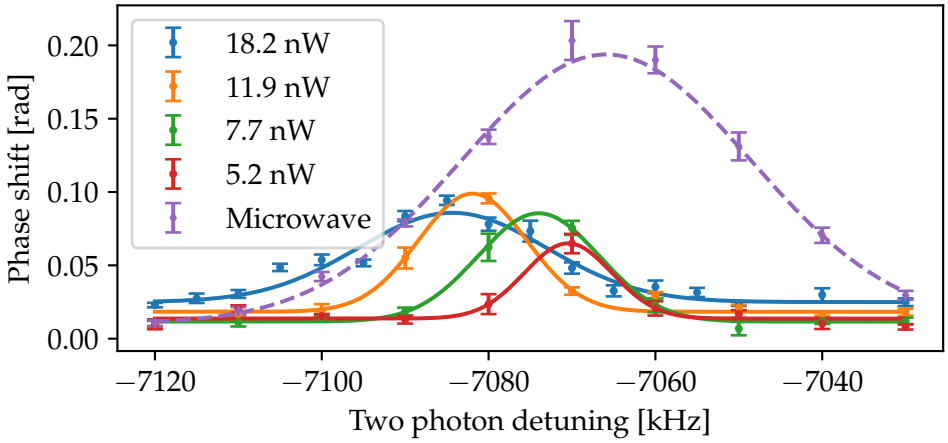

Figure 8.6 — Microwave spectroscopy and Raman spectroscopy on the stretched transition for different powers with the "good" modulation index of 4700. Note the change in the Raman spectra for different powers. Lines are gaussian fits.

where ω_{opt} is the carrier frequency, z is the modulation index, Δ is the sideband frequency and $\Phi\left(\frac{t}{T_{\text{flip}}}\right)$ is a rectangular wave with period T_{flip}. The spectrum of this field is plotted, along with the signal without the phase flips, in figure 8.7.

We see that a whole forest of peaks appears and that these have a significant amplitude, even far from the original sidebands. Seeing as the carrier is detuned by $\sim 4.5\,\text{GHz}$ w.r.t the excited state manifold, any component close to $4.5\,\text{GHz}$ will be close to resonance and result in strong Stark shifts. It seems, as of writing, that the fact that the Raman-Ramsey method with phase toggles works on the $|0\rangle \rightarrow |0\rangle$ transition is a coincidence and that a slight change to the carrier detuning could throw it off entirely.

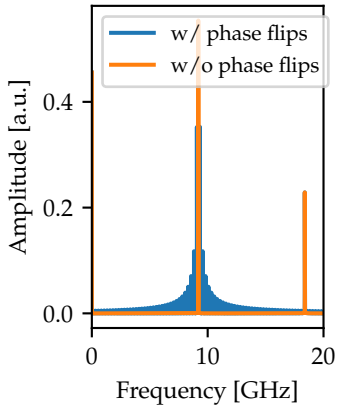

Figure 8.7 — Spectrum of the Raman light with and without phase toggling. Carrier and the two first sidebands are shown.

In the end we opted for a less elegant, and less sensitive, method. We first take a microwave spectrum as a reference. Then Raman spectra are taken for different powers. If there is a power dependent shift of the Raman spectra w.r.t the microwave spectrum, then we know that there is an unbalanced Stark shift. The Raman modulation index is then adjusted such that the shift is independent of the optical power.

Compared to the Ramsey method there are a number of downsides to this approach. The spectrum requires many data points to properly

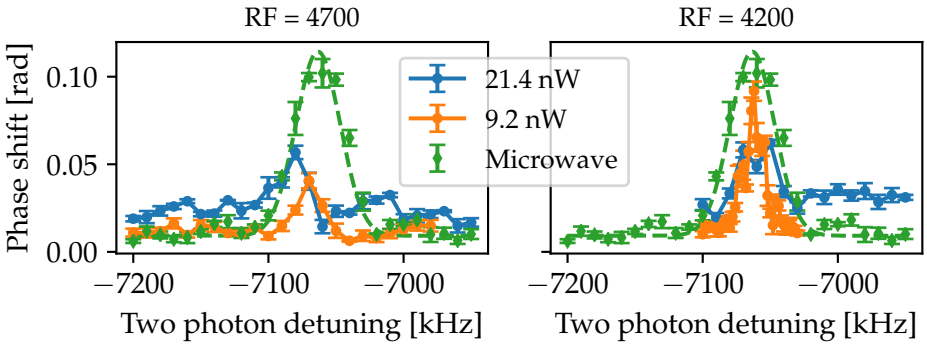

Figure 8.8 — Example of Stark shift cancellation on the stretched transition. The cancellation occurs with an RF power of 4200 DDS units. Note the change in lineshape between the two figures.

establish the line position. Due to the effects of Stark shifts the line shape and peak signal also depend on the modulation index, making it challenging to properly resolve the transition. Additionally it is cumbersome to fit the data and in practice we simply eye-ball the appropriate modulation index. The Ramsey method has, in contrast, a very simple expression to fit to the data and it is also not necessary to take many data points to properly resolve a Ramsey fringe. The Ramsey method also allows for very high sensitivity.

As seen in figure 8.8, the effects of unbalanced Stark shifts on the line shape are quite dramatic. It is therefore paramount that the effects can be minimized to improve the resolution of motional sidebands. A better method for cancelling the differential Stark shifts would be a large improvement on the flexibility and precision of the experiment. One could possibly run a Raman Ramsey sequence, but with a Raman pulse which is detuned away from resonance instead of modulating the phase. Placing the two photon detuning at 500 kHz would lead to essentially no transfer while allowing the Raman light to affect the shift of the energy levels.

8.3 Trap Vector Light Shifts

On the subject of light shifts we also explored the effect of fictitious magnetic fields due to the red trap. By purposefully unbalancing the red trap powers we no longer nicely cancel the longitudinal elliptic po-

larization of the nanofiber mode. Circular polarizations give rise to fictitious magnetic fields. Given the fact that the helicity of the polarization flips on the two sides of the fiber, the atoms on one side will experience a different effective magnetic field than on the other. This effect can be directly measured by utilizing the longitudinal elliptic polarization of the probe. Recall that the probing scheme used for this experiment takes advantage of two symmetric probe sidebands to allow for cancellation Stark shifts induced by the probe.

The probe, being polarized parallel to the red trap, will have opposite helicity on the two sides of the fiber, figure 8.9. Given the fact that the probe acts on the D2 line, a probe pulse will lead to optical pumping. The two sides of the fiber will be pumped into opposite ends of the Zeeman sub-levels. This will result in the ensemble of atoms being split on the two sides. The split of the ensemble allows us to interrogate each side of the fiber separately and in turn measure the fictitious magnetic field. Given a bias magnetic field, the effective magnetic field on the two sides of the fiber will be,

$$\mathbf{B}_{\text{eff}} = \mathbf{B}_{\text{bias}} \pm \mathbf{B}_{\text{fict}}. \tag{8.3}$$

we can then measure the effect using microwave spectroscopy. Using an elliptically polarized microwave π-pulse we can drive the transitions between the hyperfine levels.

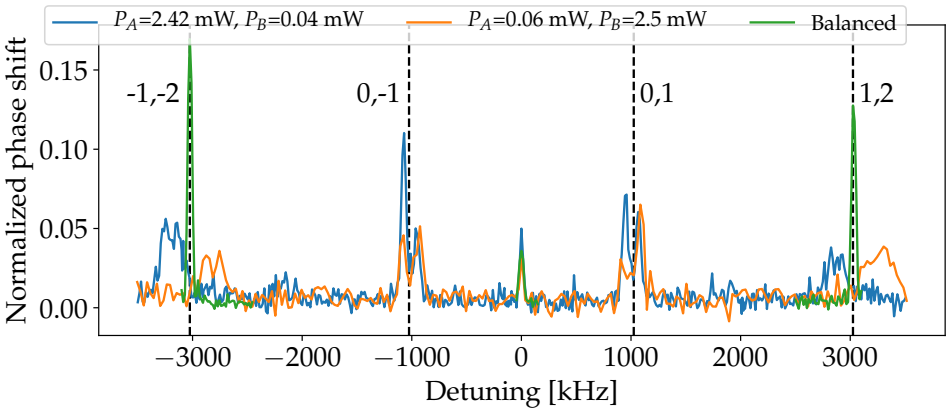

Figure 8.10 — Microwave spectrum with fictitious magnetic field induced by red trap light. The powers P_A and P_B refer to the trap powers through side A and B of the nanofiber, A being the propagation direction of the probe. The green trace is the balanced power case. Blue and orange are unbalanced with the majority of the power propagating from opposite directions.

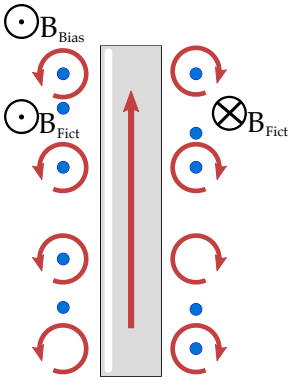

Figure 8.9 — Fictitious magnetic field generation around a nanofiber. Atoms are illustrated by the blue markers. The polarization of the red trap field is circular, with opposite helicity on either side of the fiber, fictitious magnetic fields are indicated with arrows pointing into and out of the page. The 3 Gauss bias magnetic field is indicated with an arrow pointing out of the page.

The spectrum is plotted in figure 8.10. The balanced situation is plotted as a reference. In the two unbalanced cases we flip the direction from which the majority of the power propagates. The imbalance used is roughly $2.5\,\text{mW}$ from one side and $5\,\mu\text{W}$ from the other. The $(1 \rightarrow 2)$ and $(-1 \rightarrow -2)$ transitions are shifted asymmetrically around $(0 \rightarrow 0)$. We also see that the transitions shift to the other side when the direction of propagation is reversed. From the $(0 \rightarrow 1)$ and $(0 \rightarrow -1)$ peaks we can estimate the magnitude of the fictitious magnetic field. The estimated fictitious magnetic field magnitude is (0.168 ± 0.002) Gauss and (0.18 ± 0.015) Gauss for the two cases.

CHAPTER

9 RESOLVED SIDEBAND SPECTROSCOPY

In this chapter the main experimental results of this thesis work will be presented. One of the main goals was to measure the temperature after degenerate Raman cooling, using the asymmetry of the motional sidebands. The progress on implementing the cooling scheme with subsequent Raman spectroscopy was halted by the existing fiber, Bertha, breaking. The effectiveness of the cooling scheme on the new fiber, Didrik, was not nearly as good, in terms of trap lifetimes, which potentially has a dramatic impact on the results. In order to accommodate the requirements for the cooling scheme and the spectroscopy a new magnetic field controller was made, see [Markussen, 2020] for details.

We will start this chapter off by presenting and discussing resolved sideband spectroscopy on the $(0 \rightarrow 0)$ transition. We will then move to the stretched transition, $(-3 \rightarrow -4)$, where the spectra with and without cooling will be presented. All of the data presented in this chapter have been normalized to the total number of trapped atoms.

9.1 Raman spectroscopy on $(0 \rightarrow 0)$

In previous work the focus has been on doing the sideband spectroscopy on the $(0 \rightarrow 0)$ transition, [Østfeldt, 2017; Hansen, 2018]. Given that we have a nice way of preparing the atoms into the $|F = 3, m_F = 0\rangle$ state, this is a good place to start to do sideband transfers.

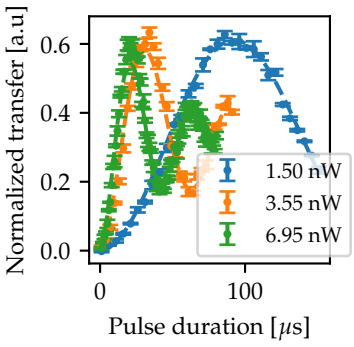

Figure 9.1 — Raman Rabi oscillations on the $|m_F = 0\rangle \rightarrow |m_{F'} = 0\rangle$ transition. The dashed lines are damped oscillator fits. The signal dephases rapidly for higher Raman pulse powers.

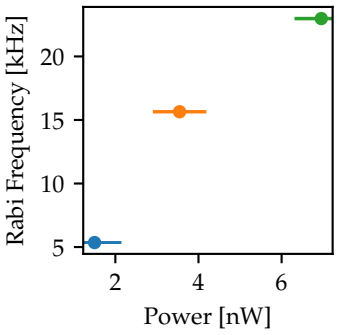

Figure 9.2 — Raman Rabi frequencies acquired from fits as a function of optical power.

The atoms are loaded into the nanofiber trap and are subsequently optically pumped into $|\mathrm{F} = 3, m_\mathrm{F} = 0\rangle$ using the state preparation scheme presented in section 2.4. A short probe measurement is carried out to establish a signal reference in the absence of atoms. A subsequent Raman pulse is then applied to bring the atoms from $|F = 3\rangle$ to $|F = 4\rangle$ where they can be detected by the probe.

In order to do efficient transfers we need to know the appropriate pulse duration. An example of Rabi oscillations using the Raman laser is shown in figure 9.1. The oscillations are fitted to a damped oscillation

$$S(t) = A\left(1 - \cos(2\pi\Omega t + \phi)\mathrm{e}^{-t/T}\right), \tag{9.1}$$

where A is the oscillation amplitude, Ω the Rabi frequency, ϕ a phase offset, T the decay time and S_{off} an offset. The Rabi frequencies acquired in the fits are plotted in figure 9.2.

The Rabi oscillations highlight an important property of the Raman transitions; the fast dephasing, which occurs due to the spatial inhomogeneity of the Raman light in addition to the thermal distribution of atomic motional states. This is the main technical limitation of using the Raman laser for fast coherent transfers of atoms. An in-depth discussion on a rapid adiabatic passage scheme to work around the inhomogeneous coupling can be found in [Østfeldt, 2017].

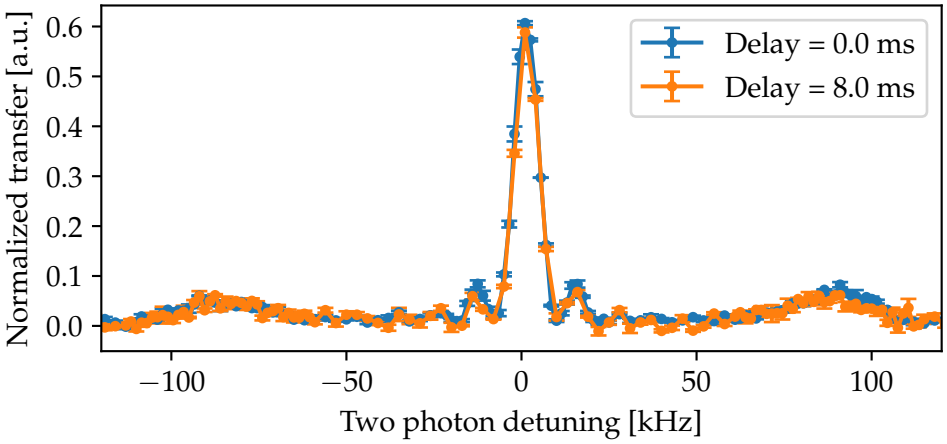

Figure 9.3 — Raman spectra on the $|m_\mathrm{F} = 0\rangle \rightarrow |m_{F'} = 0\rangle$ transition. The spectra are generated using a Raman pulse power of 1.5 nW with a pulse duration of 100 μs. The two spectra are taken with different delay after the population transfer. The transfer is normalized to the total number of atoms.

Figure 9.3 shows resolved Raman sideband spectra on the $(0 \to 0)$ transition. Two spectra are taken at different points in time; one right after the state preparation, the other after an 8 ms delay. Both of the spectra are normalized to the repumped signal to account for the difference in atom number. We can fit the carrier to a Rabi spectrum,

$$S(\Delta) = \frac{A}{1 + (\frac{\Delta - f_0}{\Omega})^2} \sin^2\left(\pi \sqrt{\Omega^2 + (\Delta - f_0)^2}\tau\right) \tag{9.2}$$

where Ω is the Rabi frequency, f_0 is the resonant frequency and τ is the pulse duration. The carrier fit is plotted in figure 9.4, giving us Rabi frequencies of ~ 5 kHz.

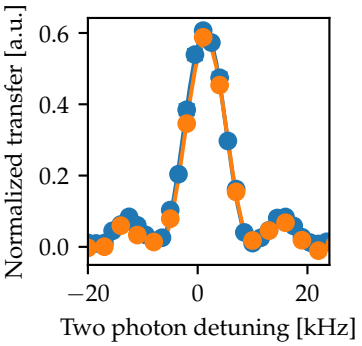

Figure 9.4 — Carrier transitions from the spectra in figure 9.3. The data is fitted with the function in eq. 9.2, yielding Rabi frequencies of 5.63(5) kHz and 4.88(8) kHz.

The motional sidebands are very clearly resolved, sitting at a frequency of roughly 90 kHz. The motional sidebands are plotted in figure 9.5. Here the asymmetry of the upper and lower sideband becomes very apparent. The asymmetry suggests that the atomic ensemble is quite cold. Moreover, we see that the lineshape of the sidebands is markedly asymmetric, owing to the anharmonicity of the trap potential. In order to estimate the temperature of the atoms, based on the spectra, we need to quantify the sideband ratio. We fit the sidebands to a heuristic model,

$$S_{\mathrm{SB}}(\Delta) = A \frac{e^{-(\Delta-\mu)^2/2\sigma^2}}{1 + e^{-\alpha(\Delta-\mu)}} \tag{9.3}$$

where A is the amplitude, μ the mean, σ the standard deviation and α is a skewness parameter.

Assuming a harmonic spectrum we can estimate the mean occupation number of the ensemble by calculating the ratio of the two sideband areas, I_{SB} [Leibfried et al., 2003]. The sideband ratio is defined as,

$$r_{\mathrm{SB}} = \frac{I_{\mathrm{lsb}}}{I_{\mathrm{usb}}} = \frac{\bar{n}}{\bar{n} + 1} \tag{9.4}$$

where $\bar{n}$ is the mean occupation number at temperature T, determined by the Bose-Einstein distribution,

$$\bar{n} = \frac{1}{e^{\frac{\hbar\omega_{\mathrm{SB}}}{k_{\mathrm{B}}T}} - 1} \tag{9.5}$$

where we define ω_{SB} as the mean frequency of the sidebands. From this we can find the temperature

$$T = -\frac{\hbar\omega_{\mathrm{SB}}}{k_{\mathrm{B}}} \frac{1}{\ln(r_{\mathrm{SB}})}. \tag{9.6}$$

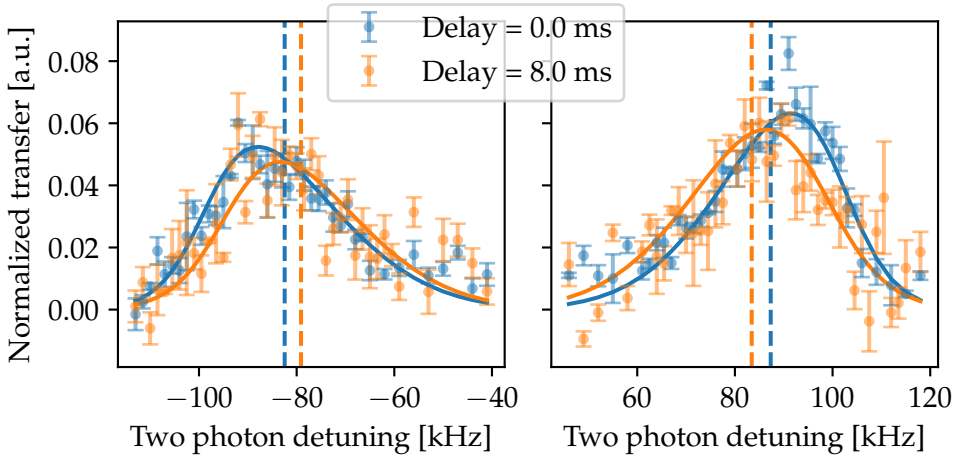

Figure 9.5 — The motional sidebands fitted to the function 9.3. The dashed lines indicate the mean frequency of the sidebands.

The integral of equation 9.3 is done numerically using a Monte-Carlo simulation, which also allows for estimation of the uncertainty. This is described in more detail in appendix C. This is also done to determine the mean frequency of the sidebands. The uncertainties quoted in this chapter only take into account statistical error and thus do not contain possible systematic errors in the estimates. We find temperatures of $\mathbf{30.1(18)}$ μK and $\mathbf{18.3(3)}$ μK for the spectrum without and with delay, respectively. This corresponds to sideband ratios of $0.87(3)$ and $0.80(6)$ with mean occupation numbers of $7(1.9)$ and $4(1.5)$. The fact that the delayed spectrum has a lower temperature is contrary to what we would have expected; as time passes, the atoms should be heated by noise sources in the trap and thus the spectrum taken after a delay should yield a larger temperature. Additionally, looking at the sideband shape and position, it would seem that the sidebands without delay skew towards higher frequencies than the delayed sidebands. Since the trap potential gets shallower for increasing energy, the lowest motional states have the largest trap frequencies and thus this would point to the temperature being lower. In chapter 11 we will see how this discrepancy might be related to the increased sensitivity of the temperature estimation for large sideband ratios.

9.2 Raman spectroscopy on the stretched levels

Having done Raman spectroscopy on the $|0\rangle \rightarrow |0\rangle$ transition we now turn to the stretched transition, $|-3\rangle \rightarrow |-4\rangle$. This is a somewhat more complicated procedure than the $|0\rangle \rightarrow |0\rangle$ transition. The pulse sequence is shown in figure 9.6.

After loading the dipole trap, the atoms are pumped out to the stretched levels using the probe along with the repumper. The atoms are then transferred to $|F = 3, m_F = -3\rangle$ via a microwave pulse, not pictured. The remaining atoms in the $|F = 4\rangle$ manifold are blown away using

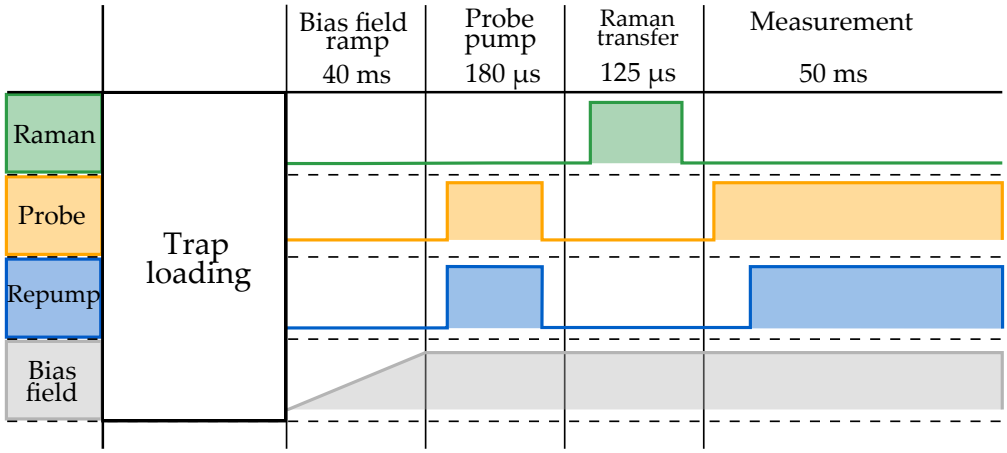

Figure 9.6 — After loading the trap the magnetic bias field is ramped up to 3 Gauss. The atoms are then pumped into $|F = 4, m_F = -4\rangle$ using the probe and repumper. A subsequent σ polarized microwave pulse brings the atoms into $|F = 3, m_F = -3\rangle$ followed by a MOT cooler pulse to blow away atoms remaining in $|F = 4\rangle$. A Raman transfer pulse is then applied followed by measurement with the probe. A repump pulse after a few ms allows for normalization of the spectra.

a pulse from the MOT cooler. The atoms can then be transferred to $|F = 4, -4\rangle$ using a Raman pulse. The probe is then turned on to measure the atoms, with the repumper turning on after a short delay to allow for normalization to the total number of atoms.

Figure 9.8 shows spectra on the stretched transition. The spectra are taken with a Raman power of 21.4 nW, a significant increase compared to the $(0 \rightarrow 0)$ transition (1.5 nW). This is due to the fact that in order to drive transitions where $\Delta m_F = \pm 1$ we need both a σ- and a π-polarized

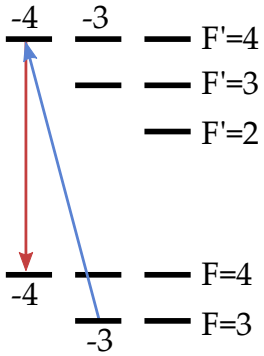

Figure 9.7 — Transfers between the two stretched hyperfine levels. In order to complete the transfer a σ^- polarized photon and a π polarized photon is necessary.

photon, figure 9.7. Our Raman light is almost exclusively σ^- polarized and we therefore need more power to achieve Rabi frequencies, comparable to those on $|0\rangle \rightarrow |0\rangle$. The power can be optimized by rotating the polarization of the Raman laser, to introduce more linearly polarized light, however this optimization was never carried out.

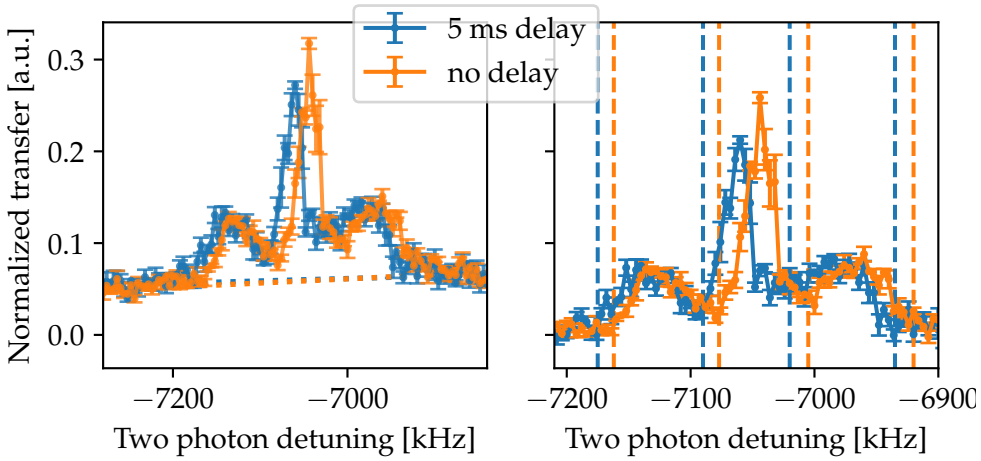

Figure 9.8 — Raman spectra on the stretched transition. The spectra are taken with different delays, leading to a shift due to the magnetic field value gradually changing. Pulse duration of $125\,\mu$s with a power of $21.7\,$nW.

The motional sidebands are resolved in figure 9.8, however, they are not as clearly resolved as on the $|0\rangle \rightarrow |0\rangle$ transition. Additionally the signal has a large offset, as shown in the left panel of figure 9.8. The offset is accounted for by calculating the mean signal of the ten first and last data points and then fitting a straight line (shown as dashed lines in the left panel) to those points. This line is then subtracted from the signal. The right panel shows the normalized phase shift with the offset subtracted. The vertical dashed lines denote the delimiters for the motional sidebands.

The motional sidebands, with fits, are plotted in figure 9.9. From these fits we can extract a temperature, in the same way as in section 9.1. The temperatures we find are $13.9(5)\,\mu$K for the delayed spectrum and $12.3(3)\,\mu$K for the other. This is lower than the temperatures found on the $(0 \rightarrow 0)$ transition, despite there being no cooling mechanism in use. The offset of the signal, figure 9.8(left), leads to some ambiguity in the temperature, as an offset in the signal will affect the ratio of the sidebands. The effect of a constant offset is to increase the temperature,

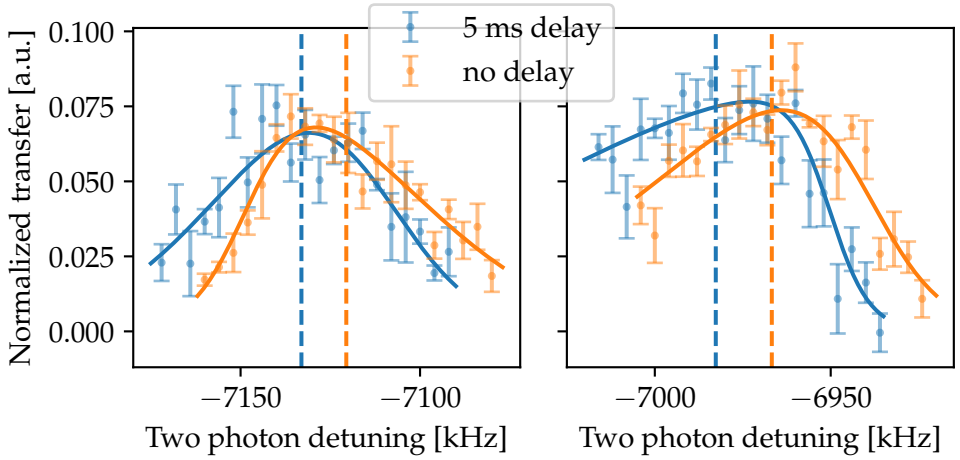

Figure 9.9 — Lower(left) and upper(right) motional sideband of spectra on the stretched transition taken at different times after optical pumping. Raman power of 21.7 nW with a pulse duration of 125 μs. The vertical lines mark the mean frequency of the sidebands.

as the difference in sideband amplitude becomes less pronounced. On the other hand a slope in the offset can lead to lower temperatures by lifting the upper sideband more than the lower. Table 9.1 contains tem-

	5 ms delay	no delay
Unmodified	19.5(8) μK	17.6(4) μK
Constant	11.7(5) μK	9.9(3) μK
Slope	13.9(5) μK	12.3(3) μK

Table 9.1 — Temperatures on the stretched transition with different methods for accounting for offsets.

peratures for the different methods of accounting for the signal offset. We see almost a factor of two between the lowest and highest temperature. This ambiguity highlights one of the major flaws in this method for temperature estimation; a signal offset has an impact on the resulting temperature. For this reason it is nice to be able to reduce the offset in the signal.

The source of the offsets seen in figure 9.8 seem to be a combination of a couple of factors. The fact that we drive the $(-3 \rightarrow -4)$ transition means that we are having to use a σ^- and a π polarized photon.

Since our polarization state is naturally dominated by sigma polarized light this means that the transfer will be quite inefficient. The neighboring transition, $(-3 \rightarrow -3)$, is much stronger however. This means that we are power broadening the neighboring transition quite considerably and thus this bleeds into the signal on the $(-3 \rightarrow -4)$ transition. We can estimate the Raman Rabi frequency of the $(-3 \rightarrow -3)$ transition , since we know the Rabi frequency of the $(0 \rightarrow 0)$ transition. For a power of 1.5 nW we get a Rabi frequency of roughly 5 kHz on the $(0 \rightarrow 0)$ transition. The $(-3 \rightarrow -3)$ transition is roughly 2/3 as strong, only accounting for sigma- transitions. This means that with a power of 21.7 nW we are effectively driving the $(-3 \rightarrow -3)$ transition with a Rabi frequency of 50 kHz. If we assume that the fast oscillations of the Rabi spectrum are averaged out we can write the contribution of the neighboring level as

$$S = \frac{\Omega^2}{\Omega^2 + \Delta^2} \frac{1}{2} \tag{9.7}$$

This means that at a detuning of 1 MHz we would expect a transfer of about 0.0012 which does not seem to account for the large offset in the signal. The Raman transitions rely on the validity of the adiabatic elimination of the excited state. As the intensity grows the transfer of atoms into the excited state manifold increases. This then leads to broadband noise. This, however, is also a small effect. Lastly there is the effect of magnetic field fluctuations. Since we are working on the stretched transition the sensitivity to magnetic fields is maximal. This of course means that fluctuations of the bias field will lead to broadband noise. The effects of the magnetic field will be discussed in more detail in the next section.

9.2.1 Degenerate Raman cooling

Finally we want to see if we can measure the effects of cooling using Raman spectroscopy. The cooling scheme employed in the following discussion was presented in chapter 2, however a brief recap will be given. By utilizing the fictitious magnetic field generated by the blue trap lasers we can couple adjacent degenerate Zeeman states. If the bias magnetic field is tuned correctly two adjacent Zeeman levels, with different motional states $|m_{\mathrm{F}}, n\rangle$ and $|m'_{\mathrm{F}}, n+1\rangle$, become degenerate, thereby allowing for the coupling via the fictitious magnetic field. By pumping the atoms using a σ^- polarized beam we can continually cycle the atoms into lower motional levels. All the motional states can

couple via the fictitious magnetic field to adjacent states except for the motional ground state, effectively making it a dark state. This leads to atoms accumulating in the lowest motional state, thereby cooling the ensemble, [Meng et al., 2018; Markussen, 2020].

Early on in the process of implementing the cooling scheme it became apparent that in order to do both cooling and Raman spectroscopy we needed to be able to switch the bias magnetic field fast, since the good bias field for cooling was not suitable for resolved sideband spectroscopy. In the past, the MOT compensation coils had provided the bias field, however they were found to be too slow. For this reason a magnetic field controller was developed. The details of this magnetic field controller can be found in [Markussen, 2020].

The optimum bias field for cooling was found to be roughly 0.51 Gauss, see appendix C. The σ^- polarized pump is supplied by the probe laser. As shown in chapter 3, the helicity of the evanescent field flips on the two sides of the fiber resulting in cooling of atomic motion on one side and heating on the other. The experimental timeline for the degen-

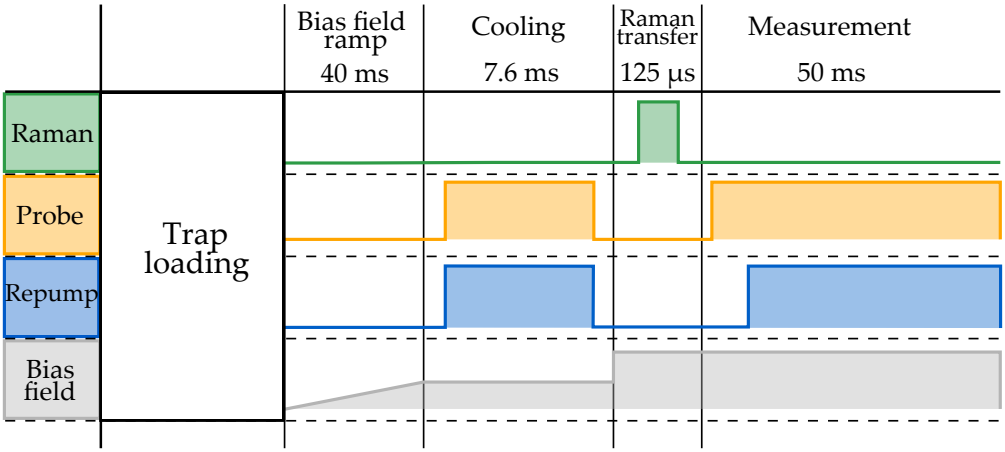

Figure 9.10 — Sequence for degenerate Raman cooling scheme with Raman sideband spectroscopy. The atoms are loaded into the nanofiber trap, the magnetic bias field is subsequently ramped to the cooling value of 0.51 Gauss. The probe and repumper are turned on for 7.6 ms to pump and cool the atoms. The magnetic field is subsequently increased to 3 Gauss to allow for resolved sideband spectroscopy. The Raman laser is pulsed and the population in $|F = 4, m_F = -4\rangle$ is read out by the probe.

erate Raman cooling followed by Raman spectroscopy is outlined in figure 9.10. After loading the trap the magnetic field is ramped up to the good cooling value of 0.51 Gauss. At this value a probe pulse is applied

for 7.6 ms. This pulse facilitates the cooling and pumps the atoms into the $|F = 4, m_F = -4\rangle$ level. After the probe pulse a microwave saving pulse brings the atoms into $|F = 3, m_F = -3\rangle$. This pulse is followed by a MOT cooler pulse which blows away any atoms remaining in $|F = 4\rangle$. The magnetic field is then ramped to 3 Gauss, allowing for better resolution of the motional sidebands. We then probe the ensemble, followed by a repump pulse to allow for normalization.

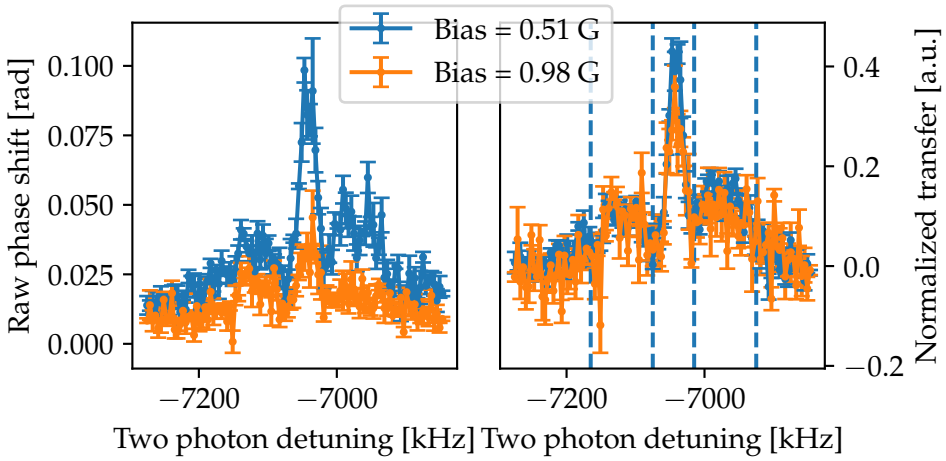

Figure 9.11 — Raman spectra taken after degenerate Raman cooling. Both spectra are taken with a $125\,\mu$s pulse duration and a power of $24.5\,$nW. The spectra are taken with two different bias magnetic fields; the good cooling field at $0.51\,$G and the suboptimal field at $0.98\,$G. Left panel shows the raw phase shift. Right panel shows the normalized phase shift with subtracted offset. The vertical lines in the right panel mark the delimiters for the motional sidebands.

Plotted in 9.11 are Raman spectra of atoms with the optimum bias value of 0.51 Gauss and with a sub-optimum value of 0.98 Gauss, for comparison. The left panel of figure 9.11 shows the raw spectra without normalization to the repumped signal. The right panel shows the normalized signal with a sloped offset subtracted. The first thing to note in the left panel is the drastic increase in signal from the bad bias field to the good. This shows that the cooling scheme has an effect on the lifetime in the trap and that a significant amount of atoms stick around after cooling. We can however also see that the line shape of the spectrum changes quite dramatically when we normalize to the repumped values. This tells us that there are significant variations in total number of atoms. The data is taken sequentially, i.e. the detuning is stepped

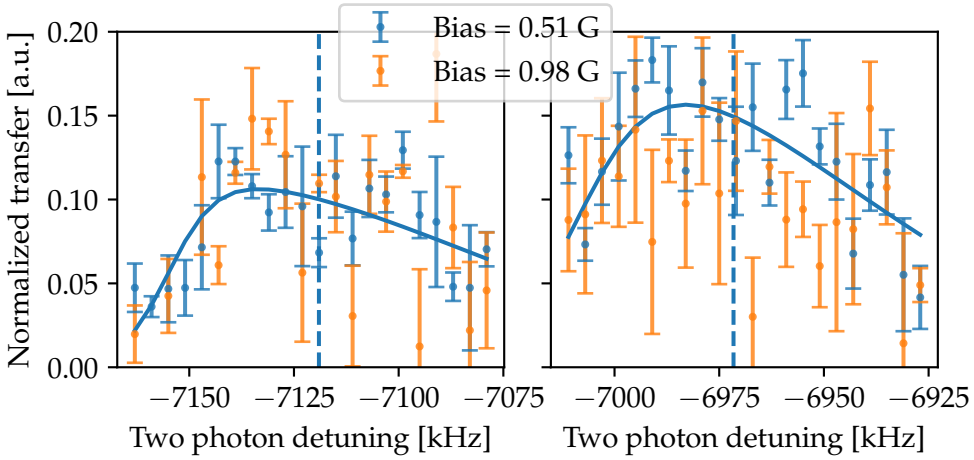

Figure 9.12 — Lower(left) and upper(right) motional sideband of Raman spectra, with and without degenerate Raman cooling. Only the cooled spectrum has an included fit. Vertical dashed lines mark the mean frequency of the sideband.

linearly, with four measurements per data point. If the variations in the loading was simply noisy, one would expect this to average out over time, however it seems that something is drifting quite dramatically. Drifts in the Raman transfer would manifest itself in the normalized spectra, however we see the same basic line shape in both cases. It would seem that the total number of atoms is drifting. This could be due to the actual loading of the nanofiber trap, however this seems unlikely. What seems more likely is that the magnetic field is somehow drifting over time. A drifting magnetic field would change the efficiency with which we can transfer atoms into $m_{\mathrm{F}} = -3$ after pumping, thereby lowering the number of atoms.

The motional sidebands from the spectra, figure 9.11, are plotted in figure 9.12, with fits using equation 9.3. The sideband asymmetry is quite clear in the cooled spectrum, whereas the uncooled spectrum has a much less pronounced asymmetry. Only the cooled sidebands are fitted, since the uncooled data is too noisy to allow for reasonable fits. Based on visual inspection it seems quite clear, that the cooled spectrum has a larger asymmetry than the uncooled spectrum and therefore also a lower temperature. As with the measurements of the uncooled stretched transition spectra there is a sizeable offset in the data, which, depending on the method, can be accounted for, leading to widely varying temperature estimates. Different temperature esti-

	With cooling
Unmodified	$20(1.8)\,\mu$K
Constant	$7.7(8)\,\mu$K
Slope	$10.6(7)\,\mu$K

Table 9.2 — Temperatures on the stretched transition with different methods for accounting for offsets.

mates for the cooled spectrum are given in table 9.2. These temperatures are lower than the ones found in table 9.1 for both the constant offset and the sloped offset. The temperatures also lie outside the error bars of table 9.1. These measurements indicate that the cooling scheme actually manages to cool down the atomic ensemble. We observed significantly better cooling on the old nanofiber, [Markussen, 2020], than on the new fiber, which gives us a lot of room for improvement of the cooling scheme implementation.

We saw in chapter 8 that we had to calibrate the Raman sideband ratio for the stretched transition. Calculations on the cancellation, shown in appendix B.1, showed that the optimum configuration of carrier detuning and modulation index is different on the stretched transition compared to the $(0 \rightarrow 0)$ transition. At the $\sim 4.7\,$GHz detuning we might be exerting a slight common mode Stark shift on the atoms. This will almost certainly project the thermal state of the atoms into a higher temperature state. Looking at the spectra taken on the stretched transition, compared to the $(0 \rightarrow 0)$ transition we also see slightly lower sideband frequencies, which can possibly be attributed to the modification of the potential due to the common mode Stark shift of the Raman laser.

Summary

We have used Raman transitions to resolve motional sidebands on both the $(0 \rightarrow 0)$ transition and on the stretched transition. We have employed a novel cooling scheme known as degenerate Raman cooling and have measured that the scheme is able to cool the atomic motion. We have found that offsets in the spectroscopic signal result in large modifications of the resulting temperature estimation, highlighting one of the major drawbacks of the method. We also observed broadening of the sidebands on the stretched transition, which magnetic field instability can possibly explain.

Using the $(-3 \rightarrow -4)$ transition leads to off resonant excitation of the neighboring transition, due to the unfavorable polarization content of the light. Doing the sideband spectroscopy on the $(-3 \rightarrow -3)$ transition would allow for larger Rabi frequencies at lower optical powers, possibly improving the resolution of the sidebands.

Having used the harmonic approximation of the sideband spectrum to estimate the temperature, we would now like to gain some insight into the validity of this approximation. In the next part we will simulate the trap potential and gain a deeper understanding of the trapped atoms.

Part III

Simulation Work

CHAPTER

10 SIMULATING A MULTILEVEL SYSTEM

In chapter 9 we found that we can resolve the motional sidebands of atoms trapped near the surface of a nanofiber. By using the ratio of the two sidebands areas we could estimate the temperature of the atomic ensemble. While taking the ratio of sidebands is a valid strategy for the harmonic potential, it is somewhat more complicated in the anharmonic potential. In order to evaluate the validity of the temperature estimation method we need to treat the actual trap potential.

In this chapter the Hamiltonian governing motional transitions will be derived along with the equations of motion, enabling the simulation of spectra.

10.1 The Lamb-Dicke Hamiltonian

An introduction to the coupling of motional levels was presented in chapter 2. In this chapter a more comprehensive treatment will be given, following the treatment given in [Gerry and Knight, 2005].
To begin, let us consider the case of a two-level atom in a harmonic trap potential interacting with monochromatic light. In this case the full Hamiltonian will be given by

$$H = \hbar\omega_0\sigma_3 + \hbar\nu\left(aa^\dagger + \frac{1}{2}\right) + \frac{\hbar\Omega}{2}\left(\sigma_+ e^{-i(\omega_L t - k_L x)} + \text{c.c}\right) \tag{10.1}$$

The first two terms are the atomic energy, where ω_0 is the transition frequency for the internal atomic state, $\sigma_3 = |e\rangle\langle e|$ is the excited state

population, ν is the motional frequency and a, $a^\dagger$ are the annihilation and creation operators of the trap potential. The last term describes the interaction between light and the trapped atom, with Ω as the Rabi frequency, $\sigma_{+(-)}$ the atomic raising(lowering) operator and ω_L and k_L as the laser frequency and wavenumber. In the standard treatment of the two-level atom we neglect the spatial phase contribution, but if the light has a spatial decay, which is significant on the scale of the atomic motion, then this can be represented by an imaginary wavenumber. This allows us to rewrite the interaction term in equation 10.1,

$$H_I = \frac{\hbar\Omega}{2}\left(\sigma_+ e^{-i\omega_L t} e^{-k_L x} + \text{c.c}\right). \tag{10.2}$$

The strong confinement of atoms in the trap results in discretization of the atomic motion. We can therefore write the position variable x as an operator,

$$\hat{x} = \sqrt{\frac{\hbar}{2\nu M}}(a + a^\dagger) \tag{10.3}$$

where M is the atomic mass and $a^{(\dagger)}$ is the annihilation(creation) operator for motional excitations. We can define a quantity,

$$\eta \equiv k_L \sqrt{\frac{\hbar}{2\nu M}}, \tag{10.4}$$

known as the Lamb-Dicke parameter. In the limit of small η the exponential decay in equation 10.2 can be Taylor expanded to first order. In the interaction picture the interaction Hamiltonian then becomes

$$H_I = \frac{\hbar\Omega}{2}\left(\sigma_+\left(e^{i\Delta t} - \eta\left(a e^{i(\Delta+\nu)t} + a^\dagger e^{i(\Delta-\nu)t}\right)\right) + \text{c.c.}\right), \tag{10.5}$$

where $\Delta = \omega_L - \omega_0$ is the detuning with respect to the atomic transition. The matrix elements between the states of a harmonic potential with the annihilation and creation operators are

$$\langle n|a|n+1\rangle = \sqrt{n}$$

$$\langle n+1|a^\dagger|n\rangle = \sqrt{n+1}$$

which allows us to write up the Hamiltonian for an atom in the nth motional state,

$$H_I = \frac{\hbar\Omega}{2}\left(\sigma_+\left(e^{i\Delta t} - \eta\left(\sqrt{n}e^{i(\Delta+\nu)t} + \sqrt{n+1}e^{i(\Delta-\nu)t}\right)\right) + \text{c.c.}\right). \tag{10.6}$$

This can of course be expressed for a general potential as

$$H_I = \frac{\hbar\Omega}{2}\left(\sigma_+\left(e^{i\Delta t} - \Omega_{n,n-1}e^{i(\Delta+\nu_{n,n-1})t} - \Omega_{n,n+1}e^{i(\Delta-\nu_{n,n+1})t} + \text{c.c.}\right)\right) \tag{10.7}$$

where $\Omega_{n,n'}$ is the transition matrix element between motional state n and n' and $\nu_{n,n'}$ is the transition frequency.

We can then write a Hamiltonian with n motional levels as a $2n \times 2n$ block matrix,

$$\mathbf{H}_I = \left(\begin{array}{c|c} 0 & \mathbf{A} \\ \hline \mathbf{A}^\dagger & 0 \end{array}\right) \tag{10.8}$$

where we have sorted our states such that the upper left block of zeros corresponds to all the ground state motional levels and the lower right block corresponds to all the excited state motional levels. They are set to zero since we assume that motional transitions may only occur along with a change of the internal state of the atom. The matrix $\mathbf{A}$ is given by

$$\mathbf{A} = \frac{\hbar\Omega}{2}\begin{pmatrix} e^{i\Delta t} & -\tilde{\Omega}_{0,1}(t) & & \\ -\tilde{\Omega}_{1,0}(t) & e^{i\Delta t} & \ddots & \\ & \ddots & \ddots & -\tilde{\Omega}_{n-1,n}(t) \\ & & -\tilde{\Omega}_{n,n-1}(t) & e^{i\Delta t} \end{pmatrix}, \tag{10.9}$$

where $\tilde{\Omega}_{n,n'}(t)$ is now defined as $\Omega_{n,n'}e^{i(\Delta\pm\nu_{n,n'})}$ with $\nu_{n,n'}$ being the transition frequency between n and n'. The main diagonal of $\mathbf{A}$ corresponds to carrier transitions and thus are independent of motional level in this approximation. The upper diagonal are elements that increase the motional quantum number and the lower diagonal are elements that lower the motional quantum number.

The validity of this Hamiltonian rides on the assumption that we can Taylor expand the exponential decay of the field to only first order. However, if the field decay is sufficiently fast, this is no longer a good approximation. In that case higher order terms of the expansion have to be taken into account. This will, for the harmonic potential lead to a second order term,

$$\langle n|\,\eta^2\left(a+a^\dagger\right)^2|n'\rangle = \langle n|\,\eta^2\left(a^2+a^{\dagger 2}+2aa^\dagger-1\right)|n'\rangle \tag{10.10}$$

From this we see two things; one is the fact that higher order transfers are possible, i.e. two phonon increase of motional energy. The other is the fact that the carrier transitions will be affected by the motional state of the atom. This means that the Rabi frequency of the carrier will depend on the temperature of the ensemble. And there will, in principle, be even higher order terms.

10.2 The Von Neumann Equation

The states interacting with the light can be expressed using the density matrix, defined as

$$\rho = \sum p_j \left|\psi_j\right\rangle \left\langle\psi_j\right| , \tag{10.11}$$

The time evolution of the density matrix in the interaction picture is governed by the Von Neumann equation[Steck, 2008],

$$\dot{\rho}_I = -\frac{1}{i\hbar}\left[H_I, \rho_I\right] , \tag{10.12}$$

where ρ_I is the density matrix in the interaction picture. This differential equation allows us to calculate the effect of the interaction on the atomic population. We can solve this differential equation with fourth order Runge-Kutta integration using the `SciPy.integrate` python library, [Dormand and Prince, 1980].
To solve the time evolution we need an initial state of the system $\rho_I(0)$. In order to include the effects of a finite temperature on the ensemble we need to setup the initial state in a thermal distribution,

$$\rho_{I,n,n}(0) = \frac{e^{-\frac{\hbar\omega_n}{k_\mathrm{B}T}}}{\sum_{n=0} e^{-\frac{\hbar\omega_n}{k_\mathrm{B}T}}} \tag{10.13}$$

where $\rho_{I,n,n}(0)$ is the nth diagonal entry of the initial density matrix, k_B is the Boltzmann constant, T is the temperature and ω_n is the frequency of the nth motional level. The initial state should, in principle, be determined by the Bose-Einstein distribution, but we are far from the condensation temperature, so the Boltzmann factor is sufficient.

10.3 Generalizing to anharmonic potentials

To generalize the model to an arbitrary potential we need to find the individual Rabi frequencies for the transitions between the different motional levels. This can be expressed as

$$\Omega_{n,n'} = \int_{-\infty}^{\infty} \psi_n I(x) \psi_{n'} dx, \tag{10.14}$$

where $\psi_{n,(n')}$ are the wavefunctions of the trapping potential and $I(x) = I_0 u(x)$ is the intensity[1] with $u(x)$ as the mode profile. We see that in the case of a constant mode, i.e. no spatial dependence, the only non-zero terms are where $n = n'$. These coefficients between motional states are commonly known as the Franck-Condon factors. Factoring out I_0 from eq. 10.14 we get a purely geometric quantity describing the transition strength.

We can then write the interaction as the elementwise product of two matrices,

$$\mathbf{A} = \mathbf{\Omega} \odot \boldsymbol{\delta} \tag{10.15}$$

where

$$\mathbf{\Omega}_{n,n'} = \frac{\hbar\Omega}{2} \langle n | \, u \, | n' \rangle$$

are the elements of the matrix $\mathbf{\Omega}$, given by the overlaps of the wavefunctions with the driving mode, and where

$$\boldsymbol{\delta}_{n,n'} = \exp\left(i \left(\Delta + \omega_n - \omega_{n'}\right) t\right)$$

are the elements of the time dependence matrix, given by the energy level spacing.

The matrix $\mathbf{A}$ contains all of the possible transitions between motional states, with the associated time dependence. Evaluating this matrix requires the wavefunctions with their respective energies. Therefore, to carry out the full simulation, we have to find wavefunctions of the trap potential.

[1] The intensity is used here since we are driving Raman transitions

CHAPTER

11 ONE DIMENSIONAL SIMULATION

In the previous chapter we saw how a two-level atom with motional levels can be simulated. We also formulated the general expression for the Hamiltonian of an arbitrary trap potential and driving field. To gain an insight into the behavior of the trapped atoms in the specific case of a nanofiber trap potential we have to do a number of things,

- Find the wavefunctions of the trap potential,
- find the overlap of wavefunctions, given a specific mode profile,
- and calculate the time evolution of a thermal state for different frequencies

We will begin by deriving the numerical method for solving the one dimensional Schrödinger equation, we will then explore the consequences of the solutions and simulate Raman spectra. The Raman spectra will then be compared to the temperature estimation method used in chapter 9.

11.1 Finite difference method in 1d

The method for calculating the wavefunctions in one dimension is known as finite difference method. It makes use of a homogeneous spatial grid

to define the spatial derivatives. To find the wavefunctions of the potential we have to solve the time independent Schrödinger equation,

$$H\Psi = E\Psi \tag{11.1}$$

where E are the energies of the Hamiltonian. The Hamiltonian consists of a kinetic and potential contribution

$$H = -\frac{\hbar^2}{2m}\frac{\partial^2}{\partial x^2} + U(x). \tag{11.2}$$

We can write this as

$$H = -\frac{\partial^2}{\partial x^2} + \frac{2mk_{\mathrm{B}}}{\hbar^2}U(x), \tag{11.3}$$

where k_B is the Boltzmann constant and m is the mass of Cesium. This ensures that the potential, given in Kelvin has the proper units. On a discrete grid the partial derivative can be written as a difference equation,

$$\frac{\partial^2\Psi(x)}{\partial x^2} = \frac{\Psi(x-\delta) - 2\Psi(x) + \Psi(x+\delta)}{\delta^2}, \tag{11.4}$$

with δ as the grid spacing. This operator can be written in terms of an $n \times n$ matrix, where n is the number of grid points. The potential can be written as an $n \times n$ diagonal matrix, giving us the Hamiltonian,

$$\mathbf{H} = \frac{-1}{\delta^2}\begin{pmatrix} -2 & 1 & & \\ 1 & -2 & \ddots & \\ & \ddots & \ddots & \\ & & & \end{pmatrix} + \frac{2mk_B}{\hbar^2}\begin{pmatrix} U(x_0) & & & \\ & U(x_1) & & \\ & & \ddots & \\ & & & U(x_n) \end{pmatrix} \tag{11.5}$$

where $U(x_n) = U(x_0 + n\delta)$ is the potential at the nth point on the grid. Finding the wavefunctions and the eigenenergies is simply a matter of solving this eigenvalue problem.

11.2 Wavefunctions in one dimension

With the tools developed in the previous section we can solve the one dimensional radial trap potential. Some of the wavefunctions of a trap potential with trap powers of $P_{\mathrm{Blue}} = 8\,\mathrm{mW}$ and $P_{\mathrm{Red}} = 2 \times 0.72\,\mathrm{mW}$

are plotted in figure 11.2. To improve visibility we plot every fifth wave function, with the wavefunctions vertically spaced by their respective energies. The anharmonicity of the trapping potential leads to the energy spacing becoming smaller for larger motional energies. The energies are plotted in figure 11.1.

We note that as we approach the top of the potential the transition frequencies approach zero. This is due to the fact that the potential asymptotically reaches zero and therefore the motional states become continuous. With a power of $P_{\text{blue}} = 8\,\text{mW}$ and $P_{\text{Red}} = 2 \times 0.72\,\text{mW}$ we

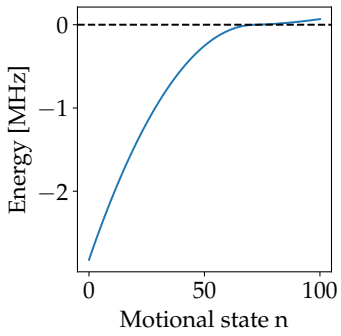

Figure 11.1 — The energies of the one dimensional trap potential. Dashed line indicates the top of the potential.

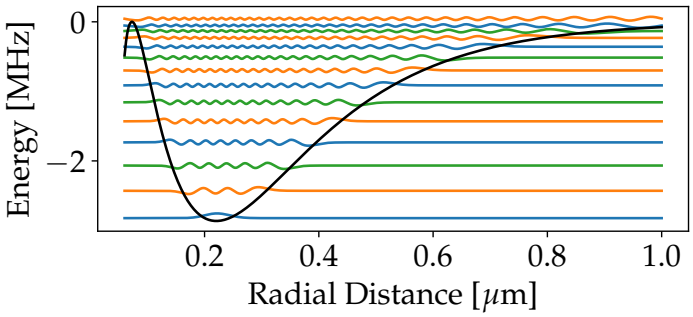

Figure 11.2 — Every fifth wave function of the radial trap potential at $P_{blue} = 2\times 4$mW, spaced by the respective energies in MHz. Fundamental frequency of 81 kHz. The scale of the wavefunctions has been adjusted to improve legibility.

get a transition frequency of the lowest transition of $81\,\text{kHz}$. The transition frequency for the ground state for a number of powers is plotted in figure 11.3. This shows that increasing the trap power results in a deeper trap with larger trap frequencies.

The wavefunctions in figure 11.2 tell us that for increasing motional energy the position of the atoms moves away from the surface of the fiber. The expectation value of the radial distance, $\langle n|\, r\, |n\rangle$, is plotted in figure 11.4.

We can also find the wavefunctions in the axial and azimuthal degrees of freedom. These are plotted in figure 11.5. We note that these spectra are far more harmonic than the radial potential. We find the ground state transition frequencies to be $65\,\text{kHz}$ and $134\,\text{kHz}$ for the azimuthal and axial potential, respectively.

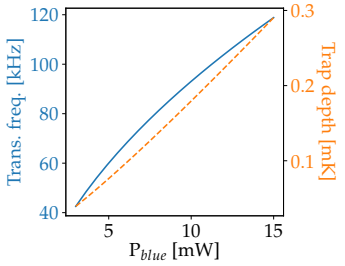

Figure 11.3 — Trap frequency and depth as a function of P_{blue}.

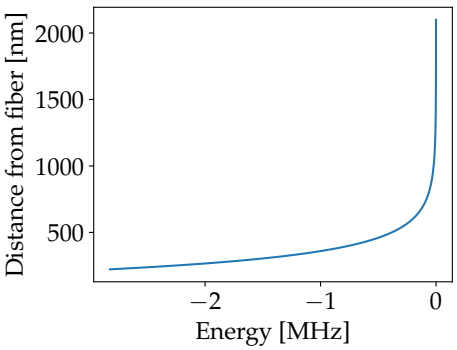

Figure 11.4 — Expectation value of the radial distance as a function of energy.

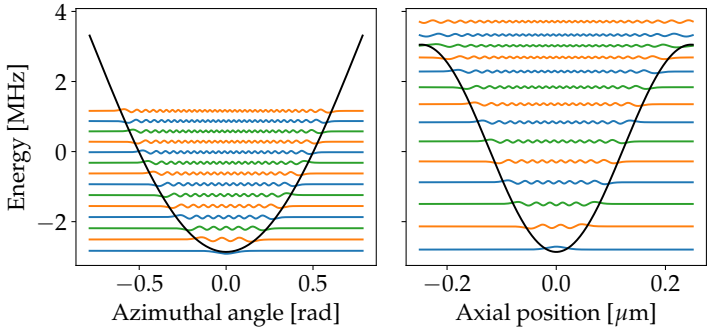

Figure 11.5 — The azimuthal and axial potential with wavefunctions. Every fifth wavefunction is plotted and spaced by the respective energy. The ground state trap frequencies are 65 kHz and 134 kHz for the azimuthal and axial potential, respectively.

11.2.1 Franck-Condon factors

Having found the wavefunctions we can now calculate the Franck-Condon factors, presented in chapter 10.3. The Franck-Condon factors are calculated in the discrete case in the following way,

$$\mathbf{\Omega_{n,n'}} = \frac{\hbar\Omega}{2}\Psi_n \cdot (\Psi_{n'} \odot u). \tag{11.6}$$

Here u is the mode profile as a vector and $\odot$ is the Hadamard product, i.e. the element-wise multiplication of two matrices. The Rabi frequencies for Raman transitions are given by products of electric fields and therefore we will use the intensity profile as the mode in the calculations

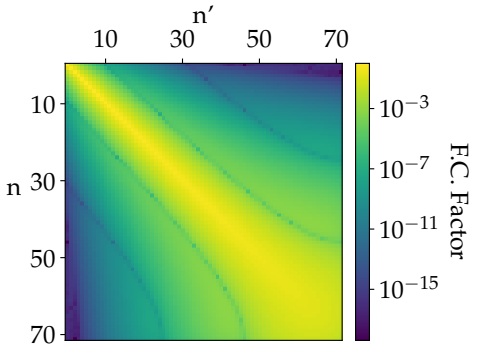

Figure 11.6 — The overlaps of the one dimensional wavefunctions with an exponential mode profile, $\langle n| u |n'\rangle$. The color bar is logarithmic.

of the Franck-Condon factors. There is some degree of choice when it comes to normalizing the mode profile. Our choice is made such that the element $|\langle 0| u |0\rangle| = 1$.

To facilitate a coupling there needs to be a significant gradient of the intensity. This eliminates the axial part of the potential, since the Raman light propagates as a running wave and thus has no decay along the fiber. The azimuthal part of the Raman light is symmetric around the trap minimum, which means that only transitions between states of equal parity are allowed. This will, for the lowest energy levels, be two phonon transitions, which have smaller Franck-Condon factors, i.e. $\propto \eta^2$. This leaves us with the radial part of the potential. Since we have an exponential decay this allows for coupling between the motional states. The full Franck-Condon matrix is shown in figure 11.6. Note that the color bar is logarithmic to allow for the resolution of smaller structures within the matrix. We note that the Rabi frequency of the carrier goes down as the motional energy goes up. This can be explained by the expectation value of the radial distance as seen in figure 11.4. As the motional energy increases, the atoms see less of the light and therefore have a weaker interaction. We also see that highly excited motional states can more easily couple to other states. This shows that approximating the interaction as linear is not actually viable in the real potential.

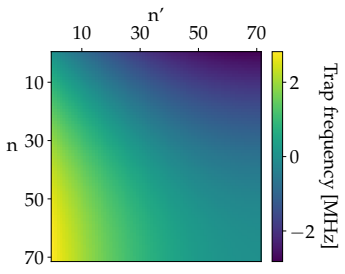

Figure 11.7 — Transition frequencies between all motional states of the one dimensional radial potential.

11.3 Simulating Raman spectra

We now have the necessary prerequisites to calculate the Raman spectrum of an atomic ensemble at any sufficiently low temperature. Since we know the energies of the motional states we can calculate the transition frequency between every state, shown in figure 11.7.

A spectrum at 20 μK is plotted in figure 11.8. The asymmetry of the sidebands is clearly pronounced, with a slight asymmetry of the amplitudes. We can estimate the temperature, the same way as presented in chapter 9, i.e. fit the motional sidebands to a skewed gaussian, equation 9.3, then calculate the area and the mean frequency of the sidebands. These are then put into

$$T = -\frac{\hbar\omega_{sb}}{k_B}\frac{1}{\ln(r_{sb})} \tag{11.7}$$

to find the temperature. The sidebands with fits are plotted in figure 11.9. From the fit we find a temperature of 22 μK compared to the actual value of 20 μK. We can do the same procedure for a series of spectra, ranging in temperate from 4 μK to 50 μK.

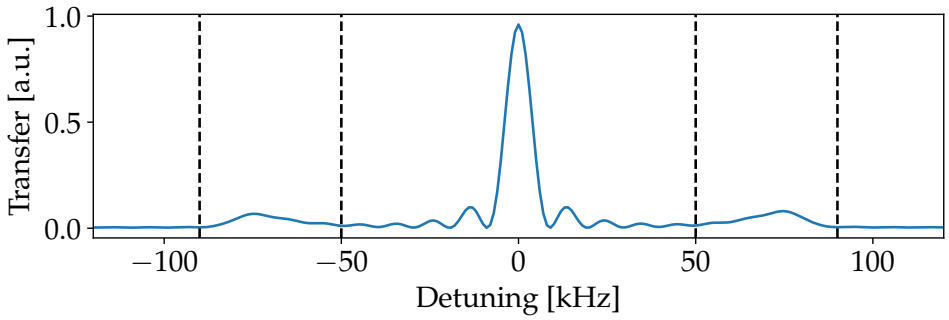

Figure 11.8 — Simulation of Raman spectrum at 20 μK using 72 motional states and a ground state Rabi frequency of 5 kHz. Dashed lines indicate motional sidebands.

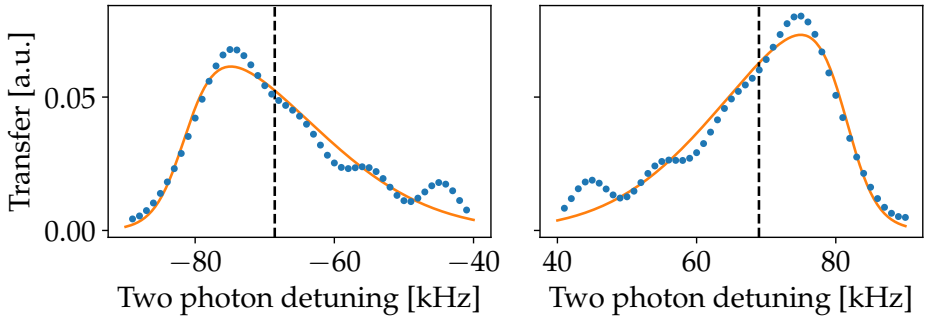

Figure 11.9 — Sidebands from figure 11.8 fitted to a skewed gaussian, equation 9.3. Vertical dashed lines denote the mean sideband frequency.

The temperatures as a function of sideband ratio are plotted along with the true temperatures in figure 11.11. It is clear that determining the temperature using this method is mostly accurate when used in low temperature regimes. When the sideband ratio becomes larger than 0.8 the temperature races off and small noise contributions will lead to large changes in temperature, which may be the explanation for the behavior seen in chapter 9 on the $(0 \to 0)$ transition. We can, however, see that in the low temperature domain the estimated temperatures follow the actual temperatures. From these calculations we see that the estimation method systematically overestimates the temperature. Using the sideband ratio as a measure for the temperature becomes somewhat problematic at very low temperatures. This is due to the fact that the lower motional sideband gets so small that noise can begin to impact the temperature estimate. An example of a 100 nK spectrum is plotted in figure 11.10. At very low temperatures it is therefore only possible to give an upper bound on the temperature.

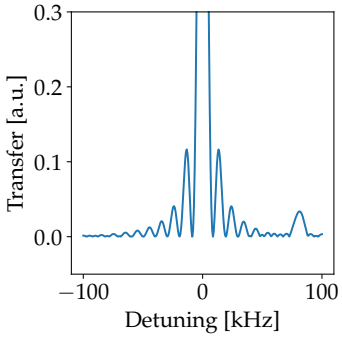

Figure 11.10 — Simulated spectrum at 100 nK

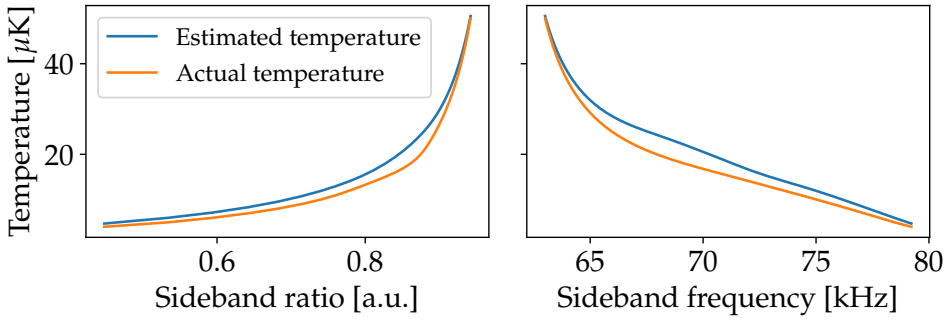

Figure 11.11 — Estimated temperature as a function of sideband ratio(left) and sideband frequency(right). The actual temperature is also plotted for reference.

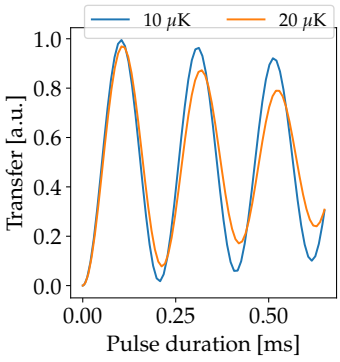

Figure 11.12 — Carrier Rabi oscillations at $10\,\mu$K and $20\,\mu$K with a ground state Rabi frequency of 5 kHz. The contrast of the oscillations goes down as the temperature increases.

From these simulations we can also see the effect of the carrier Rabi frequency at different temperatures, figure 11.12. In chapter 9 we saw how the Rabi oscillations from the Raman interactions decayed over time. This decay can be attributed to the interference of different carrier Rabi frequencies. The distribution of motional energy will change the spectrum of the carrier transition and thus lead to a temperature dependent decay of the Rabi oscillations. This model also allows for revival of Rabi oscillations, plotted in figure 11.13. Whether this can reasonably be measured in the real experiment is debatable since the interaction with the Raman light will lead to occasional spontaneous emission. Additionally since the Lamb-Dicke parameter for our trap is not zero, there will be a finite amount of scattering leading to a change of the motional state. However, the timescale on which the revival of the Rabi oscillations occur is not unreasonable and therefore would be testable in our experimental setup. The revival of Rabi oscillations in addition to the state dependent Rabi frequency is reminiscent of the Jaynes-Cummings model in cavity quantum electro dynamics. The ability to drive motional states at different Rabi frequencies opens up the opportunity to make non-trivial states of the atomic ensemble. For instance one can create entanglement between motional and internal states. In the discussion of the temperature estimation of the experimental data we found that an offset in the signal would result in a large change in the estimated temperature. The possible origins of the signal offsets were discussed, however we also find a similar effect occurring in the simulations of the motional spectra. Figure 11.14 shows a simulation at 60 μK. The scale has been exaggerated to highlight the signal pedestal

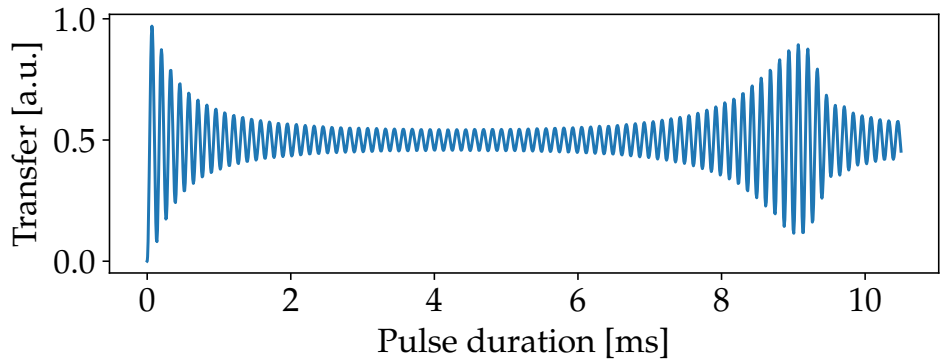

Figure 11.13 — Revival of Rabi oscillations. The simulation is done at $20\,\mu$K, with a ground state Rabi frequency of 10 kHz. We note that the Rabi oscillations decay initially, but revive after ~ 6 ms.

on which the sidebands and carrier sit. As seen in the Franck-Condon matrix the Rabi frequencies between states increases for large n. In the case of a high temperature ensemble, atoms will be inhabiting high energy motional levels and therefore higher order transitions are made possible. This can now happen over a long range of frequencies leading to a broadband signal increase.

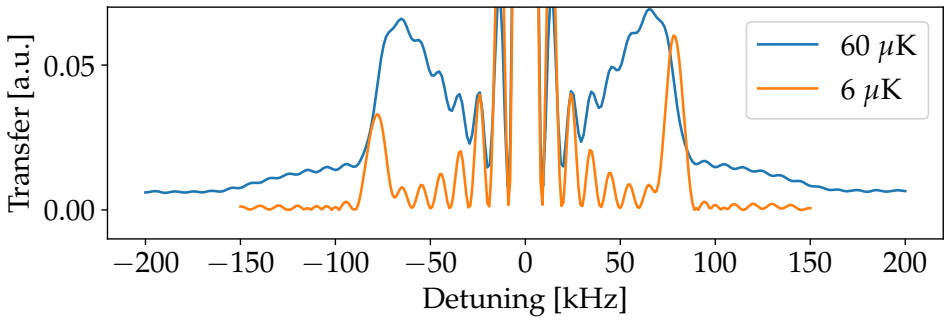

Figure 11.14 — Signal offset of a spectrum simulated at $60\,\mu$K compared to a spectrum at $6\,\mu$K. A significant broadband noise pedestal appears as the temperature of the atomic ensemble is raised.

CHAPTER

12 TWO DIMENSIONAL SIMULATION

In the previous section we treated the trap potential in the one dimensional case. Due to the non-separability of the potential we cannot expect to fully understand the motional states by only considering one dimension. We therefore extend our treatment to two dimensions. This chapter details the efforts towards doing Raman spectrum simulations of the two dimensional trap potential. The scaling of the problem, however, proved to be a significant obstacle. The work, nonetheless, paves the way towards more realistic simulations of the physical system.

12.1 Finite difference method in 2d

The method for finding the wavefunctions in two dimensions is essentially the same as the one dimensional case. The resulting wavefunctions of this problem are two dimensional and thus are described by a 2d matrix. In order to apply the methods of eigenvalue analysis we need to flatten the wavefunctions into single column vectors. This in turn means that for wavefunctions on an $N \times N$ grid of points, the Hamiltonian has size $N^2 \times N^2$. This scaling means that one has to consider the computational costs.

We will now derive the form of the 2d finite difference Hamiltonian. Just like in the previous section we need to formulate a discrete second

derivative. In the 2d case the time independent Schrödinger equation is

$$E\Psi(x,y) = \left[-\frac{\hbar^2}{2m}\left(\frac{\partial^2}{\partial x^2} + \frac{\partial^2}{\partial y^2}\right) + U(x,y)\right]\Psi(x,y). \tag{12.1}$$

As with the one dimensional case the kinetic part can be discretized via the following difference equation

$$\left(\frac{\partial^2}{\partial x^2} + \frac{\partial^2}{\partial y^2}\right)\Psi(x,y) = \frac{\Psi(x,y-\delta_y) - 2\Psi(x,y) + \Psi(x,y+\delta_y)}{\delta_y^2} + \frac{\Psi(x+\delta_x,y) - 2\Psi(x,y) + \Psi(x-\delta_x,y)}{\delta_x^2} \tag{12.2}$$

where $\delta_{x,y}$ are the grid spacings in the x and y directions. We can write this in terms of a matrix

$$\nabla^2 = \begin{pmatrix} -2D_{xy} & 1/\delta_x^2 & & 1/\delta_y^2 & \\ 1/\delta_x^2 & \ddots & \ddots & & \ddots \\ & \ddots & & & \\ 1/\delta_y^2 & & & & \\ & \ddots & & & \end{pmatrix} \tag{12.3}$$

where

$$D_{xy} = \frac{1}{\delta_x^2} + \frac{1}{\delta_y^2}.$$

We can define the two dimensional potential as a diagonal matrix,

$$\mathbf{U}(x,y) = \begin{pmatrix} U(x_0,y_0) & & & & \\ & \ddots & & & \\ & & U(x_n,y_0) & & \\ & & & \ddots & \\ & & & & U(x_n,y_n) \end{pmatrix} \tag{12.4}$$

where $U(x_n, y_{n'}) = U(x_0 + n\delta_x, y_0 + n'\delta_y)$ is the potential at the (n, n')th point on the grid. The full Hamiltonian will thus be,

$$\mathbf{H} = -\nabla^2 + \frac{2mk_\mathrm{B}}{\hbar^2}\mathbf{U}(x,y). \tag{12.5}$$

As previously stated, this problem scales as $\sim n^4$ and therefore is quite computationally taxing. To reduce computation times and memory requirements we make use of sparse matrices. Using the `SciPy`

sparse library we can define the Hamiltonian in a much more economic way, [Virtanen et al., 2020]. Since the Hamiltonian is Hermitian we can further speed up the computation using `SciPy.eigsh`. This function returns n eigenvectors in order of eigenvalue.

12.2 Two dimensional wavefunctions

Using the equations derived in the previous section we can find the wavefunctions of the two dimensional potential. We focus on the transverse potential, i.e. the potential at a fixed axial coordinate. The first six wavefunctions in terms of energy are plotted in figure 12.1. The green and blue contour lines indicate equipotential lines of the trapping potential, with trapping powers of $P_{\text{blue}} = 8\,\text{mW}$ and $P_{\text{red}} = 2 \times 0.7\,\text{mW}$. The low energy wavefunctions are very reminiscent of wavefunctions of the harmonic potential. We can assign a number of radial and azimuthal excitations to the wavefunctions. From this we find that the ground state transition frequency is $113\,\text{kHz}$ for the first radial transition and $88\,\text{kHz}$ for the first azimuthal transition. We note that this trap frequency is higher for both degrees of freedom than the one dimensional potentials.

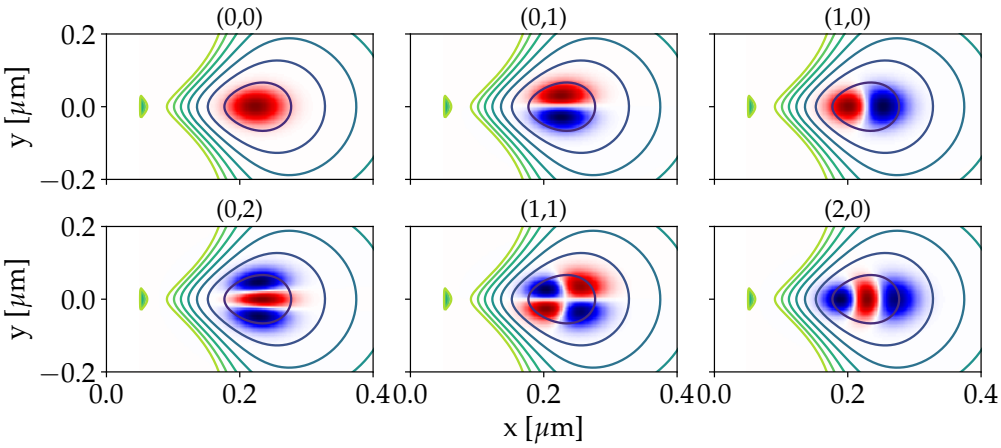

Figure 12.1 — Plot of the first six wavefunctions in order of energy. Contour lines show the trap potential. Blue and red colors indicate the sign of the wave function. The wavefunctions can be assigned a number of radial and azimuthal excitations shown as (n_r, n_a). $x = 0$ indicates the surface of the nanofiber.

The non-separability of the potential becomes apparent when look-

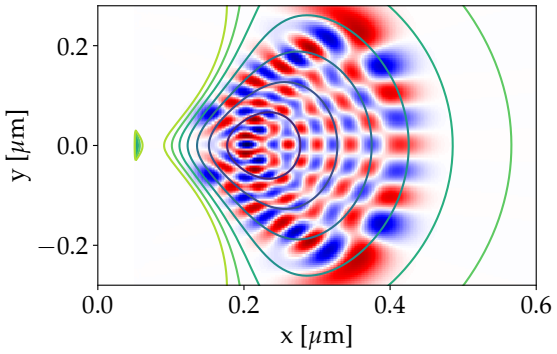

Figure 12.2 — The 170th wave function in order of energy. The wavefunction exhibits the break down of the radial and azimuthal separation. $X = 0$ indicates the surface of the nanofiber.

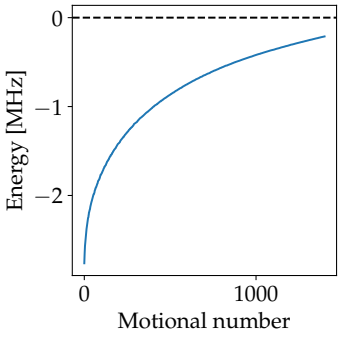

Figure 12.3 — Eigenenergies of the first 1400 wavefunctions of the two dimensional trap potential. The edge of the potential at 0 K is indicated by a dashed line.

ing at highly excited states of the potential. The 170th wavefunction is plotted in figure 12.2. It is clear that one cannot assign a reasonable number of radial and azimuthal excitations. We are, so to say, mixing the motional degrees of freedom more at larger motional energies.

The first 1400 energies are plotted in figure 12.3. If we, for the moment, imagine a two dimensional harmonic potential, with degenerate trap frequencies, then we can divide out n excitations in $n + 1$ different ways. This means that for an energy $E(n)$ in one dimension we need n^2 states in two dimensions to reach the same energy level. The spectrum seen in figure 12.3 shows that with 1400 states we do not reach the top of the potential. This happens to be an important fact for the simulations of Raman spectra. This will be discussed in more detail in the section 12.3.

Figure 12.4 shows the expectation value of the radial distance from the fiber surface. Like the one dimensional case the distance increases with increasing energy. The distances shown are calculated from the first 400 wavefunctions.

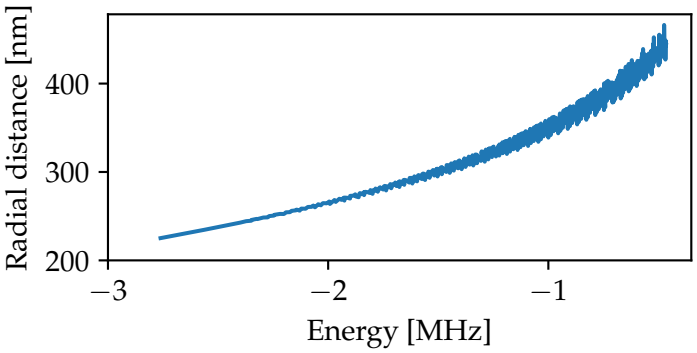

Figure 12.4 — The expectation value of the radial coordinate for the two dimensional potential as a function of energy. First 700 wavefunctions are displayed.

12.2.1 Franck-Condon factors

In the same manner as the one dimensional treatment, we find the transition matrix elements between all of the wavefunctions. We can once again argue for why the transverse plane of the fiber makes for the most interesting physics by considering the lack of decay in the axial degree of freedom. In order to calculate the Franck-Condon factors we need to know the intensity distribution of the evanescent field.

The Raman mode is plotted in figure 12.5. The mode of the Raman light has a near exponential decay radially and a sinusoidal dependence in the azimuthal degree of freedom. To calculate the Franck-Condon factors in two dimensions, we first calculate the mode of the Raman intensity. We then loop over all of the wavefunctions, summing over the elementwise multiplication of the states. The resulting Franck-Condon factors are plotted in figure 12.6. We see the same sort of behavior as in the one dimensional case; states with larger energy can couple to more levels. Unlike the one dimensional case, where the states are naturally in a nice order, we get a different kind of sorting of the wavefunctions in 2d. This leads to a different structure of the transition elements. This should, however, make no difference for the applicability of this method.

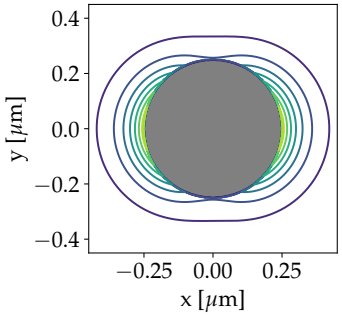

Figure 12.5 — Contour plot of the transverse intensity distribution of the Raman light.

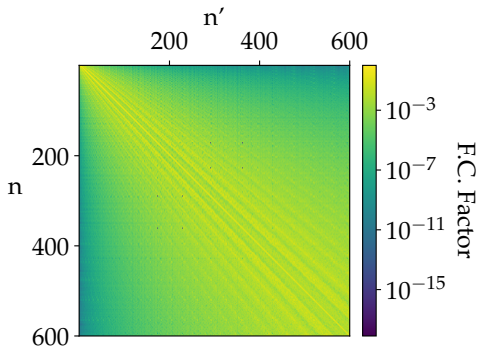

Figure 12.6 — Franck-Condon coefficients of the two dimensional trap potential. Note the logarithmic color bar.

12.3 Simulating Raman spectra

With the Franck-Condon factors we can calculate the Raman spectrum. It is noteworthy, that we cannot cover the full spectrum of motional states with the computational resources that we have at our disposal. This means that we can only simulate spectra at low temperatures. Figure 12.7 shows the Boltzmann factors for a series of temperatures as a function of the eigenenergies found in figure 12.3. From the 1400 states we can try to approximate how many states are necessary to represent the ensemble at a given temperature. We define the ratio of population

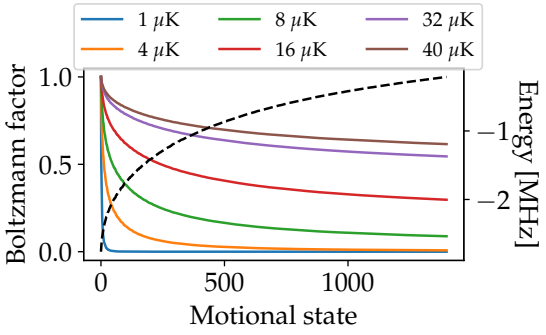

Figure 12.7 — The Boltzmann factor for the motional states at temperatures between 2 μK and 32 μK. The state energy is plotted as a dashed line.

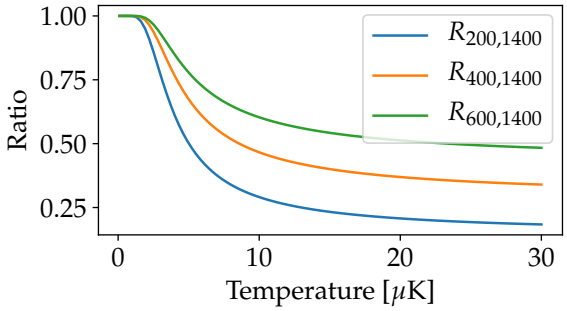

Figure 12.8 — Ratio of the partition functions of different numbers of states to the partition function of 1400 states.

in the following way,

$$R_{N,N'}(T) = \frac{\sum_{n=0}^{N} e^{\frac{-\hbar\omega_n}{k_B T}}}{\sum_{n=0}^{N'} e^{\frac{-\hbar\omega_n}{k_B T}}} \tag{12.6}$$

where N' is the total number of states available and where ω_n is the frequency of the nth energy level. In this case the maximum number of states available is 1400. The ratios for different temperatures are plotted in figure 12.8.

As expected, low temperature ensembles can be nicely represented with only a few states. However we already see a large discrepancy at temperatures close to $10\ \mu$K. We can simulate a spectrum at $1\ \mu$K, shown in figure 12.9, using 200 and 400 states. This should, based on the calculations of figure 12.8, lead to more or less identical spectra. However, the spectrum using 400 states exhibits some new features, which do not show up in the other spectrum. One would expect that including more states would simply make the simulation more accurate, however these features are nowhere to be seen in the experimental data and they do not show up in the 1d simulations.

The origin of these erroneous peaks could be several different things. Since these peaks show up for systems of a larger number of states it is possible that somehow the calculation of the matrix elements of the Franck-Condon matrix are wrong. As we increase the energy, we also increase the extent of the wavefunctions. This, in principle, means that one has to extend the domain on which the wavefunctions are calculated. This also means that to ensure accurate Franck-Condon factors one has to use a large potential domain and a large number of points,

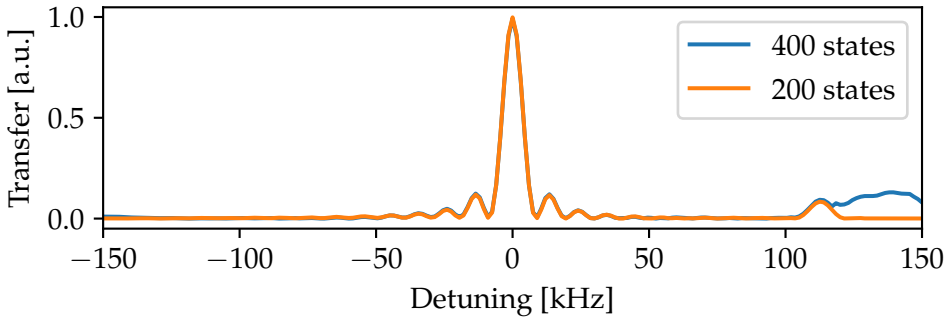

Figure 12.9 — Spectra simulated at $1\,\mu$K using 200 and 400 states, with a ground state Rabi frequency of $5\,$kHz and a pulse duration of $100\,\mu$s. Note the additional peak in the spectrum using 400 states.

seeing as when the domain increases in size, the grid density decreases. A large discrepancy in the Franck-Condon factors would manifest itself in the matrix in figure 12.6, however, we do not see such behavior. The wavefunctions used to calculate the Franck-Condon factors are simulated on a 500×500 grid with x and y coordinates ranging from 0 to 1.5 μm in x and -1.7 to 1.7 μm in y. This should be plenty large to represent wavefunctions at the appropriate energies.

What seems like a more probable source of the error is numerical instability. Working with 400 states means that the Hamiltonian is an 800×800 matrix. On top of this, the elements of the Hamiltonian have widely varying time dependences as seen in figure 12.10. This is related to the so called stiffness of the system of equations, [Shampine and Gear, 1979]. The stability of a stiff system of equations is highly dependent on the size of the time step used in the integration. In our treatment we use a 4th order Runge-Kutta integration method. This method is not built to handle stiff ordinary differential equations. Therefore this could be the origin of the large error in the integration, when using many wavefunctions.

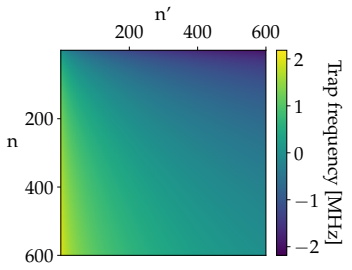

Figure 12.10 — Transition frequencies between each of the first 600 motional states of the 2D trap potential.

Despite these obstacles, the work on the 2d simulations lays the groundwork for more in-depth simulations of the trapping potential. Optimizing the code for larger systems of stiff equations will allow us to better simulate the spectra. Furthermore, the numerical results found in this fully quantum method could be compared with classical ensemble calculations, such as in [Markussen et al., 2020]. This could give us some insight into the intersection of the classical point particle trajecto-

ries and the wavefunction approach.

Since we know that the potential is non-separable, it is of course also worth investigating the three dimensional potential. As we have seen, going from one dimension to two, the transition frequencies are affected by the other degrees of freedom. There is of course no reason why this should not also be the case in three dimensions. Extending the model to three dimensions is, in abstract terms, a simple procedure, however, the computational requirements are much higher and therefore it is beyond the scope of this work.

CHAPTER

13 CONCLUSION

This brings us to the conclusion of this thesis, where the key results will be summarized and a few comments on future paths for the experiment will be given.

In the first part of the thesis we developed some of the key physical concepts for understanding the physics of our experiment. We saw how a two-level atom interacts with light and were able to extend the treatment to multi-level atoms. The interaction of the atoms with far detuned light led to a dipole force, which could be leveraged to trap neutral atoms. We saw how the evanescent field of a sub-wavelength optical fiber could be used to trap Cesium atoms in a potential well.

In the second part we successfully pulled, characterized, and installed a new nanofiber into the experimental setup. The experimental setup was presented, along with the two-color heterodyne detection setup and the dipole force-free Raman scheme. The trap parameters were investigated to find the optimum trap configuration for maximal loading. We found that there was noise, which is yet to be mitigated. We also showed that the dipole force-free Raman scheme could be calibrated to cancel differential Stark shifts, however, we also discovered a significant systematic flaw in the experimental procedure for cancelling the Stark shifts, requiring a different approach on the stretched transition. Finally we used Raman transitions to resolve the motional sidebands of the trap potential. This allowed for the measurement of the temperature based on the sideband asymmetry. We applied a novel cooling scheme, taking advantage of the fictitious field generated by

the blue trap light. We saw how systematic errors had a significant impact on the temperature estimation and presented different methods of accounting for the aforementioned errors.

In the last part of the thesis, we delved into simulating the motional states of the trap potential to gain an insight into the merits of the temperature estimation method. We first developed the necessary theoretical background for simulating multi-level systems and finding wavefunctions of arbitrary potentials numerically. The wavefunctions of the one dimensional radial trap potential were found and subsequent simulations of the Raman spectra were carried out. We saw agreement between our temperature estimation method and the temperature used in the simulations. We also saw the emergence of temperature dependent effects on the carrier transitions. The model was extended to treat the two dimensional trapping potential, with the wavefunctions exhibiting properties characteristic of a non-separable potential. We did, however, find that technical limitations kept us from fully simulating the two dimensional potential. Despite this, the treatment of the two dimensional potential paves the way towards increasingly deep understanding of the motional states of the trapping potential.

While we were able to estimate the temperature of the atomic ensemble, certain practical limitations still limit the confidence with which we can quote a temperature. An immediate improvement to the thermometry of the cooled atoms would be to run the spectroscopy on the $(-3 \rightarrow -3)$ transition as opposed to the $(-3 \rightarrow -4)$ transition. An investigation into the effects of magnetic field fluctuations would also be prudent. We also found that the efficacy of the cooling was worse on the new fiber, compared to the old fiber, the reason for which has yet to be determined. Investigation into the possible heating mechanisms might allow us to better cool the atoms and in the process see more pronounced effects in the Raman spectra.

Further extending the simulations will give us a deeper insight into the motional states. We have seen from the simulations that revival of Rabi oscillations happens on a timescale of a few ms. This is within the realm of testability and would also be an interesting measurement to carry out.

APPENDIX

A ELECTRIC FIELD OF A STANDING WAVE

A.1 Electric field of standing wave

Forming a standing wave with the quasi-linear nanofiber modes we can write the complex electric field as,

$$\begin{aligned}
\tilde{E}_r(t,r,\phi,z) &= E_r(t,r,\phi,z)\left(e^{-i\beta z}+e^{i\beta z}\right) \\
\tilde{E}_\phi(t,r,\phi,z) &= E_\phi(t,r,\phi,z)\left(e^{-i\beta z}+e^{i\beta z}\right) \\
\tilde{E}_z(t,r,\phi,z) &= E_z(t,r,\phi,z)\left(e^{-i\beta z}+e^{i(\beta z+\pi)}\right),
\end{aligned} \tag{A.1}$$

where β is the propagation constant. The electric field at different points in time is plotted in figure A.1. We see that the evolution of the electric field does not change the orientation of the field, leading to the cancellation of the longitudinal circular polarization of the running wave.

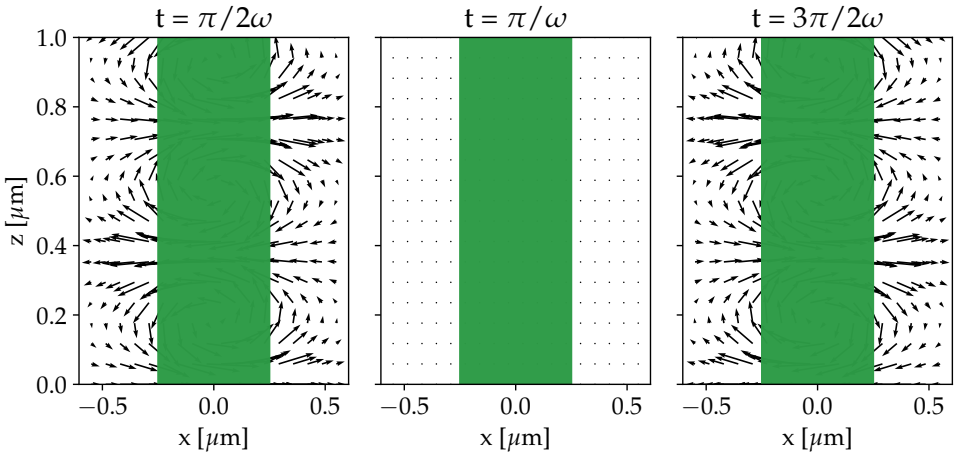

Figure A.1 — Electric field of the standing wave generated by counter propagating quasi-linear polarization modes. Arrows indicate the direction of the electric field. The green bar indicates the nanofiber. The orientation of the field stays the same over time, however the local polarization depends on the position.

APPENDIX

B STARK SHIFT CANCELLATION SUPPLEMENTARY

B.1 Cancellation on $(0 \rightarrow 0)$ vs $(-3 \rightarrow -4)$

The calculation of the differential Stark shift calculation follows the treatment given in [Østfeldt, 2017]. In the far detuned carrier case we can write the Stark shift of the level $|F, m_F\rangle$ as

$$\Delta E_{ls}^{(F,m_F)} = C \sum_{F',m_{F'},SB} \left(A^{(m_F - m_{F'})} \frac{I_{SB} |C_{FF'}^{m_F m_{F'}}|^2}{(\Delta_{\text{carr}} + \omega_{SB}) + \Delta_{FF'}^{m_F,m_{F'}}} \right) \tag{B.1}$$

where we sum over the sidebands SB with intensity I_{SB} and sideband frequency ω_{SB}, and the full excited state manifold F', $m_{F'}$. For each excited level we find the Clebsch-Gordan coefficient $C_{FF'}^{m_F m_{F'}}$ between the ground state and each excited level. The $A^{(m_F - m_{F'})}$ variable accounts for the amount of each polarization component of the light, with $m_F - m_{F'} = \pm 1$ being $\sigma^{\pm}$-polarization and $m_F - m_{F'} = 0$ being π polarization. C is simply a conversion factor to ensure proper units. The variable Δ_{carr} is the carrier detuning of the Raman light. The variable $\Delta_{FF'}^{m_F m_{F'}}$ is the shift of the excited state w.r.t. the center of the upper manifold, taking into account the shift of the ground state level. This will be a function of the applied magnetic field,

$$\Delta_{FF'}^{m_F m_{F'}} = \Delta_{F'} + m_F \mu_B g_F B + m_{F'} \mu_B g_{F'} B + \Delta_{hfs} \delta_{F,3} \tag{B.2}$$

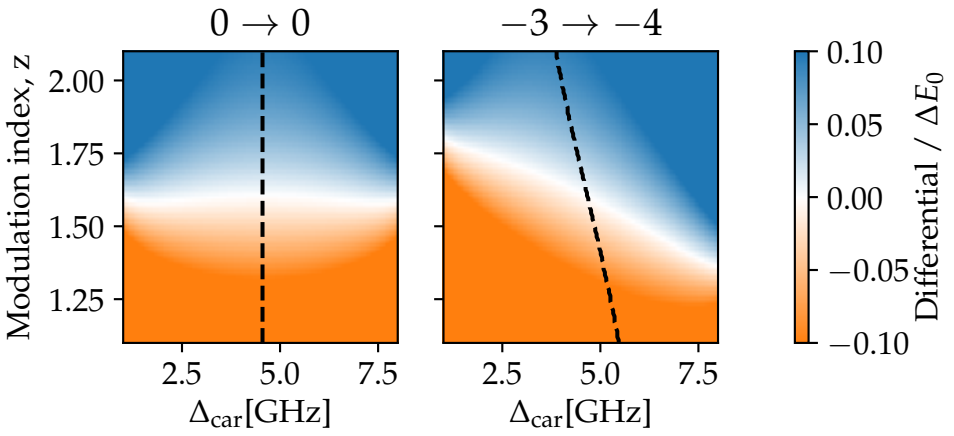

Figure B.1 — Differential Stark shifts on the $|F = 3, m_F = 0\rangle \rightarrow |F = 4, m_F = 0\rangle$ and $|F = 3, m_F = -4\rangle \rightarrow |F = 4, m_F = -4\rangle$ transitions. Dashed lines indicate parameters for balanced common-mode Stark shift.

where μ_B is the Bohr magneton, g_F is the Landé g-factor of the hyperfine level, B is the applied magnetic field and where we have introduced the last term to account for the difference between the $F = 4$ and $F = 3$ levels. The first term is the detuning of the level F' w.r.t. the center of the excited state manifold in the absence of a magnetic field.

The Raman sidebands used in the dipole force-free Raman scheme are generated using phase modulation. The phase modulation can be written as

$$E(t) = E_0 e^{i\omega t}\left[J_0(z) + \sum_{n=1}^{\infty} J_n(z)\left(e^{in\omega_{SB}t} + (-1)^n e^{-in\omega_{SB}t}\right)\right] \tag{B.3}$$

where J_n is the nth order Bessel function of the first kind and where z is the modulation index. Changing the modulation index affects the relative amplitudes of the generated sidebands and as such lead to different Stark shift contributions. By scanning the carrier detuning and the modulation index we can map out the parameter space to find the combination which leads to zero differential Stark shift, defined as

$$\Delta E_{\text{diff}} = \Delta E_{ls}^{(3,-3)} - \Delta E_{ls}^{(4,-4)} \tag{B.4}$$

for the $-3 \rightarrow -4$ transition.

Figure B.1 shows the differential Stark shifts between levels $(0 \rightarrow 0)$ and $(-3 \rightarrow -4)$ with an applied magnetic field of 3 Gauss using the first

five Raman sidebands. We see that for a carrier detuning of $\sim 4.7\,\mathrm{GHz}$ on the $(0 \rightarrow 0)$ transition we find an optimum modulation index of 1.6, however, on the $(-3 \rightarrow -4)$ transition this is no longer the optimum; the optimum modulation index is shifted upwards slightly. This is also consistent with our measurements.

APPENDIX

C RAMAN SPECTROSCOPY SUPPLEMENTARY

C.1 Error propagation for temperature estimation

To find the error of the temperature estimates we first have to error propagate the formula for calculating the temperature. The temperature is given by

$$T = -\frac{\hbar\omega_{SB}}{k_B}\frac{1}{\ln(r_{SB})} \tag{C.1}$$

where ω_{SB} is the mean sideband frequency and r_{SB} is the sideband ratio. Using the law of error propagation, [Barlow, 1991], the uncertainty of T is given by,

$$\delta_T = \frac{\hbar}{k_B}\sqrt{\left(\frac{1}{\ln(r_{SB})}\right)^2 \delta^2_{\omega_{SB}} + \left(\frac{\omega_{SB}}{r_{SB}}\right)^2 \delta^2_{r_{SB}}}. \tag{C.2}$$

The sidebands are fitted with the function

$$S_{SB}(\Delta) = A\frac{e^{-(\Delta-\mu)^2/2\sigma^2}}{1+e^{-\alpha(\Delta-\mu)}} \tag{C.3}$$

since this function has no simple expression for the integral and mean frequency we have to calculate these quantities numerically. The uncertainty in the frequency and area can be calculated from the standard deviation of the numerical results. To calculate the two quantities we take

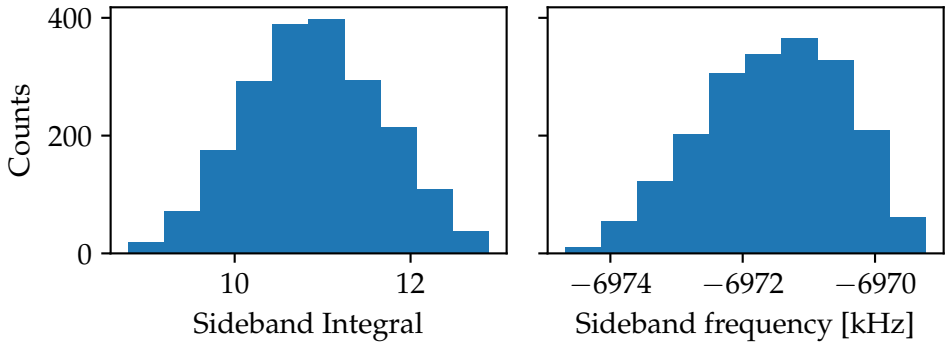

Figure C.1 — Monte Carlo simulations of the sideband area and sideband frequency for degenerate Raman cooled spectra. 2000 iterations used.

a random set of fit parameters, lying within the range of uncertainty from the fit, we then compute the quantities. Afterwards the means and standard deviations give us the necessary information to calculate the error in the temperature estimate. Figure C.1 shows histograms of the Monte Carlo simulation of the sidebands in section 9.2.1.

C.2 Bias magnetic field for cooling

The determination of the optimum bias magnetic field is carried out by varying the current sent to the MOT coils, generating the bias field. By stepping the magnetic field we can find the appropriate value, i.e. the magnetic field for which the largest fraction of the atoms are left in the trap after a certain amount of time. Measurements of the optimum bias field are shown in figure C.2.

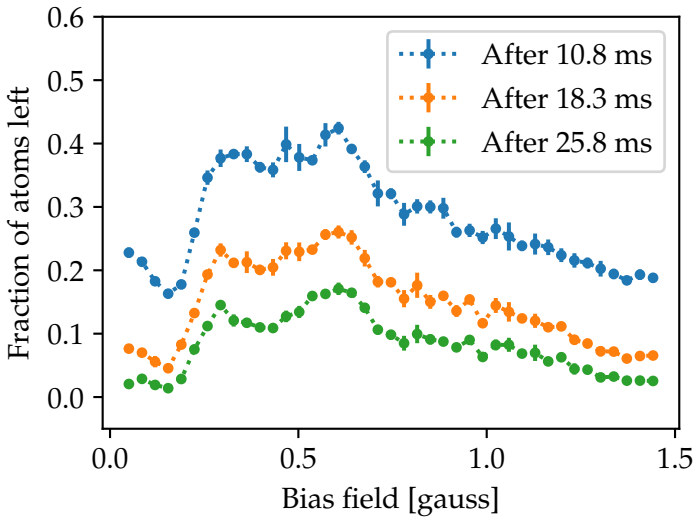

Figure C.2 — Fraction of atoms in the trap after different time intervals using different bias magnetic fields. Note the peaks at ~ 0.5 Gauss.

BIBLIOGRAPHY

H. J. Kimble. The quantum internet, 2008. ISSN 14764687.

John Preskill. Lecture Notes. chapter 1. California Institute of Technology, 1998. URL http://www.theory.caltech.edu/people/preskill/ph229/notes/chap1.pdf.

Limin Tong, Jingyi Lou, and Eric Mazur. Single-mode guiding properties of subwavelength-diameter silica and silicon wire waveguides. *Opt. Express*, 2004. ISSN 1094-4087. doi: 10.1364/opex.12.001025.

Fam Le Kien, V. I. Balykin, and K. Hakuta. Atom trap and waveguide using a two-color evanescent light field around a subwavelength-diameter optical fiber. Technical Report 6, 2004.

E Vetsch, D Reitz, G. Sagué, R Schmidt, S T Dawkins, and A Rauschenbeutel. Optical interface created by laser-cooled atoms trapped in the evanescent field surrounding an optical nanofiber. *Phys. Rev. Lett.*, 104(20), 2010. ISSN 00319007. doi: 10.1103/PhysRevLett.104.203603.

J. B. Béguin. *A one-dimensional Quantum Interface between a few atoms and weak light*. Ph.d, University of Copenhagen, 2015.

C.J. Foot. Atomic Physics (Oxford Master Series in Atomic, Optical and Laser Physics). *Citeulike.Org*, 2005.

Daniel Adam Steck. *Quantum and Atom Optics*. 2007. URL http://steck.us/teaching.

Daniel A Steck. Cesium D Line Data. *Theor. Div.*, 4710(7):1–31, 2008. ISSN 00036951. doi: 10.1063/1.2430906. URL papers2://publication/uuid/3652516F-351D-4309-AF4A-4EC5C8825574{%}5Cnhttp://steck.us/alkalidata/.

Peter W. Milonni and Joseph H. Eberly. *Laser Physics*. John Wiley & sons, 2010. ISBN 9780470387719.

J. Dalibard and C. Cohen-Tannoudji. Dressed-atom approach to atomic motion in laser light: the dipole force revisited. *J. Opt. Soc. Am. B*, 2 (11):1707, 1985. ISSN 0740-3224. doi: 10.1364/josab.2.001707.

Fam Le Kien, Philipp Schneeweiss, and Arno Rauschenbeutel. Dynamical polarizability of atoms in arbitrary light fields: General theory and application to cesium. *Eur. Phys. J. D*, 67(5):28–30, 2013. ISSN 14346060. doi: 10.1140/epjd/e2013-30729-x.

C. Lacrôute, K. S. Choi, A. Goban, D. J. Alton, D. Ding, N. P. Stern, and H. J. Kimble. A state-insensitive, compensated nanofiber trap. *New J. Phys.*, 14, 2012. ISSN 13672630. doi: 10.1088/1367-2630/14/2/023056.

E. Brion, L. H. Pedersen, and K. Mølmer. Adiabatic elimination in a lambda system. *J. Phys. A Math. Theor.*, 40(5):1033–1043, 2007. ISSN 17518113. doi: 10.1088/1751-8113/40/5/011.

Steven Chu. Laser Trapping of Neutral Particles. *Sci. Am.*, 1992. ISSN 0036-8733. doi: 10.1038/scientificamerican0292-70.

Claude N. Cohen-Tannoudji and William D. Phillips. New mechanisms for laser cooling. *Phys. Today*, 1990. ISSN 19450699. doi: 10.1063/1.881239.

D. Boiron, A. Michaud, P. Lemonde, Y. Castin, C. Salomon, S. Weyers, K. Szymaniec, L. Cognet, and A. Clairon. Laser cooling of cesium atoms in gray optical molasses down to 1.1 μK. *Phys. Rev. A - At. Mol. Opt. Phys.*, 1996. ISSN 10941622. doi: 10.1103/PhysRevA.53.R3734.

D. J. Wineland, C. Monroe, W. M. Itano, D. Leibfried, B. E. King, and D. M. Meekhof. Experimental Issues in Coherent Quantum-State Manipulation of Trapped Atomic Ions. *J. Res. Natl. Inst. Stand. Technol.*, 103(3):259–328, 1998. ISSN 1044677X. doi: 10.6028/jres.103.019.

Christoffer Østfeldt. *Coherent Optical Control and Cooling of Nanofiber-trapped Atoms*. Master thesis, University of Copenhagen, 2017.

B. Albrecht, Y. Meng, C. Clausen, A. Dareau, P. Schneeweiss, and A. Rauschenbeutel. Fictitious magnetic-field gradients in optical microtraps as an experimental tool for interrogating and manipulating cold atoms. *Phys. Rev. A*, 2016. ISSN 24699934. doi: 10.1103/PhysRevA.94.061401.

Y. Meng, A. Dareau, P. Schneeweiss, and A. Rauschenbeutel. Near-Ground-State Cooling of Atoms Optically Trapped 300 nm Away from a Hot Surface. *Phys. Rev. X*, 2018. ISSN 21603308. doi: 10.1103/PhysRevX.8.031054.

Signe Brynold Markussen. *Trapping and Cooling of Cesium Atoms in an Optical Nanofiber Trap*. Master thesis, University of Copenhagen, 2020.

Eugen Vetsch. *Optical Interface Based on a Nanofiber*. Ph.d, Johannes Gutenberg University, 2010.

M. Boustimi, J. Baudon, P. Candori, and J. Robert. Van der Waals interaction between an atom and a metallic nanowire. *Phys. Rev. B - Condens. Matter Mater. Phys.*, 2002. ISSN 01631829. doi: 10.1103/PhysRevB.65.155402.

N Schlosser, G Reymond, and P Grangier. Collisional Blockade in Microscopic Optical Dipole Traps. *Phys. Rev. Lett.*, 89(2), 2002. ISSN 10797114. doi: 10.1103/PhysRevLett.89.023005.

Freja Thilde Pedersen. *High Transmission Optical Nanofibers - Fabrication and Characterization*. Master thesis, University of Copenhagen, 2017.

J. D. Love, W. M. Henry, W. J. Stewart, R. J. Black, S. Lacroix, and F. Gonthier. Tapered single-mode fibres and devices Part 1. Adiabaticity criteria. *IEE proceedings. Part J, Optoelectron.*, 1991. ISSN 02673932. doi: 10.1049/ip-j.1991.0060.

Fredrik K. Fatemi, Jonathan E. Hoffman, Pablo Solano, Eliot F. Fenton, Guy Beadie, Steven L. Rolston, and Luis A. Orozco. Modal interference in optical nanofibers for sub-Angstrom radius sensitivity. *Optica*, 2017. ISSN 2334-2536. doi: 10.1364/optica.4.000157.

D. Gabor. Theory of communication. *J. Inst. Electr. Eng. - Part I Gen.*, pages 429–457, 1947. doi: 10.1049/ji-1.1947.0015.

Eric R.I. Abraham and Eric A. Cornell. Teflon feedthrough for coupling optical fibers into ultrahigh vacuum systems. *Appl. Opt.*, 1998. ISSN 15394522. doi: 10.1364/AO.37.001762.

V. I. Balykin, K. Hakuta, Fam Le Kien, J. Q. Liang, and M. Morinaga. Atom trapping and guiding with a subwavelength-diameter optical fiber. *Phys. Rev. A - At. Mol. Opt. Phys.*, 70(1):1–5, 2004. ISSN 10502947. doi: 10.1103/PhysRevA.70.011401.

F. Warken, E. Vetsch, D. Meschede, M. Sokolowski, and A. Rauschenbeutel. Ultra-sensitive surface absorption spectroscopy using sub-wavelength diameter optical fibers. *Opt. Express*, 15(19):11952, 2007. ISSN 1094-4087. doi: 10.1364/oe.15.011952.

Pablo Solano, Jeffrey A. Grover, Jonathan E. Hoffman, Sylvain Ravets, Fredrik K. Fatemi, Luis A. Orozco, and Steven L. Rolston. Optical Nanofibers: A New Platform for Quantum Optics. *Adv. At. Mol. Opt. Phys.*, 66:439–505, 2017. ISSN 1049250X. doi: 10.1016/bs.aamop.2017.02.003.

J. B. Béguin, E. M. Bookjans, S. L. Christensen, H. L. Sørensen, J. H. Müller, E. S. Polzik, and J. Appel. Generation and detection of a sub-poissonian atom number distribution in a one-dimensional optical lattice. *Phys. Rev. Lett.*, 113(26), 2014. ISSN 10797114. doi: 10.1103/PhysRevLett.113.263603.

Christoffer Østfeldt, Jean-Baptiste S. Béguin, Freja T. Pedersen, Eugene S. Polzik, Jörg H. Müller, and Jürgen Appel. Dipole force free optical control and cooling of nanofiber trapped atoms. *Opt. Lett.*, 42 (21):4315, 2017. ISSN 0146-9592. doi: 10.1364/ol.42.004315.

Jürgen Appel, Andrew Macrae, and A I Lvovsky. Versatile Digital GHz Phase Lock for External Cavity Diode Lasers. 2010.

Jacob Thornfeldt Hansen. *Raman Spectroscopy of nanofiber trapped cesium atoms*. Bachelor thesis, University of Copenhagen, 2018.

Signe Brynold Markussen. *Motion of Atoms in a Nanofiber Trap*. Bachelor thesis, University of Copenhagen, 2017.

Sara Elisabeth Dahl Andersen. *Characterization of motional frequencies in a nanofiber atom trap*. Bachelor thesis, University of Copenhagen, 2018.

Daniel Hümmer, Philipp Schneeweiss, Arno Rauschenbeutel, and Oriol Romero-Isart. Heating in Nanophotonic Traps for Cold Atoms. *Phys. Rev. X*, 2019. ISSN 21603308. doi: 10.1103/PhysRevX.9.041034.

D. Leibfried, R. Blatt, C. Monroe, and D. Wineland. Quantum dynamics of single trapped ions. *Rev. Mod. Phys.*, 75(1):281–324, 2003. ISSN 00346861. doi: 10.1103/RevModPhys.75.281.

Christopher C. Gerry and Peter L. Knight. *Introductory Quantum Optics*. 2005. ISBN 9780521820356.

J. R. Dormand and P. J. Prince. A family of embedded Runge-Kutta formulae. *J. Comput. Appl. Math.*, 1980. ISSN 0771050X. doi: 10.1016/0771-050X(80)90013-3.

Pauli Virtanen, Ralf Gommers, Travis E. Oliphant, Matt Haberland, Tyler Reddy, David Cournapeau, Evgeni Burovski, Pearu Peterson, Warren Weckesser, Jonathan Bright, Stéfan J. van der Walt, Matthew Brett, Joshua Wilson, K. Jarrod Millman, Nikolay Mayorov, Andrew R.J. Nelson, Eric Jones, Robert Kern, Eric Larson, C. J. Carey, İlhan Polat, Yu Feng, Eric W. Moore, Jake VanderPlas, Denis Laxalde, Josef Perktold, Robert Cimrman, Ian Henriksen, E. A. Quintero, Charles R. Harris, Anne M. Archibald, Antônio H. Ribeiro, Fabian Pedregosa, Paul van Mulbregt, Aditya Vijaykumar, Alessandro Pietro Bardelli, Alex Rothberg, Andreas Hilboll, Andreas Kloeckner, Anthony Scopatz, Antony Lee, Ariel Rokem, C. Nathan Woods, Chad Fulton, Charles Masson, Christian Häggström, Clark Fitzgerald, David A. Nicholson, David R. Hagen, Dmitrii V. Pasechnik, Emanuele Olivetti, Eric Martin, Eric Wieser, Fabrice Silva, Felix Lenders, Florian Wilhelm, G. Young, Gavin A. Price, Gert Ludwig Ingold, Gregory E. Allen, Gregory R. Lee, Hervé Audren, Irvin Probst, Jörg P. Dietrich, Jacob Silterra, James T. Webber, Janko Slavič, Joel Nothman, Johannes Buchner, Johannes Kulick, Johannes L. Schönberger, José Vinícius de Miranda Cardoso, Joscha Reimer, Joseph Harrington, Juan Luis Cano Rodríguez, Juan Nunez-Iglesias, Justin Kuczynski, Kevin Tritz, Martin Thoma, Matthew Newville, Matthias Kümmerer, Maximilian Bolingbroke, Michael Tartre, Mikhail Pak, Nathaniel J. Smith, Nikolai Nowaczyk, Nikolay Shebanov, Oleksandr Pavlyk, Per A. Brodtkorb, Perry Lee, Robert T. McGibbon, Roman Feldbauer, Sam Lewis, Sam Tygier, Scott Sievert, Sebastiano Vigna, Stefan Peterson, Surhud More, Tadeusz Pudlik, Takuya Oshima, Thomas J. Pingel, Thomas P. Robitaille, Thomas Spura, Thouis R. Jones, Tim Cera, Tim Leslie, Tiziano Zito, Tom Krauss, Utkarsh Upadhyay, Yaroslav O. Halchenko, and Yoshiki Vázquez-Baeza. SciPy 1.0: fundamental algorithms for scientific computing in Python. *Nat. Methods*, 2020. ISSN 15487105. doi: 10.1038/s41592-019-0686-2.

L. F. Shampine and C. W. Gear. A User's View of Solving Stiff Ordinary Differential Equations. *SIAM Rev.*, 1979. ISSN 0036-1445. doi: 10.1137/1021001.

Signe B. Markussen, Jürgen Appel, Christoffer Østfeldt, Jean Baptiste S. Béguin, Eugene S. Polzik, and Jörg H. Müller. Measure-

ment and simulation of atomic motion in nanoscale optical trapping potentials. *Appl. Phys. B Lasers Opt.*, 2020. ISSN 09462171. doi: 10.1007/s00340-020-07424-5.

R. J. Barlow. Statistics: A Guide to the Use of Statistical Methods in the Physical Sciences. *Technometrics*, 1991. ISSN 00401706. doi: 10.2307/1269014.